Optimal Design of Soft Responsive Actuators and Impact Resistant Structures

Thesis by

Andrew Akerson

In Partial Fulfillment of the Requirements for the
Degree of
Doctor of Philosophy

CALIFORNIA INSTITUTE OF TECHNOLOGY
Pasadena, California

2023
Defended May 23, 2023

Andrew Akerson
ORCID: 0000-0002-4382-1226

ACKNOWLEDGEMENTS

There are a number of people that had an enormous hand in my graduate studies through their guidance, motivation, and support. Here, I would like to mention these people and their contributions. This includes advisors, thesis committee members, past and present group members, collaborators, friends, and most importantly family.

Firstly, I am enormously grateful to my advisor Kaushik Bhattacharya. His wisdom and intuition, coupled with his ability to communicate his thoughts, allowed the projects I worked on under him to move (mostly) smoothly. The wealth of knowledge he has on all things mechanics related allowed me to ask him any questions, regardless of their connection to my research, where he always managed to provide insights. Throughout my PhD he was extraordinarily patient, allowing me to learn and develop on my own. More importantly, he was stern when I was stubborn, pushing me in the necessary directions. It is a great privilege to work under him and with the incredible group he somehow finds time to manage.

I would also like to give a special thanks to my committee members Michael Ortiz, Chiara Daraio, Ruby Fu, and Ryan Watkins. Much of my mechanics philosophy is directly and indirectly attributed to that of Michael Ortiz. Since he began attending our joint group meetings, I have thoroughly enjoyed our conversations, where I always seem to come away from them having learned something. Chiara has also been instrumental in my education. Her nonlinear wave propagation course was enormously helpful in developing dynamics intuition. More importantly, she was always very supportive of me and provided career advice throughout my time at Caltech. While Ruby arrived towards the end of my studies, in the time she has been here we have had wonderful conversations. The often lively discussions ranged from her career experiences as a young faculty to progress in our concurrently sprained ankles. Finally, Ryan Watkins has provided a rich amount of practical knowledge. In his short stint as visiting researcher from JPL, he has been a welcome addition to the weekly group meetings.

Next, I would like to thank the past and current group members. I have learned quite a lot from our discussions and working through problems to-

gether. In particular, it has been a pleasure working with and beside Roubing Bai, Buregede Liu, Sharan Injeti, Kevin Korner, Eric Ocegueda, Aakila Rajan, Sathvik Sanagala, Adeline Wihardja, Carter Cocke, and Maximo Cravero Baraja. Additionally, members of the Ravi group have grown to be great friends while also provided insights into experimental methods. These include Suraj Ravidran, Vatsa Ghandi, Jack Weeks, and Barry Lawlor.

I have also had the opportunity to work with incredible collaborators. I have learned mathematics and mathematical thinking working with Blaise Bourdin on optimal design of responsive structures. I have also had the pleasure of working with Taylor Ware and his student, Seelay Tasmin, and his postdoc, Asaf Dana. Their knowledge of polymer chemistry and the ability to make designs I generate in the computer into a functional object is simply incredible. Finally, Connor McMahan's thoughtfulness, drive, and efficiency while working on his project doing continuum models for architected structures was invaluable to my development as a researcher. It was also the most fun I have ever had while doing mechanics.

I would also like to acknowledge the brilliant people at the University of Minnesota. Through my time as an undergraduate and masters student, the faculty in the department of Aerospace Engineering and Mechanics provided me with a great foundational education and mechanics perspective. In particular, Richard James, Perry Leo, and Ryan Elliott's teaching was extremely formative. Ryan taught me many of the tools I use today through the research he guided me through. I am grateful for his patience and support, where he is always available, even now, to provide thoughtful advice. I should also thank Paul Plucinsky, as I would not be where I am today without him. At the time, he was a Postdoc at Minnesota where he insisted I apply to Caltech. I would also like to acknowledge the great friends I made at Minnesota. I always look forward to catching up and regaling our times in Akerman Hall with Alex Pratt, Devon Veldhouse, Matt Skelton, and Bryce Doerr to name a few.

The friends I have made at Caltech have made my time here truly special. For the sake of brevity, I will only name a few. Jack Weeks, Prithvi Akella, Connor McMahan, Ethan Pickering, Maximo Cravero Baraja, Vatsa Ghandi, Aakila Rajan, Sathvik Sanagala, Shengduo Liu, Carter Cocke, and Ethan Eichberger have been nothing but superb company, fueling both interesting discussions and degenerate antics. In particular, Jack, Prithvi, Connor, and Vatsa have

been with me my entire time at Caltech. There is no one else I would have rather have gone through the experience with.

Lastly, I would like to thank my family for their love and support through the years. My parents Mike and Betsy Akerson, and my brother Joey Akerson, have continued to support me from across the country. While I have missed them greatly being so far away, they always manage to make the trek from the midwest to visit periodically. Also, Jessica Wettstein has also been enormously supportive through my time as a student. Also I would like to thank my pets Dino and the late BunBun. Dino is a good cat and BunBun was a good bunny. They have been a welcome, time consuming distractions from my studies.

ABSTRACT

The rapid pace of development of new responsive and structural materials along with significant advances in synthesis techniques, which may incorporate multiple materials in complex architectures, provides an opportunity to design functional devices and structures of unprecedented performance. These include implantable medical devices, soft-robotic actuators, wearable haptic devices, mechanical protection, and energy storage or conversion devices. However, the full realization of the potential of these emerging techniques requires a robust, reliable, and systematic design approach. This thesis explores this through optimal design methods. By investigating pressing engineering problems which exploit these advances in materials and manufacturing, we develop optimal design methods to realize next-generation structures.

We begin by reviewing classical optimal design methods, the mathematical difficulties they raise, and the practical approaches of overcoming these difficulties. We introduce the canonical problem of compliance minimization of a linear elastic structure. After illustrating the intricacies of this seemingly simple problem, we detail contemporary methods used to address the underlying mathematical issues.

We then turn to extending these classical methods for emerging materials and technologies. We must incorporate optimal design with rich physical models, develop computational approaches for efficient numerics, and study mathematical regularization to obtain well-posed optimization problems. Additionally, care must be taken when selecting an application-tailored objective function which captures the desired behavior. Finally, we must also take into account manufacturing constraints in scenarios where the fabrication pathway affects the structural layout. We address these issues by exploring model optimal design problems. While these serve to ground the fundamental study, they are also relevant, pressing engineering problems.

The first application we consider is the design of responsive structures. Recent developments in material synthesis and 3D printing of anisotropic materials, such as liquid crystal elastomers (LCE), have facilitated the realization of structures with arbitrary morphology and tailored material orientation. These methods may also produce integrated structures of passive and active material.

This creates a trade-off between stiffness and actuation flexibility when designing such structures. Thus, we turn to optimal design. This is complicated by anisotropic behavior and finite deformations, manufacturing constraints, and choice of objective function. Like many optimal design problems, the naive formulations are ill-posed giving rise to mesh dependence, lack of convergence, and other numerical deficiencies. So, starting with a simple setting using linear kinematics and working all the way to finite deformation, we develop a systematic mathematical theory that motivates, and then rigorously proves, an alternate well-posed formulation. We examine suitable objective functions, before studying a series of examples in both small and finite deformation. However, the manufacturing process constrains the design as extrusion-based 3D printing aligns nematic directors along the print path. We extended the formulation with these considerations to produce print-aware designs while also recovering the fabrication pathway. We demonstrate the formulation by designing and producing physical realizations of these actuators.

Next, we explore optimal design of impact resistant structures. The complex physics and numerous failure modes of structural impact creates challenges when designing for impact resistance. Here, we apply gradient-based topology optimization to the design of such structures. We start by constructing a variational model of an elastic-plastic material enriched with gradient phase-field damage, and present a novel method to accurately and efficiently compute its transient dynamic time evolution. Sensitivities over this trajectory are computed through the adjoint method, and we develop a numerical method to solve the resulting adjoint dynamical system. We demonstrate this formulation by studying the optimal design of 2D solid-void structures undergoing blast loading. Then, we explore the trade-offs between strength and toughness in the design of a spall-resistant structure composed of two materials of differing properties undergoing dynamic impact.

We conclude by summarizing the presented work and discuss the contribution towards the overarching goal of optimal design for emerging materials technologies. From our study, key issues have arose which must be addressed to further progress the field. We examine these and lay a pathway for future studies which will allow optimal design to tackle complicated, pressing engineering problems.

PUBLISHED CONTENT AND CONTRIBUTIONS

Akerson, A., Optimal Structures for Failure Resistance Under Impact, *Journal of Mechanics and Physics of Solids* 172 105172, 2023.
doi.org/10.1016/j.jmps.2022.105172

Akerson, A., Bourdin, B., and Bhattacharya, K., "Optimal Design of Responsive Structures", *Structural and Multidisciplinary Optimization* 65:4, 2022.
doi.org/10.1007/s00158-022-03200-5
Contributions: A.A. worked on the development of the mathematical framework based on suggestions of B.B. and K.B., took the lead in the mathematical proofs and numerical simulations, and wrote the manuscript.

McMahan, C., Akerson, A., Celli, P., Audoly, B., and Daraio, C., "Effective Continuum Models for the Buckling of Non-periodic Architected Sheets that Display Quasi-mechanism Behaviors", *Journal of Mechanics and Physics of Solids* 166 104934, 2022.
doi.org/10.1016/j.jmps.2022.104934
Contributions: A.A. developed the numerical method, wrote the computational code, performed simulations, and wrote the numerical method section of the manuscript. M.C. developed the model, assisted with the computations, performed experiments, wrote the rest of the manuscript. C.P., A.B., and D.C. provided technical guidance and introduced the research direction.

TABLE OF CONTENTS

LIST OF ILLUSTRATIONS

LIST OF TABLES

Chapter 1

INTRODUCTION

The rapid pace of development of new responsive and structural materials along with significant advances of synthesis techniques, which may incorporate multiple materials in complex architectures, provide an opportunity to design functional devices and structures of unprecedented performance. These include implantable medical devices, soft-robotic actuators, wearable haptic devices, and mechanical protection. However, the full realization of the potential of these emerging techniques requires a robust, reliable, and systematic design approach. This is especially true when complex materials, dynamic loading, multi-physics coupling, or manufacturing constraints become involved. Additionally, with advances in computational capabilities, numerical methods to iteratively design these complex structures are now feasible. This thesis focuses on developing rigorous optimal design methods to translate these advances in materials and synthesis towards practical applications.

In practice, engineers typically design structures by starting with industry standards and intuition, followed by sophisticated dynamical simulations to iterate on a design before it undergoes physical testing. While this allows engineers to design adequate structures for simple scenarios, it may fall short in situations which are governed by richer physics, complex material behavior, or include manufacturing constraints. Optimal design methods replace the empirical and incremental approach in favor of a systematic computational procedure which eliminates the guesswork and human factor in structural design. Rather than manually designing a structure, optimal design looks to solve the inverse problem of finding the layout of material that optimizes a performance metric. This is typically solved using well-developed, contemporary optimization techniques. While these methods were once prohibitively computationally expensive, the ever-increasing amount of available computing power may allow us to employ these methods to solve complicated problems producing application tailored structures.

The ideas of optimal design date back to over a century ago, however much of the development has occurred in the past few decades [16]. The subject

was originally contemplated in the late 1800s by James Clark Maxwell and Anthony Michell [17, 18]. These works went largely unnoticed by the community until the mid 20th century, when researchers began optimizing thicknesses of truss members [24, 9, 34]. This grew over the decades to considering material distributions in continuous solids [26, 6, 27]. However, these early methods often relied on ad-hoc methods to regularize the formulation to achieve a computationally tractable problem [28, 22]. While these methods have been shown to have physical significance [30], there has been work to mathematically formalize these techniques to rigorously prove well-posedness of the design problem [12, 13, 14, 7]. The general ideas of optimal design have since been extended to a wide array of applications including acoustic band-gaps [29], piezoelectric transducers [31], micro-electro-mechanical systems [20], magneto-responsive structures [40], energy conversion devices [8], and fluid structure interaction [39]. However, these are mainly linear or steady-state problems.

The field of optimal design as been extensively formulated for optimizing simple objective functions using basic mechanics models. While somewhat academic in nature, this has yielded a rich literature which we may base this work on [5, 7, 1]. Before we consider optimal design for complex problems, we first discuss these previously developed methods. However, even for simple problems, care must be taken in the formulation to achieve a tractable optimization problem. We review these difficulties, discuss the new challenges which arise from more complex problems, and discuss how we plan to address them. Finally, we give a brief outline of the thesis and how each of the projects discussed fit into the larger framework of optimal design for emerging technologies.

1.1 Optimal Design Methods

We detail the three main approaches to optimal design. These are sizing, shape, and topology optimization. We discuss the details of these methods, explore each of their strengths and limitations, and provide relevant applications.

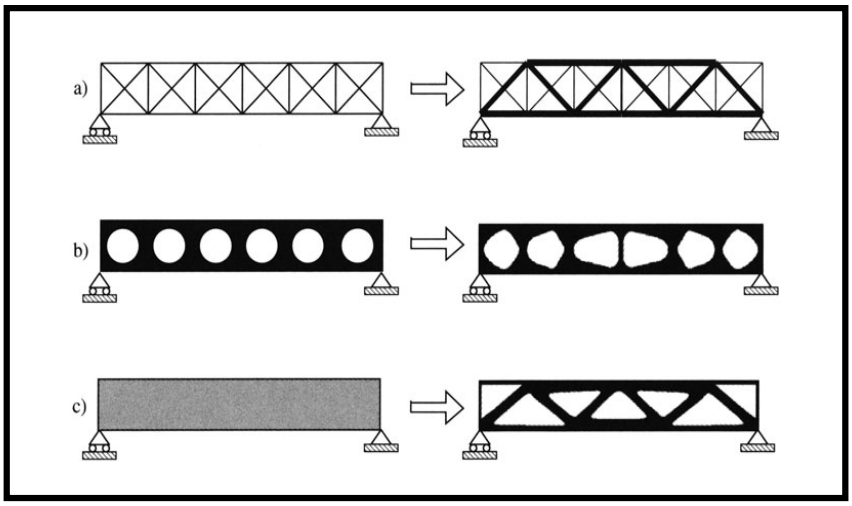

Figure 1.1: The original (left) and converged (right) geometries for sizing optimization (a), shape optimization (b), and topology optimization (c). Taken from *Topology Optimization: Theory, Methods and Applications, 2nd edition*, Springer by Bendsøe and Sigmund, 2003.

1.1.1 Sizing Optimization

The earliest and least computationally intensive method is sizing optimization. Here, the optimization problem is posed as finding the dimensions of known structural elements. This is commonly used to determine the optimal thickness distribution of truss members [34]. While this simple method is restrictive by assuming the placement of these elements, it has been applied to complex problems such as tuning acoustic band gaps of lattice structures [11], and designing crash-resistant truss structures undergoing plasticity [19].

1.1.2 Shape Optimization

Shape optimization looks to find the optimal design of a structure through controlling the shape of voids or sub-regions of the domain. Here, the structure is assumed to have a set number of voids or sub-regions, with the shape of them considered as the optimized quantity. This is commonly formulated with sharp-interface methods, where the interface of the sub-regions are considered as level-sets of a scalar design function. Then, optimizing over this function evolves the shape to achieve the desired performance [2, 1, 4]. Another method of shape optimization is the method of mappings [35]. Here, the initial design with pre-placed holes or sub-regions is considered as the reference configura-

tion, where a smooth mapping deforms the structure to the design. Then, optimizing over this mapping function optimizes the structure. This requires careful consideration of the mapping, often being the solution to an auxiliary, elliptic PDE to ensure regularity [10].

The main benefit of shape optimization is that the sharp interface between material species is preserved. Additionally, perturbing the shape of these regions often results in optimization algorithms converging quicker than topology optimization methods. However, restricting the design to a known number of sub-regions is quite prohibitive. Nonetheless, researchers have applied these to study problems ranging from multi-material structural optimization [38] to multi-physics problems [25].

1.1.3 Topology Optimization

Topology optimization looks to find the optimal placement of material in a given domain. At the cost of computational expense, topology optimization is the most powerful of the three methods as it does not involve any predefined configurations [5]. Typical density-based methods consider the density of material at each point in the domain as the unknown before the design is posed as an optimization problem over these densities. Then, gradient-based optimization methods are used to iteratively update the design, where sensitivities are usually computed through the adjoint method [23]. However, the basic formulation often results in an ill-posed optimization problem [12]. Therefore, researchers use a variety of techniques to recover a well-posed optimization problem. Ad-hoc methods such as sensitivity filtering, where gradients are locally averaged prior to design updates, produce viable structures [5]. However, more systematic approaches such as density filtering [7], phase-field methods [33, 21], slope penalization [22], and PDE filtering techniques [15, 37] regularize the underlying mathematical problem. This also serves practical purposes by introducing a minimum length scale of features through the filter radii and transition lengths. For all these methods, care must be taken in determining the behavior of intermediate densities between material species, while ensuring the final design is composed mostly of either species. This is usually achieved by implicitly penalizing intermediate densities [5], and we discuss these ideas further in the proceeding chapter.

While the filtering and phase-field methods incur an additional computational

expense, topology optimization remains the most general optimal design formulation. By not assuming the number or placement of structural members, topology optimization is the most expressive, being able to search a wider range of the design space. However, this is at the cost of introducing a large optimization problem, with the number of design variables usually well into the thousands. This is not seen as a major issue, as modern gradient-based update schemes are able to handle these problems [32], with the majority of the computational time spent on repeatedly solving the governing PDEs.

Gradient-based optimization methods are the most conventionally used techniques for structural optimization. Whether for sizing, shape, or topology optimization, gradient-based methods outclass Bayesian or genetic algorithm approaches due to the high cost of evaluation. A solution to the governing PDE is required to obtain the objective value for a given design. Thus, Bayesian methods, where the number of required evaluations scale exponentially with the parameter space of the design, are computationally infeasible. This is especially true for topology optimization, where the number of design variables may exceed several thousand. Conversely, gradient-based optimization schemes tend to scale only with the complexity of the underlying problem, rather than the dimension of the parameterization. Furthermore, the adjoint method allows one to obtain these gradients at a cost on the same order as the evaluation. It is typical for gradient-based optimal design schemes to converge on the order of a hundred evaluations. Thus, gradient-based optimization remains the most popular choice in these settings.

As the focus of the presented work will be restricted to topology optimization methods, in Chapter 2 we review the canonical problem of minimum compliance optimization of a linear elastic structure. We start by discussing a classical formulation for topology optimization. As the naiive construction often results in an ill-posed optimization problem, we detail the density filtering method to regularize and recover well-posedness. Then, we discuss the adjoint method for obtaining the sensitivities used for gradient-based optimization. Finally, we touch on the computational details and how this method is implemented in practice.

1.2 Optimal Design for More Complex Problems

While the minimum compliance example detailed in Chapter 2 introduces the topology optimization formulation, regularization techniques, and standard computational procedures for optimal design, there are a number of difficulties that must be addressed when tackling design problems related to the emerging materials and manufacturing technologies. These include modeling richer physics, computational approaches for efficient numerics, and regularization to obtain well-posed optimization problems. Additionally, care must be taken when selecting an application-tailored objective function which captures the desired behavior. Finally, we must also take into account manufacturing constraints in scenarios where the fabrication pathway affects the structural layout.

Applications which are of interest to engineers are often governed by complex physical interactions. Materials for soft robotics and actuation can involve large deformation of stimuli responsive materials and microstructural evolution. While there has been some work exploring optimal design with finite deformation theory [21], formulating this for a responsive structure remains a challenge. Another application area is 3D printed metals for mechanical protection. Here, transient dynamics, plasticity, and material failure become relevant. Thus, optimal design formulations must account for this through the modeling and design methodology.

As optimal design is an iterative process, requiring repeated mechanics simulations, computational efficiency is of great importance. However, modeling complex physical interactions incurs increased computational cost. Thus, developing numerical schemes which may efficiently perform the required computations is a key challenge. In the compliance minimization example, the forward and adjoint problems are both simple linear problems. However, this is not true in general, especially when nonlinear mechanics, dynamics, and material failure are involved. As such, we must address computational accuracy, efficiency, and scalability for both the forward and associated adjoint problems.

Once the complex mechanics and its computational algorithms are addressed, we must direct our focus towards optimization. Here, we should give careful consideration for proper objective functions which correlate to desired performance. This is a non-trivial endeavor. Complex models introduce new field

variables through dynamic trajectories which need to be used to quantify a performance metric. Furthermore, we must ensure the resulting optimization problem is well-posed. As we will discuss in the minimum compliance example, naiive approaches can result in mesh dependency and fine structure formation in the optimal solutions. For density-based topology optimization, filtering schemes work well. However, with additional design variables such as material orientation, we must develop suitable regularization methods.

As we intend to develop methods which may translate to applications, we must consider manufacturability. Filtering techniques introduce a minimum length scale for features, which can often be set to that of the manufacturing resolution. This is appropriate for isotropic materials, as conventional methods of translating the design to a fabrication pathway will yield the desired structure. However, this is not the case for certain classes of anisotropic materials. Here, the 3D print path may determine the material orientation [3, 36]. Additionally, ensuring the structure may be printing in a time-efficient manner is desired. We must account for these aspects in the design formulation to achieve manufacturable designs.

1.3 Outline of Thesis

We address these issues of modeling, computation, optimization, and manufacturability by exploring model optimal design problems. While these serve to ground the fundamental study, they are also relevant, pressing engineering problems. By examining the optimal designs, we may gain mechanics insight into the physical interactions that give rise to improved performance. Thus, our exploration is aimed at developing foundational methods while demonstrating them for relevant applications.

We start in Chapter 2 by introducing the example of minimum compliance for an isotropic linear elastic structure. As the naiive formulation results in an ill-posed optimization problem, we discuss regularization through density filtering. Then, we introduce the adjoint method for obtaining sensitivities for design updates. Finally, we detail the general computational procedure and finite element discretizations used to solve the problem in practice. This provides a foundation which we may extend to emerging materials and manufacturing technologies.

We move on to Chapter 3 by investigating optimal design of responsive struc-

tures. Here, we explore integrated structures composed of passive and active materials for use in actuation. We consider linear kinematics, and explore different objective functions for this problem. We adopt the filtering and penalization methods we detailed for the minimum compliance problem, and rigorously prove regularization in this setting. We study examples in 2D and 3D by designing lifting and torsional actuators. While this work considering small deformation theory and fixed actuation strains, it develops key insights related to objective functions and mathematical regularization for responsive materials.

In Chapter 4 we extend these ideas to consider large deformations, anisotropic responsive materials with spatially varying orientations, and manufacturing constraints. We consider the model problem of designing responsive actuators made of liquid crystal elastomers. These materials are composed of rod-like nematic molecules embedded in an elastomer matrix. Upon heating, these materials undergo a solid-to-solid phase transformation where the nematic molecules transition from an aligned to disordered state. This pulls the elastomer matrix, resulting large deformation. We develop optimal design methods which account for this large deformation and the microstructural evolution. As the orientation of the nematic molecules, or director field, can be tailored through manufacturing processes, we optimize the material orientation. However, 3D printing methods for these materials aligns the directors along the print path. This introduces an additional constraint, which extend the formulation to account for. Through this, we develop mathematically rigorous theory to ensure regularization of the optimization problem. Additional, we present physical realization of these designs which are produced by a collaborating research lab.

The last example we consider in Chapter 5 is that of impact resistant structures for mechanical protection. Here, the complex physics of transient dynamics, plasticity, and material failure must be accounted for. We formulated a variational model with such considerations and develop a novel computational approach for simulating the forward and adjoint problem. We accomplish this through an operator-splitting method to decouple the non-linearity and non-locality for the damage updates. This results in an accurate and efficient computational procedure for the required simulations. We formulate optimal design through density-based topology optimization, and construct interpo-

lation function to both penalize intermediate densities and preserve natural boundary conditions. We apply these methods to investigate the design of solid-void structures for blast loading. Then, we explore the trade-offs between strength and toughness to design spall-resistant impact resistant structures.

Through these examples, we address the challenges posed in Section 1.2. We develop general optimal design methods, backed by rigorous mathematical theory, to tackle complex design problems related to actuation and mechanical protection. This is detailed in Chapter 6. Additionally, we discuss the difficulties that have arose through our investigations. We conclude by laying the groundwork for future investigations that may allow optimal design methods to exploit emerging materials and manufacturing technologies while solving pressing engineering problems.

BIBLIOGRAPHY

[1] G. Allaire, F. De Gournay, F. Jouve, and A. M. Toader. Structural optimization using topological and shape sensitivity via a level set method. *Control and Cybernetics*, 34(1):59–81, 2005.

[2] G. Allaire, F. Jouve, and A.-M. Toader. A level-set method for shape optimization. *Comptes Rendus Mathematique*, 334(12):1125–1130, 2002.

[3] C. P. Ambulo, M. J. Ford, K. Searles, C. Majidi, and T. H. Ware. 4d-printable liquid metal–liquid crystal elastomer composites. *ACS Applied Materials & Interfaces*, 13(11):12805–12813, 2021.

[4] S. Amstutz and H. Andrä. A new algorithm for topology optimization using a level-set method. Technical Report 78, Fraunhofer (ITWM), 2005.

[5] M. Bendsøe and O. Sigmund. *Topology Optimization: Theory, Methods and Applications*. Springer, 2nd edition, 2003.

[6] M. P. Bendsøe. Optimal shape design as a material distribution problem. *Structural Optimization*, 1(4):193–202, 1989.

[7] B. Bourdin. Filters in topology optimization. *International Journal for Numerical Methods in Engineering*, 50(9):2143–2158, 2001.

[8] L. N. Collins and K. Bhattacharya. Optimal design of a model energy conversion device. *Structural and Multidisciplinary Optimization*, 59:389–401, 2017.

[9] J. Foulkes. The minimum-weight design of structural frames. *Proceedings of the Royal Society of London. Series A, Mathematical and Physical Sciences*, 223(1155):482–494, 1954.

[10] J. Haubner, M. Siebenborn, and M. Ulbrich. A continuous perspective on shape optimization via domain transformations. *SIAM Journal on Scientific Computing*, 43(3):A1997–A2018, 2021.

[11] S. Injeti. *Multi-Functional Metamaterials*. PhD thesis, California Institute of Technology, 2021.

[12] R. V. Kohn and G. Strang. Optimal design and relaxation of variational problems, i. *Communications on Pure and Applied Mathematics*, 39(1):113–137, 1986.

[13] R. V. Kohn and G. Strang. Optimal design and relaxation of variational problems. ii. Technical report, Massachusetts Inst of Tech Cambridge, 1986.

[14] R. V. Kohn and G. Strang. Optimal design and relaxation of variational problems. iii. Technical report, Massachusetts Inst of Tech Cambridge, 1986.

[15] B. S. Lazarov and O. Sigmund. Filters in topology optimization based on helmholtz-type differential equations. *International Journal for Numerical Methods in Engineering*, 86(6):765–781, 2011.

[16] J. Lógó and H. Ismail. Milestones in the 150-year history of topology optimization: A review. *Computer Assisted Methods in Engineering and Science*, 27(2–3), 2020.

[17] J. C. Maxwell. I.—on reciprocal figures, frames, and diagrams of forces. *Earth and Environmental Science Transactions of The Royal Society of Edinburgh*, 26(1):1–40, 1870.

[18] A. Michell. Lviii. the limits of economy of material in frame-structures. *The London, Edinburgh, and Dublin Philosophical Magazine and Journal of Science*, 8(47):589–597, 1904.

[19] C. B. Pedersen. Topology optimization for crashworthiness of frame structures. *International Journal of Crashworthiness*, 8(1):29–39, 2003.

[20] N. L. Pedersen. Topology optimization of laminated plates with prestress. *Computers and Structures*, 80(7-8):559–570, 2002.

[21] P. Penzler, M. Rumpf, and B. Wirth. A phase-field model for compliance shape optimization in nonlinear elasticity. *ESAIM: Control, Optimisation and Calculus of Variations*, 18(1):229–258, 2012.

[22] J. Petersson and O. Sigmund. Slope constrained topology optimization. *International Journal for Numerical Methods in Engineering*, 41(8):1417–1434, 1998.

[23] R. E. Plessix. A review of the adjoint-state method for computing the gradient of a functional with geophysical applications. *Geophysical Journal International*, 167(2):495–503, 2006.

[24] W. Prager. Optimization of structural design. *Journal of Optimization Theory and Applications*, 6:1–21, 1970.

[25] X. Ren, A. Thabuis, A. Hannukainen, and Y. Perriard. Shape optimization of soft magnetic composites using level-set method. *IEEE Transactions on Magnetics*, 57(5):1–8, 2021.

[26] M. P. Rossow and J. E. Taylor. A finite element method for the optimal design of variable thickness sheets. *AIAA Journal*, 11(11):1566–1569, 1973.

[27] G. Rozvany and W. Prager. *Structural Design Via Optimality Criteria: The Prager Approach to Structural Optimization*. Mechanics of Elastic and Inela. Springer Netherlands, 1989.

[28] O. Sigmund. On the design of compliant mechanisms using topology optimization. *Mechanics of Structures and Machines*, 25(4):493–524, 1997.

[29] O. Sigmund and J. S. Jensen. Systematic design of phononic band-gap materials and structures by topology optimization. *Philosophical Transactions of the Royal Society A: Mathematical, Physical and Engineering Sciences*, 361(1806):1001–1019, 2003.

[30] O. Sigmund and K. Maute. Sensitivity filtering from a continuum mechanics perspective. *Structural and Multidisciplinary Optimization*, 46, 10 2012.

[31] E. C. N. Silva and N. Kikuchi. Design of piezoelectric transducers using topology optimization. *Smart Materials and Structures*, 8(3):350–364, 1999.

[32] K. Svanberg. The method of moving asymptotes - a new method for structural optimization. *International Journal for Numerical Methods in Engineering.*, 24(October 1985):359–373, 1987.

[33] A. Takezawa, S. Nishiwaki, and M. Kitamura. Shape and topology optimization based on the phase field method and sensitivity analysis. *Journal of Computational Physics*, 229(7):2697–2718, 2010.

[34] J. E. Taylor and M. P. Rossow. Optimal truss design based on an algorithm using optimality criteria. *International Journal of Solids and Structures*, 13(10):913–923, 1977.

[35] S. Thomas. Shape optimization for semi-linear elliptic equations based on an embedding domain method. *Applied Mathematics and Optimization*, 49, 03 2004.

[36] S. W. Ula, N. A. Traugutt, R. H. Volpe, R. R. Patel, K. Yu, and C. M. Yakacki. Liquid crystal elastomers: an introduction and review of emerging technologies. *Liquid Crystals Reviews*, 6(1):78–107, 2018.

[37] M. Wallin, N. Ivarsson, O. Amir, and D. Tortorelli. Consistent boundary conditions for pde filter regularization in topology optimization. *Structural and Multidisciplinary Optimization*, 62(3), 4 2020.

[38] Y. Wang, Z. Luo, Z. Kang, and N. Zhang. A multi-material level set-based topology and shape optimization method. *Computer Methods in Applied Mechanics and Engineering*, 283:1570–1586, 2015.

[39] G. H. Yoon. Topology optimization for stationary fluid–structure interaction problems using a new monolithic formulation. *International Journal for Numerical Methods in Engineering*, 82(5):591–616, 2010.

[40] Z. Zhao and X. S. Zhang. Topology optimization of hard-magnetic soft materials. *Journal of the Mechanics and Physics of Solids*, 158:104628, 2022.

Chapter 2

BACKGROUND: MINIMUM COMPLIANCE

As the focus of the work presented in the proceeding chapters is on topology optimization, we start by reviewing the canonical problem of minimum compliance optimization of a linear elastic structure. We introduce a naive formulation for the topology optimization problem, and quickly realize the mathematical issues with this approach. We discuss the different methods used to relax and regularize this ill-posed optimization problem. In particular, we detail the density filtering method to recover well-posedness. Then, we discuss the adjoint method for obtaining the design sensitivities used for gradient-based optimization. Finally, we provide computational details through a finite element discretization, and how the method is implemented in practice.

2.0.1 Formulation

We consider a bounded region $\Omega \subset \mathbb{R}^n$, $n = 2, 3$, occupied by two isotropic linear elastic materials with elastic moduli $\mathbb{C}_1$ and $\mathbb{C}_2$, occupying regions $D_1 \subset \Omega$, $D_2 \subset \Omega$, $D_1 \cup D_2 = \Omega$, respectively. Here, we assume a large stiffness contrast $\|\mathbb{C}_2\| >> \|\mathbb{C}_1\|$. We consider fixed displacements $u = u_0$ on some region of the boundary $\partial_u\Omega \subset \partial\Omega$, with boundary tractions f applied to $\partial_f\Omega \subset \Omega$. Thus, with $u : \Omega \mapsto \mathbb{R}^n$ as a displacement field, we assume an energy function for the structure as

$$\begin{aligned}\mathcal{E}(u,\chi) := \int_\Omega \left[(1-\chi)\frac{1}{2}\mathbb{C}_1\varepsilon(u)\cdot\varepsilon(u) + (\chi)\frac{1}{2}\mathbb{C}_2\varepsilon(u)\cdot\varepsilon(u)\right]\, d\Omega \\ - \int_{\partial_f\Omega} f\cdot u\; dS,\end{aligned} \tag{2.1}$$

where $\varepsilon(u) := 1/2(\nabla u + \nabla u^T)$ is the symmetric gradient and χ is the characteristic function of the region D_2,

$$\chi(x) := \begin{cases} 0 & \text{if } x \in D_1 \\ 1 & \text{if } x \in D_2 \end{cases}. \tag{2.2}$$

Then, the equilibrium displacement field is determined through energy minimization

$$u^{eq} = \arg\min_{u\in\mathcal{U}} \mathcal{E}(u,\chi), \tag{2.3}$$

where

$$\mathcal{U} := \{u \in H^1(\Omega),\ u = u_0 \text{ on } \partial_u\Omega\} \tag{2.4}$$

is the space of admissible displacements. The compliance is defined as

$$\mathcal{C}(\chi) := \int_{\partial_f\Omega} f \cdot u^{eq}\ dS. \tag{2.5}$$

Then, the optimization problem is to minimize the compliance subject to a volume constraint on the stiffer material,

$$\begin{gathered}\inf_{\chi\in\mathcal{D}} \mathcal{C}(\chi) = \int_{\partial_f\Omega} f \cdot u^{eq}\ dS \\ \text{Subject to : } u^{eq} \text{ satisfying (2.3)},\end{gathered} \tag{2.6}$$

where

$$\mathcal{D} := \left\{\chi : \Omega \mapsto \{0,1\},\ \frac{1}{|\Omega|}\int_\Omega \chi\ d\Omega \le \alpha\right\} \tag{2.7}$$

is the space of admissible designs, with α being the restricted volume fraction.

2.0.2 Relaxation and Regularization

The optimization problem (2.7) is ill-posed. As fine mixtures of material species has enhanced stiffness, infinitely fine structure may emerge in the optimization [7]. Mathematically, this design problem is not *lower semi-continuous*, that is a minimizing sequence may not converge on the minimimzer. This issue manifests in computation deficiencies such as mesh dependencies and checkerboard structures [3]. To proceed, there are a few options. The mathematically rigorous approach to solving (2.7) is to relax the problem by instead considering the *G-closure*, that being the space of all effective elastic moduli tensors achievable through fine mixtures of $\mathbb{C}_1$ and $\mathbb{C}_2$. Then, by optimizing point-wise over these effective moduli, we recover a well-posed optimization problem [1, 4]. This is referred to as homogenization methods, and while effective in simple 2D cases where the G-closure is determined, such as electrical conductor design [2], it does not translate well to 3D or nonlinear problems. Additionally, even if we can find micro-structures associated with each effective moduli, this poses manufacturing issues when producing this fine-scale structure.

Instead, we take the approach of density relaxation combined with a convolution filter and penalization [5]. We relax the problem to consider a continuous,

scalar density variable $\rho : \Omega \mapsto [0,1]$, where regions of $\rho = 0$ and $\rho = 1$ correspond to regions of material with moduli $\mathbb{C}_1$ and $\mathbb{C}_2$. Then, intermediate densities $\rho \in (0,1)$ represent mixtures of the two materials. Finally, we filter the density variable through a convolution filter with filter function F of characteristic length R_f,

$$\begin{aligned} &F \in W^{1,2}(\mathbb{R}^n), \\ &\text{Supp}(F) \subset B_{R_f}, \\ &F \geq 0 \ \text{ a.e. in } \ B_{R_f}, \\ &\int_{B_{R_f}} F \ dx = 1, \end{aligned} \tag{2.8}$$

where B_{R_f} denotes the open ball of radius R_f of $\mathbb{R}^n$, and we define the convolution over the bounded region Ω as

$$(F * \rho)(x) := \int_\Omega F(x-y)\rho(y) \ dy. \tag{2.9}$$

Then, the energy function depends on the filtered density as

$$\begin{aligned} \mathcal{E}(u,\rho) := \int_\Omega \Big[&(1-(F*\rho)^p)\,\frac{1}{2}\mathbb{C}_1\varepsilon(u)\cdot\varepsilon(u) \\ &+ (F*\rho)^p \frac{1}{2}\mathbb{C}_2\varepsilon(u)\cdot\varepsilon(u)\Big] \ d\Omega - \int_{\partial_f\Omega} f\cdot u \ dS, \end{aligned} \tag{2.10}$$

where $p \in \mathbb{R}$, $p > 1$ is the penalization power. This implicitly penalizes regions of intermediate densities, as there is little stiffness gain in the intermediate regions compared to the fully stiff regions. Under the constraint that the total volume of stiffer material is constrained, this results in unfavorable intermediate densities. This technique is known classically as the solid isotropic material with penalization (SIMP) method. Then, the minimum compliance problem becomes

$$\begin{aligned} \inf_{\rho\in\mathcal{D}_\rho} \ \mathcal{C}(\rho) &= \int_{\partial_f\Omega} f\cdot u^{eq} \ dS \\ \text{Subject to : } u^{eq} &= \arg\min_{u\in\mathcal{U}} \ \mathcal{E}(u,\rho), \end{aligned} \tag{2.11}$$

where

$$\mathcal{D}_\rho := \left\{ \rho : \Omega \mapsto [0,1], \ \frac{1}{|\Omega|}\int_\Omega \rho \ d\Omega \leq \alpha \right\} \tag{2.12}$$

is the space of admissible designs. With this relaxation and regulation through the filter, the optimization problem 2.11 is proven to be well posed [5]. That is, there exists a design $\bar{\rho} \in \mathcal{D}_\rho$ which attains the minimum to the optimization problem. Thus, the previously mentioned issue of fine structure formation is

alleviated, with the filter length R_f prescribing the length scale of features. Intuitively, the filter smooths out the design and eliminates the effect of fine structure on the energy functional. Thus, the minimizing design will not have this infinitely fine structure. Mathematically, the filter allows weakly converging designs to result in a strongly converging operator in the governing PDE, resulting in lower semi-continuity of the objective function.

2.0.3 Adjoint Method for Sensitivities

To solve (2.11), gradient based optimization is typically employed. Starting with an initial design, the elasticity PDE is solved, followed by the adjoint method to obtain the *sensitivities*, that is, the derivative of the objective function with respect to the design variables. These sensitivities are used to update the design with a gradient based optimization method, and the process is iterated until convergence. However, the design affects equilibrium displacement fields which are used to compute the objective. This variation of the equilibrium displacement with the design variable is difficult to obtain through standard means. Thus, we introduce the adjoint method to circumvent this calculation [8]. This results in an adjoint problem whose solution is used to recover the sensitivities. We detail this procedure for the minimum compliance example.

The minimization criteria for the equilibrium displacement u^{eq} in (2.11) can be equivalently written in weak form,

$$\begin{aligned} 0 = \int_\Omega \Big[&\left(1 - (F * \rho)^p\right) \mathbb{C}_1 \varepsilon(u) \cdot \varepsilon(\delta u) \\ &+ (F * \rho)^p \mathbb{C}_2 \varepsilon(u) \cdot \varepsilon(\delta u) \Big] \, d\Omega - \int_{\partial_f \Omega} f \cdot \delta u \, dS \qquad \forall \delta u \in \mathcal{U}_0, \end{aligned} \tag{2.13}$$

where

$$\mathcal{U}_0 := \{u \in H^1(\Omega), \ u = 0 \text{ on } \partial_u \Omega\} \tag{2.14}$$

is the space of admissible displacement variations. Then, assuming u^{eq} satisfies equilibrium, the compliance is equivalent to the Lagrangian

$$\begin{aligned} \mathcal{L}(\rho) := \int_{\partial_f \Omega} f \cdot u^{eq} \, dS + \int_\Omega \Big[&\left(1 - (F * \rho)^p\right) \mathbb{C}_1 \varepsilon(u^{eq}) \cdot \varepsilon(\lambda) \\ &+ (F * \rho)^p \mathbb{C}_2 \varepsilon(u^{eq}) \cdot \varepsilon(\lambda) \Big] \, d\Omega \\ - \int_{\partial_f \Omega} f \cdot \lambda \, dS, \end{aligned} \tag{2.15}$$

for any adjoint field $\lambda \in \mathcal{U}_0$. Here, it is clear that $\mathcal{L}$ is equivalent to $\mathcal{C}$ as we have only added zero through the satisfied weak form of equilibrium. We denote the variation of functional $\mathcal{L}(\rho)$ in the direction of $\delta\rho$ as

$$\mathcal{L}_{,\rho}\delta\rho := \frac{\mathrm{d}}{\mathrm{d}v}\left[\mathcal{L}(\rho + v\delta\rho)\right]\Big|_{v=0}, \tag{2.16}$$

and the variations of the function u^{eq} with ρ as

$$\delta_\rho u^{eq} := \frac{\mathrm{d}}{\mathrm{d}v}\left[u^{eq}|_{\rho+v\delta\rho}\right]\Big|_{v=0}. \tag{2.17}$$

Then, taking variations of (2.15) gives

$$\begin{aligned}\mathcal{L}_{,\rho}\delta\rho := &\int_{\partial_f\Omega} f\cdot\delta_\rho u^{eq}\, dS \\ &+\int_\Omega \Big[\left(1-(F*\delta\rho)^p\right)\mathbb{C}_1\varepsilon(u^{eq})\cdot\varepsilon(\lambda) \\ &\qquad + (F*\delta\rho)^p\mathbb{C}_2\varepsilon(u^{eq})\cdot\varepsilon(\lambda) \\ &\qquad + \left(1-(F*\rho)^p\right)\mathbb{C}_1\varepsilon(\delta_\rho u^{eq})\cdot\varepsilon(\lambda) \\ &\qquad + (F*\rho)^p\mathbb{C}_2\varepsilon(\delta_\rho u^{eq})\cdot\varepsilon(\lambda)\Big]\, d\Omega.\end{aligned} \tag{2.18}$$

The term $\delta_\rho u^{eq}$ is the most difficult to compute. We circumvent this by instead choosing a particular λ to eliminate terms which contain variations of the equilibrium displacement. Then, the sensitivity reduces to

$$\begin{aligned}\mathcal{L}_{,\rho}\delta\rho = \mathcal{C}_{,\rho}\delta\rho = \int_\Omega \Big[&\left(1-(F*\delta\rho)^p\right)\mathbb{C}_1\varepsilon(u^{eq})\cdot\varepsilon(\lambda) \\ &+ (F*\delta\rho)^p\mathbb{C}_2\varepsilon(u^{eq})\cdot\varepsilon(\lambda)\Big]\, d\Omega\end{aligned} \tag{2.19}$$

if the adjoint field $\lambda \in \mathcal{U}_0$ satisfies

$$\begin{aligned}0 = &\int_\Omega \Big[\left(1-(F*\rho)^p\right)\mathbb{C}_1\varepsilon(\delta_\rho u)\cdot\varepsilon(\lambda) \\ &\qquad + (F*\rho)^p\mathbb{C}_2\varepsilon(\delta_\rho u^{eq})\cdot\varepsilon(\lambda)\Big]\, d\Omega \\ &+\int_{\partial_f\Omega} f\cdot\delta_\rho u^{eq}\, dS \qquad\qquad \forall\delta_\rho u^{eq}\in\mathcal{U}_0.\end{aligned} \tag{2.20}$$

It should be noted that for this particular objective function and linear elastic model, in the case of homogeneous boundary conditions it can be easily shown that $\lambda = -u^{eq}$. However, in general this is not the case, requiring one to solve the adjoint problem. The standard procedure is to first compute the solution to the elasticity problem (2.13), then solve the adjoint problem (2.20), before computing the sensitivities (2.19).

2.0.4 Computational Implementation

To solve the optimization problem (2.11) using the adjoint method detailed above, we turn to computation. As linear elasticity lends itself well to a standard Galerkin finite element formulation, this is the approach we take. However, it should be noted that the choice to discretization is quite arbitrary, and the presented discussion mainly serves to illustrate the computational procedure.

We consider a standard Galerkin finite element formulation with Lagrange polynomial shape functions [6]. We consider the displacement field discretized as

$$u^h(x) = \sum_{i=1}^{N} u_i N^i(x), \tag{2.21}$$

where $\{N^i\} \subset H^1(\Omega)$ are the vector valued shape functions and $\{u_i\}$ are their scalar amplitudes. We consider the associated approximation space

$$\mathcal{U}^h := \Big\{ u \in H^1(\Omega),\ u^h = \sum_{i=1}^{N} u_i N^i,\ u^h = u_0 \text{ on } \partial_u \Omega^h \Big\}, \tag{2.22}$$

where Ω^h is the tessellated domain. As is standard, we choose a discontinous Galerkin discretization for the density field [3],

$$\rho^h = \sum_{\beta=1}^{N_e} \rho_\beta \Phi^\beta, \tag{2.23}$$

where $\{\Phi^\beta\} \subset L^2(\Omega)$ are the non conforming shape functions for the density, and $\{\rho_\beta\}$ is the amplitude. Usually, it is assumed that the shape functions take a value of identity on regions of compact support for each of the N_e elements of the finite element mesh. Then, the design space is reduced to

$$\mathcal{D}_\rho^h := \Big\{ \rho^h : \Omega \mapsto [0,1],\ \rho^h = \sum_{\beta=1}^{N_e} \rho_\beta \Phi^\beta,\ \frac{1}{|\Omega^h|} \int_{\Omega^h} \rho^h \, d\Omega \leq \alpha \Big\}. \tag{2.24}$$

Minimizing the elastic energy with respect to displacement fields in the approximation space results in the equilibrium relation

$$\begin{aligned} 0 = \int_{\Omega^h} \Big[& \Big(1 - (F * \rho^h)^p\Big) \mathbb{C}_1 \varepsilon(u^h) \cdot \varepsilon(\nabla N^i) \\ & + (F * \rho^h)^p \mathbb{C}_2 \varepsilon(u^h) \cdot \varepsilon(\nabla N^i) \Big] \, d\Omega \\ & - \int_{\partial_f \Omega^h} f \cdot N^i \, dS \qquad\qquad i = 1, \ldots, N, \end{aligned} \tag{2.25}$$

along with the associated Dirichlet boundary conditions. This is a set of N linear equations with N unknowns being the amplitudes of the unknown displacement field. The adjoint variable is discretized in the same finite element space as the displacements,

$$\lambda^h(x) = \sum_{i=1}^{N} \lambda_i N^i(x). \tag{2.26}$$

Then, the discrete counterpart to the adjoint problem in (2.20) is

$$\begin{aligned} 0 = \int_{\Omega^h} \Big[\Big(1 - (F * \rho^h)^p\Big) \mathbb{C}_1 \varepsilon(\nabla N^i) \cdot \varepsilon(\lambda^h) \\ + (F * \rho^h)^p \mathbb{C}_2 \varepsilon(\nabla N^i) \cdot \varepsilon(\lambda^h) \Big] \, d\Omega \\ - \int_{\partial_f \Omega^h} f \cdot N^i \, dS \qquad\qquad i = 1, \ldots, N, \end{aligned} \tag{2.27}$$

with the associated boundary conditions. Again, this is a set of equations for the N adjoint amplitudes. In all of the above, these integrals are conventionally approximated with Gaussian quadrature, with the compact support of the shape functions providing efficient computation.

Then, the sensitivities may be computed as

$$\begin{aligned} \frac{\mathrm{d}\mathcal{C}}{\mathrm{d}\rho_\beta} = \mathcal{C}_{,\rho} \Phi^\beta = \int_{\Omega^h} \Big[\Big(1 - (F * \Phi^\beta)^p\Big) \mathbb{C}_1 \varepsilon(u^h) \cdot \varepsilon(\lambda^h) \\ + (F * \Phi^\beta)^p \mathbb{C}_2 \varepsilon(u^h) \cdot \varepsilon(\lambda^h) \Big] \, d\Omega, \end{aligned} \tag{2.28}$$

where u is the equilibrium displacement field computed from (2.25). In practice, the continuous form of the filter is usually replaced with a discrete analogue [5]. Here, the filtered density is taken constant on each element β as

$$(F * \rho^h)_\beta = \frac{\displaystyle\sum_{i \in V(\beta)} \rho_i \int_{\Omega_i^h} F(x - c_\beta) \, dx}{\displaystyle\sum_{i \in V(\beta)} \int_{\Omega_i^h} F(x - c_\beta) \, dx}, \tag{2.29}$$

where Ω_i^h is element i, c_β is the center of element β, and $V(\beta)$ is the set of elements whose centers are within the filter radius R_f to element β. The denominator in (2.29) normalizes the filter density, allowing the filtered density to attain values of unity near the boundary.

With the sensitivity calculated, the density values are then updated using a gradient based optimization scheme. For simple problems, such as linear

elastic compliance minimization, optimality criteria methods may be used [10]. However, for more complicated problems, stochastic gradient descent or more sophisticated algorithms such as method of moving asymptotes [9] is usually employed. The designs are continuously updated until convergence, usually requiring $\mathcal{O}(100)$ iterations [3].

2.1 Conclusion

Through the minimum compliance example, we introduced the underlying mathematical issues that arise in optimal design. The lack of lower-semicontinuity of the optimization problem allows the formation of infinitely fine structure along minimizing sequences. We discussed the methods to regularize the design problem to recover well-posedness. In particular, we detailed the density filtering method, where the effect of fine oscillations in microstructure is averaged through a convolution filter. We introduced the adjoint method to obtain design sensitivities, allowing us to apply well-developed gradient-based optimization methods. Finally, we discussed how this method is implemented in practice, providing a standard finite element discretization.

This seemingly simple example illustrated the key fundamental aspects of optimal design related to mathematical regularizing and sensitivity calculation. Additionally, it introduced methods which we will invoke when moving towards more complex problems. Density filtering and the SIMP interpolation scheme provide a foundation which we will extend to responsive actuators and impact-resistant structures. The ideas of mathematical regularization will become crucial when understanding the proper formulation when optimizing over both structure and material orientation.

BIBLIOGRAPHY

[1] G. Allaire, E. Bonnetier, G. Francfort, and F. Jouve. Shape optimization by the homogenization method. *Numerische Mathematik*, 76:27–68, 03 1997.

[2] G. Allaire and M. Briane. Multiscale convergence and reiterated homogenisation. *Proceedings of the Royal Society of Edinburgh Section A: Mathematics*, 126(2):297–342, 1996.

[3] M. Bendsøe and O. Sigmund. *Topology Optimization: Theory, Methods and Applications*. Springer, 2nd edition, 2003.

[4] M. P. Bendsøe and N. Kikuchi. Generating optimal topologies in structural design using a homogenization method. *Computer Methods in Applied Mechanics and Engineering*, 71(2):197–224, 1988.

[5] B. Bourdin. Filters in topology optimization. *International Journal for Numerical Methods in Engineering*, 50(9):2143–2158, 2001.

[6] P. G. Ciarlet. *The Finite Element Method for Elliptic Problems*. Society for Industrial and Applied Mathematics, 2002.

[7] R. V. Kohn and G. Strang. Optimal design and relaxation of variational problems, i. *Communications on Pure and Applied Mathematics*, 39(1):113–137, 1986.

[8] R. E. Plessix. A review of the adjoint-state method for computing the gradient of a functional with geophysical applications. *Geophysical Journal International*, 167(2):495–503, 2006.

[9] K. Svanberg. The method of moving asymptotes - a new method for structural optimization. *International Journal for Numerical Methods in Engineering.*, 24(October 1985):359–373, 1987.

[10] J. E. Taylor and M. P. Rossow. Optimal truss design based on an algorithm using optimality criteria. *International Journal of Solids and Structures*, 13(10):913–923, 1977.

Chapter 3

OPTIMAL DESIGN OF RESPONSIVE STRUCTURES

Akerson, A., Bourdin, B., and Bhattacharya, K. Optimal Design of Responsive Structures. *Structural and Multidisciplinary Optimization*, 65:4, 2022.

Contributions: A.A. worked on the development of the mathematical framework based on suggestions of B.B. and K.B., took the lead in the mathematical proofs and numerical simulations, and wrote the manuscript.

Abstract

With recent advances in both responsive materials and fabrication techniques it is now possible to construct integrated functional structures, composed of both structural and active materials. We investigate the robust design of such structures through topology optimization. By applying a typical interpolation scheme and filtering technique, we prove existence of an optimal design to a class of objective functions which depend on the compliances of the stimulated and unstimulated states. In particular, we consider the actuation work and the blocking load as objectives, both of which may be written in terms of compliances. We study numerical results for the design of a 2D rectangular lifting actuator for both of these objectives, and discuss some intuition behind the features of the converged designs. We formulate the optimal design of these integrated responsive structures with the introduction of voids or holes in the domain, and show that our existence result holds in this setting. We again consider the design of the 2D lifting actuator now with voids. Finally, we investigate the optimal design of an integrated 3D torsional actuator for maximum blocking torque.

3.1 Introduction

Recent advances in active or responsive materials, approaches to synthesis and fabrication, and significant applications ranging from soft robotics, wear-

able and prosthetic devices, microfluidics, etc. have led to the development of various integrated functional materials and devices (E.g. [32, 30, 45]). These devices integrate responsive or active materials such as shape-memory alloys, piezoelectrics, dielectric elastomers and liquid crystal elastomers with structural polymers and metals. Further, there have been rapid strides in advancing 3D printing and other synthesis technologies for responsive or active materials [9, 23, 42, 27, 19], and in combining them with structural components to build integrated functional materials and structures [34]. As the complexity and fidelity of the function, and consequently the complexity of the devices increase, it is important to develop a systematic design methodology.

Topology optimization has proven to be an extremely powerful tool in structural applications [12]. The naive formulation of the classical minimum compliance problem is ill-posed (e.g. [18, 1]). However, it can be relaxed for example using the homogenization method [4, 1] or regularized using perimeter penalization [8] or phase-field approach [15]. In particular, the "simple isotropic material with penalization (SIMP)" interpolation in conjunction with a filter is known to be well-posed and has proven to be extremely effective in practice [12]. While topology optimization led to many real-life applications, the designs were typically complex, and manufacturing optimal designs remained a challenge. The advent of 3D printing and similar net-shape fabrication techniques have greatly addressed these challenges and given new impetus to optimal design. In particular, conceptual links have been established between the multi-scale nature of topology optimization and the idea of tiling, and regularization to a method of incorporating manufacturing constraints. These have established a pathway to 3D print (almost) optimal structures (e.g., [28, 36, 21]).

The optimal design of structural actuators has been studied in a number of works. The design of thermomechanical actuators was originally considered by Rodrigues and Fernandes [33] for 2D linear elastic solids undergoing thermal expansion. These ideas were later extended to the design of multiphysics actuators using topology optimization methods by Sigmund [39, 40] for the application of micro-electrical mechanical systems (MEMS).

Since then, various researchers have considered optimal design of diverse structural actuators including soft piezoelectric microgrippers [35], magnetic actuators [29], and electro-fluid-thermal compliant actuators [44]. In these studies,

the actuator is characterized by three primary objectives. The first is the actuation work which is equivalent to the flexibility or displacement on actuation. The second is the blocking load, or the applied load that can nullify the actuation. The third is the "workpiece" objective, which balances flexibility and stiffness of the structure using a spring attached to a point of interest.

In this work, we provide a mathematical framework to explore the use of topology optimization for the design of integrated responsive structures. Specifically, we consider an actuating structure composed of both an active material which can deform or change modulus in response to a stimulus, and a passive material. We formulate the design of these structures as an optimization problem for a general class of objective functions which are dependent on the compliances in the passive (unstimulated) and active (stimulated) states. Modified with a generalized SIMP interpolation and density filter, we prove existence of an optimal design. It can be shown that all three of the objectives described in the previous discussion can be written as functions of compliance, and thus satisfy the requirements for existence. In particular, we study the actuation work and blocking load objectives. The first is the difference in compliances while we show that the second is equivalent to the ratio of compliances. We provide numerical examples for both of these objectives, and discuss intuition behind the converged designs.

We begin in Section 3.2 by reviewing the ill-posed minimum compliance problem, and recall how a SIMP interpolation and filtering technique may lead to a well-posed problem. In Section 3.3 we introduce the energy functional for the responsive structure, and formulate an optimal design problem in which the objective is dependent on the compliances of both the stimulated and unstimulated structure. By regularizing with a SIMP interpolation and density filter, we then prove existence of solutions to this optimal design problem. We continue in Section 3.4 where we discuss objective functions used to characterize actuating systems, namely a generalized "workpiece" objective, the actuation work, and the blocking load. We show that all of these can be written in terms of compliances and thus satisfy the requirements for our existence result. Additionally, we show that the latter two appear as limiting cases of the generalized "workpiece" objective. In Section 3.5 we consider numerical examples of actuating structures. We begin in Section 3.5.1 with the actuation work objective and consider the 2D design of bimorph lifting actuators for

varying elastic moduli ratios of passive and responsive material, volume fractions of active material, and domain aspect ratios. Next, in Section 3.5.2, we consider the design of identical actuator setups now optimized for the blocking load. In Section 3.6 we consider the introduction of holes or voids in the domain, and show that the existence result continues to hold for the blocking load objective. We consider the 2D design of a lifting actuator with voids in Section 3.6.1. Then, in Section 3.6.2, we demonstrate the formulation in a 3D setting by considering the optimal design of a torsional actuator. Finally, in Section 3.7, we discuss challenges and directions for further studies.

3.2 Background: Compliance Optimization

We briefly recall the classical minimum compliance problem [12]. Consider a bounded domain $\Omega \subset \mathbb{R}^n$, $n = 2, 3$, subject to a known traction f on a part $\partial_f\Omega \subset \partial\Omega$ of its boundary, and prescribed displacement u_0 on $\partial_u\Omega \subset \partial\Omega$. The domain is partitioned into two regions, D_1 and D_2, occupied respectively by two known linear elastic materials of moduli $\mathbb{C}_1$ and $\mathbb{C}_2$. We seek the arrangement of the regions D_1 and D_2 that minimize the compliance,

$$\inf_{(D_1,D_2)\in\mathcal{C}_A} \mathcal{C}(D_1, D_2) := \int_{\partial_f\Omega} f \cdot u \, dS, \tag{3.1}$$

where $\mathcal{C}_A$ is a set of admissible designs subject to inclusions and volume fraction constraints, and u the equilibrium displacement solution of a linearized elasticity problem. It is well known that problem (3.1) is ill-posed: its solution consists of fine mixtures of regions D_1 and D_2 instead of a "conventional" design. In the homogenization approach [4, 1], the design variables and the state equation are reformulated in terms of the so-called G-closure or the set of all Hooke's laws achievable by mixtures of materials D_1 and D_2. In this sense, the design of optimal structures reduces to that of optimal metamaterials. Metamaterials with optimal properties have been constructed explicitly [20, 25, 18, 26, 1] for well-ordered non-degenerate materials. However, optimal metamaterials are not known explicitly in general. Further, homogenization-based approaches do not always lead to manufacturable designs even with additive manufacturing, since optimality generally *r*equires multiple length-scales [20, 25, 2, 16], which can make manufacturing optimal structures challenging.

The issue of manufacturability can be tackled by enforcing geometric con-

straints [3, 31, 43, 5, 6, 7], or by seeking near-optimal designs with reduced complexity. The SIMP approach [11] relaxes the problem to "grey-scale" designs through a material density ϕ taking values in $[0, 1]$. The effective Hooke's law is then interpolated to $\mathbb{C} = \phi^p \mathbb{C}_1 + (1 - \phi^p)\mathbb{C}_2$, $p > 1$. In some cases, this is equivalent to the homogenization approach within a family of sub-optimal micro-geometries [11]. In any case, this approach does not lead to a well-posed problem. Practically, a SIMP-based implementation alone suffers from mesh dependencies (the smallest feature detected depends on the mesh size) and checkerboards (design patterns at the scale of the finite element mesh that are poorly approximated by low order finite elements). Thus, they are commonly used in conjunction with a filtering technique [37], where either the sensitivities or densities are averaged during optimization, which has been shown to lead to a well-posed problem [14]. Roughly speaking, introducing a non-local term in the response function (the filter) provides compactness of minimizing sequences of designs which combined with the lower semi-continuity of the objective function, is sufficient to prove existence of "classical" solutions. We will borrow these ideas for the optimal design of responsive structures to formulate a well-posed problem.

3.3 Optimizing Responsive Structures

3.3.1 Responsive Material

A responsive material is one that changes its shape and/or stiffness in response to a stimulus. These could include activated, ferroelectric, and magnetostrictive materials. The corresponding elastic energy density may be described as

$$W(\varepsilon, S) := \frac{1}{2}(\varepsilon(u) - \varepsilon^*(S)) \cdot \mathbb{C}(S)(\varepsilon(u) - \varepsilon^*(S)), \tag{3.2}$$

where $\varepsilon(u) = (\nabla u + \nabla u^T)/2$ is the linearized strain, $S \in [0, 1]$ the stimulus (assumed here to be a scalar), $\varepsilon^*(S)$ is the stimulus-dependent actuation or spontaneous strain, and $\mathbb{C}(S)$ is the possibly stimulus-dependent elastic modulus. We assume that $\varepsilon^*(0) = 0$.

We briefly describe actuation strains of different physical systems. For the case of a liquid crystal elastomer which transforms from an isotropic to nematic phase, the 3D spontaneous strain takes a volume-preserving, trans-

versely isotropic form

$$\varepsilon^* = \frac{3}{2}\gamma\left(a \otimes a - \frac{1}{3}I_{3\times 3}\right), \tag{3.3}$$

where a is a unit vector corresponding to the preferred nematic orientation and $\gamma > 0$ is the amplitude [17]. This corresponds to an extension along axis a by γ and a contraction along directions perpendicular to a by $\gamma/2$. The next transformation strain we consider is that of a hydrogel. Due to the uniform dilatation upon transformation, the spontaneous strain takes the form $\varepsilon^* = \frac{\alpha}{3}I_{n\times n}$, where α is the volumetric expansion. Of course, α may be either positive or negative to model swelling or shrinkage upon stimulation. Finally, we consider the transformation strain for a shape-memory alloy. Transforming from a low symmetry martensite phase to a high symmetry austenite phase upon temperature increase, the induced spontaneous strains depend heavily on the material composition. This can give rise to a transformation which may extend and shear [13].

3.3.2 Optimal Design

Consider an integrated functional structure occupying a bounded region $\Omega \subset \mathbb{R}^n$ of volume V, consisting of a structural material and a responsive material. Let $\chi_s, \chi_r : \Omega \mapsto \{0, 1\}$ be the characteristic functions of the regions the structural and responsive materials occupy. $\Phi := (\chi_s, \chi_r)$ then describes the design. The structural material may either be a stiff framework or a soft binder. In this section, we assume that there are no voids, i.e., $\chi_s + \chi_r = 1$.

Subject to a traction $f \in L^2(\partial_f\Omega)$ on $\partial_f\Omega$ and displacement u_0 on $\partial_u\Omega$, the energy function describing this structure for a given displacement field u under stimulus $S \in [0, 1]$ is

$$\mathcal{E}(\Phi, u, S) := \int_\Omega \frac{1}{2}\left[\chi_s\varepsilon(u)\cdot\mathbb{C}_s\varepsilon(u) + \chi_r(\varepsilon(u)-\varepsilon^*)\cdot\mathbb{C}_r(S)(\varepsilon(u)-\varepsilon^*)\right] dx - \int_{\partial_f\Omega} f\cdot u\, ds, \tag{3.4}$$

where $\mathbb{C}_s$ and $\mathbb{C}_r$ denote respectively the Hooke's laws of the structural and responsive materials. We assume that these Hooke's laws are non-degenerate in the sense that there exist 4 positive constants $0 < m_s, m_r, M_s, M_r$ such that

$$m_{r,s} \leq \mathbb{C}_{r,s}\eta\cdot\eta \leq M_{r,s} \tag{3.5}$$

for any symmetric n-dimensional second order tensor η with unit norm. The compliance of a design is

$$\mathcal{C}(\Phi, S) := \int_{\partial_f \Omega} f \cdot u \, ds, \tag{3.6}$$

where u is the displacement given by the equilibrium condition

$$u = \arg\min_{u \in \mathcal{U}} \ \mathcal{E}(\Phi, u, S), \tag{3.7}$$

where

$$\mathcal{U} := \{u \in W^{1,2}(\Omega) : u = u_0 \text{ on } \partial_u \Omega\}. \tag{3.8}$$

Equivalently, u satisfies

$$G(\Phi, S; u) := -\text{div}\left[\chi_s(x)\mathbb{C}_s\varepsilon(u) + \chi_r(x)\mathbb{C}_r(\varepsilon(u) - \varepsilon^*(S))\right] = 0, \tag{3.9}$$

subject to the boundary conditions. The task is to find the design Φ that minimizes an objective function, which we assume to be dependent on the compliances of two states with different stimuli. Thus, we consider a class of optimization problems

$$\inf_{\Phi \in \mathcal{D}} \ \mathcal{O}(\Phi) := \bar{\mathcal{O}}(\mathcal{C}(\Phi, S_1), \mathcal{C}(\Phi, S_2)), \tag{3.10}$$

where $\bar{\mathcal{O}} : \mathbb{R} \times \mathbb{R} \mapsto \mathbb{R}$ is a given continuous function, amongst the set of allowable designs:

$$\mathcal{D} = \{\Phi : \chi_r + \chi_s = 1 \text{ on } \Omega, \ \int_\Omega \chi_r \ dV \leq \bar{V}_r\}. \tag{3.11}$$

Here, we have specified the allowable designs such that the materials occupy the whole domain and consider a restriction on the volume of responsive material, where $\bar{V}_r \leq V$ is the maximum allowed. The above problem is often ill-posed, suffering from the same issues as that of the standard compliance optimization problem in (3.1). Thus, we introduce a SIMP interpolation and a filter as discussed in the previous section.

3.3.3 Reformulation Using Interpolation and Regularization

Consider the relaxed energy functional for the responsive structure with a SIMP interpolation of penalty factor $p > 1$,

$$\begin{aligned}\mathcal{E}_f(\phi, u, S) := \int_\Omega \frac{1}{2} \big[&(1 - (F * \phi)^p)\mathbb{C}_s\varepsilon(u) \cdot \varepsilon(u) \\ &+ (F * \phi)^p \mathbb{C}_r(S)(\varepsilon(u) - \varepsilon^*(S)) \cdot (\varepsilon(u) - \varepsilon^*(S))\big] \ dx \\ &- \int_{\partial_f \Omega} f \cdot u \ ds,\end{aligned} \tag{3.12}$$

where F is the filter function of characteristic length $R_f > 0$ satisfying

$$\begin{aligned} &F \in W^{1,2}(\mathbb{R}^n), \\ &\text{Supp}(F) \subset B_{R_f}, \\ &F \geq 0 \ \text{ a.e. in } \ B_{R_f}, \\ &\int_{B_{R_f}} F \ dx = 1, \end{aligned} \tag{3.13}$$

where B_{R_f} denotes the open ball of radius R_f of $\mathbb{R}^n$, and we define the convolution over the bounded region Ω as

$$(F * \phi)(x) := \int_\Omega F(x-y)\phi(y) \ dy. \tag{3.14}$$

The field $\phi : \Omega \mapsto [0,1]$ describes the topology, with regions of $\phi = 0$ and $\phi = 1$ corresponding to passive and active material, respectively. We assume the transformation strain $\varepsilon^*(S) \in L^2(\Omega)$. Notice that since the integral in (3.14) is over Ω, the filtered density near the boundary will not be able to take values near 1. In practice, we renormalize the convolution following the lines of [14] to avoid such boundary effects, as discussed in Section 3.5. The compliance of a design is, again,

$$\mathcal{C}(\phi, S) := \int_{\partial_f \Omega} f \cdot u \, ds, \tag{3.15}$$

where u is the displacement associated with the design Φ and stimulus S minimizing $\mathcal{E}_f(\phi, u, S)$. It should be noted that under the assumptions on $\mathbb{C}_s$ and $\mathbb{C}_r$ in (3.5), u is the unique solution of the Euler-Lagrange equations.

$$\mathcal{Q}_f(\phi, u, v, S) = 0 \quad \forall \ v \in \mathcal{U}_0, \tag{3.16}$$

with

$$\begin{aligned} \mathcal{Q}_f(\phi, u, v, S) := \int_\Omega &[(1 - (F*\phi)^p)\mathbb{C}_s\varepsilon(u)\cdot\varepsilon(v) \\ &+(F*\phi)^p\mathbb{C}_r(S)(\varepsilon(u) - \varepsilon^*(S))\cdot(\varepsilon(v))] \ dx \\ &- \int_{\partial_f\Omega} f \cdot v \ ds, \end{aligned} \tag{3.17}$$

and

$$\mathcal{U}_0 := \{u \in W^{1,2}(\Omega) : u = 0 \text{ on } \partial_u\Omega\}. \tag{3.18}$$

We again consider the class of optimization problems

$$\inf_{\phi \in \mathcal{D}_f} \ \mathcal{O}(\phi) := \bar{\mathcal{O}}(\mathcal{C}(\phi, S_1), \mathcal{C}(\phi, S_2)), \tag{3.19}$$

where we optimize over the set

$$\mathcal{D}_f := \left\{ \phi : \phi(x) \in [0,1] \ \text{ a.e. on } \Omega, \int_\Omega \phi \, dx \leq \bar{V}_r \right\}. \tag{3.20}$$

Remark 1. *Ellipticity: From the definition of $\mathcal{D}$, the properties of the Hooke's laws* (3.5)*, and the properties of the filter, there exists a constant $m > 0$, only depending on Ω and S such that for any ϕ and $u \in \mathcal{U}$ the following holds:*

$$\int_\Omega \frac{1}{2} \left[(1 - (F * \phi)^p) \mathbb{C}_s \varepsilon(u) \cdot \varepsilon(u) \right. \\ \left. + (F * \phi)^p \mathbb{C}_r(S) \varepsilon(u) \cdot \varepsilon(u) \right] \, dx \geq m \|u\|^2_{W^{1,2}(\Omega)}. \tag{3.21}$$

3.3.4 Existence of Solutions

We establish the existence of solutions to (3.10) through the following theorem in this section

Theorem 3.3.1. *Recall the definition of the compliances from* (3.15)*, and set*

$$\mathcal{O}(\phi) := \bar{\mathcal{O}}(\mathcal{C}(\phi, S_1), \mathcal{C}(\phi, S_2)), \tag{3.22}$$

where $\bar{\mathcal{O}}$ is bounded below and continuous. There exists a $\bar{\phi} \in \mathcal{D}_f$ such that,

$$\mathcal{O}(\bar{\phi}) = \inf_{\phi \in \mathcal{D}_f} \mathcal{O}(\phi). \tag{3.23}$$

The proof of the theorem extends the strategy of Bourdin [14] that established existence in compliance optimization. We first provide a brief synopsis of the proof. The key idea is that the filter prevents any fine scale oscillations in the optimization problem. Precisely, the regularization provided by the filter provides weak continuity of the compliances in both the actuated and un-actuated states. Thus, we can consider any minimizing sequence to the optimization problem, show that it is uniformly bounded, extract a subsequence and pass to the limit in both the compliance in both the actuated and un-actuated states. Further, since we assume the objective to be continuous in these compliances, we can pass to the limit in the compliances and existence follows.

Remark 2. *While density filtering is used here for regularization, this analysis can be straightforwardly extended to other methods so long as we recover strong convergence of the elliptic operator. This includes approaches such as PDE filtering [24] and perimeter penalization [22].*

We now turn to the proof. We need the following lemma, which establishes the weak continuity of the solutions to the elliptic problem and whose proof is provided in Appendix 3.A.

Lemma 3.3.2. *Let $\{u_k\} \subset \mathcal{U}$ be the sequence of equilibrium solutions to* (3.16) *corresponding to sequence $\{\phi_k\} \subset \mathcal{D}_f$ for some fixed S. If*

$$(F * \phi_k)^p \to (F * \bar{\phi})^p \text{ uniformly on } \Omega \text{ when } k \to +\infty \tag{3.24}$$

then

$$u_k \rightharpoonup \bar{u} \text{ in } W^{1,2}(\Omega) \text{ when } k \to +\infty, \tag{3.25}$$

up to a subsequence, where $\bar{u} \in \mathcal{U}$ is the equilibrium configuration corresponding to $\bar{\phi} \in \mathcal{D}_f$.

Proof of Theorem 3.3.1. Let $\{\phi_k\} \subset \mathcal{D}_f$ be a minimizing sequence for (3.23). $\mathcal{D}_f$ implies that ϕ_k is uniformly bounded in $L^2(\Omega)$ and thus there exists $\bar{\phi} \in \mathcal{D}_f$ such that

$$\phi_k \rightharpoonup \bar{\phi} \text{ in } L^2(\Omega) \text{ when } k \to +\infty, \tag{3.26}$$

up to a subsequence. Because $F \in L^2(\mathbb{R}^n)$,

$$(F*\bar{\phi})(x) - \lim_{k\to\infty} (F*\phi_k)(x) = \lim_{k\to\infty} \int_\Omega F(x-y)\left(\bar{\phi}(y) - \phi_k(y)\right)\, dy = 0. \tag{3.27}$$

Since this holds for all $x \in \Omega$,

$$F * \phi_k \to F * \bar{\phi} \text{ uniformly on } \Omega \text{ when } k \to +\infty. \tag{3.28}$$

Because $(F * \phi)(x)$ is bounded for all $\phi \in \mathcal{D}_f$,

$$(F * \phi_k)^p \to (F * \bar{\phi})^p \text{ uniformly on } \Omega \text{ when } k \to +\infty. \tag{3.29}$$

Let $u_{1k}, u_{2k} \in \mathcal{U}$ be the equilibrium solutions to (3.16) corresponding to ϕ_k for $S = S_1$ and $S = S_2$, respectively:

$$u_{1k} = \arg\min_{u\in\mathcal{U}} \mathcal{E}_f(\phi_k, u, S_1), \qquad u_{2k} = \arg\min_{u\in\mathcal{U}} \mathcal{E}_f(\phi_k, u, S_2). \tag{3.30}$$

Then, from Lemma 3.3.2,

$$\begin{aligned} u_{1k} &\rightharpoonup \bar{u}_1 \text{ in } W^{1,2}(\Omega) \text{ when } k \to +\infty, \\ u_{2k} &\rightharpoonup \bar{u}_2 \text{ in } W^{1,2}(\Omega) \text{ when } k \to +\infty, \end{aligned} \tag{3.31}$$

where $\bar{u}_1, \bar{u}_2 \in \mathcal{U}$ are the equilibrium configurations corresponding to $\bar{\phi}$ for $S = S_1$ and $S = S_2$:

$$\bar{u}_1 = \arg\min_{u \in \mathcal{U}} \ \mathcal{E}_f(\bar{\phi}, u, S_1), \qquad \bar{u}_2 = \arg\min_{u \in \mathcal{U}} \ \mathcal{E}_f(\bar{\phi}, u, S_2). \tag{3.32}$$

Because $(\bar{u}_1 - u_{1k}) \in \mathcal{U}_0$, $\mathcal{Q}_f(\bar{\phi}, \bar{u}_1, (\bar{u}_1 - u_{1k}), S) = 0$. Then, using the definition of the compliance (3.15) and the weak convergence of u_{1k} to $\bar{u}_1$,

$$\lim_{k \to \infty} \ \mathcal{C}(\phi_k, S_1) = \mathcal{C}(\bar{\phi}, S_1). \tag{3.33}$$

Likewise,

$$\lim_{k \to \infty} \ \mathcal{C}(\phi_k, S_2) = \mathcal{C}(\bar{\phi}, S_2). \tag{3.34}$$

It follows

$$\lim_{k \to \infty} \ \bar{\mathcal{O}}(\mathcal{C}(\phi_k, S_1), \mathcal{C}(\phi_k, S_2)) = \bar{\mathcal{O}}(\mathcal{C}(\bar{\phi}, S_1), \mathcal{C}(\bar{\phi}, S_2)). \tag{3.35}$$

Therefore,

$$\lim_{k \to \infty} \ \mathcal{O}(\phi_k) = \mathcal{O}(\bar{\phi}). \tag{3.36}$$

Since ϕ_k is a minimizing sequence,

$$\mathcal{O}(\bar{\phi}) = \inf_{\phi \in \mathcal{D}} \ \mathcal{O}(\phi). \tag{3.37}$$

□

3.3.5 Sensitivities Through the Adjoint Method

We solve the optimal design problem using a gradient-based approach. To do so, we need to compute the directional derivative of the objective function with respect to a design changes. To this end, we utilize an adjoint approach. Consider u_1 and u_2 associated with $S = S_1$ and $S = S_2$ which satisfy (3.16) for some design $\phi \in \mathcal{D}_f$. To find the directional derivative of some functional $\mathcal{F}(\phi, u_1, u_2)$, we introduce the augmented objective $\mathcal{L}(\phi, u_1, u_2, \lambda_1, \lambda_2) = \mathcal{F}(\phi, u_1, u_2)$ for any $\lambda_1, \lambda_2 \in \mathcal{U}_0$,

$$\begin{aligned}\mathcal{L}(\phi, u_1, u_2, \lambda_1, \lambda_2) := \mathcal{F}(\phi, u_1, u_2) + \mathcal{Q}_f(\phi, u_1, \lambda_1, S_1) \\ + \mathcal{Q}_f(\phi, u_2, \lambda_2, S_2).\end{aligned} \tag{3.38}$$

One can easily show that the directional derivative of $\mathcal{F}$ in the direction $\tilde{\phi}$ is

$$\mathcal{F}'(\phi)\tilde{\phi} = \mathcal{F}_{,\phi}(\phi, u_1, u_2)\tilde{\phi} + \mathcal{Q}_{f,\phi}(\phi, u_1, \lambda_1^*, S_1)\tilde{\phi} + \mathcal{Q}_{f,\phi}(\phi, u_2, \lambda_2^*, S_2)\tilde{\phi}, \tag{3.39}$$

where $\lambda_1^*, \lambda_2^* \in \mathcal{U}_0$ are solutions of the uncoupled adjoint equations

$$\begin{cases} \mathcal{F}_{,u_1}(\Phi, u_1, u_2)\tilde{u} + \mathcal{Q}_{f,u_1}(\phi, u_1, \lambda_1^*, S_1)\tilde{u} = 0 \quad \forall \ \tilde{u} \in \mathcal{U}_0, \\ \mathcal{F}_{,u_2}(\Phi, u_1, u_2)\tilde{u} + \mathcal{Q}_{f,u_2}(\phi, u_2, \lambda_2^*, S_2)\tilde{u} = 0 \quad \forall \ \tilde{u} \in \mathcal{U}_0. \end{cases} \tag{3.40}$$

3.4 Objective Functions

3.4.1 General Workpiece Objective

We discuss a variety of objective functions used to characterize actuating systems. We define the general *workpiece objective* to be

$$\bar{\mathcal{O}}(\mathcal{C}(\phi,0),\mathcal{C}(\phi,1)) = \frac{\kappa\mathcal{C}(\phi,1)+1}{\kappa\mathcal{C}(\phi,0)+1}, \tag{3.41}$$

where $\kappa \in (0,+\infty)$ is a parameter. In the case where f is a point load in direction $\hat{n}$ at point x_0, this objective is equivalent to maximizing the force carried by a linear elastic spring in direction $\hat{n}$ of stiffness κ attached at x_0 (see Appendix 3.B). Further, this objective is dependent on the compliances of the stimulated and unstimulated states and therefore satisfies the conditions of Theorem 3.3.1. This workpiece objective has interesting limits when the parameter tends to either zero or infinity.

First, consider the limit of small κ. Using the Taylor expansion of (3.41) about $\kappa = 0$,

$$\frac{\kappa\mathcal{C}(\phi,1)+1}{\kappa\mathcal{C}(\phi,0)+1} \approx 1+\kappa\left(\mathcal{C}(\phi,1)-\mathcal{C}(\phi,0)\right). \tag{3.42}$$

Thus, for small κ, the workpiece objective is equivalent to the difference in compliance. We show in Section 3.4.2 that this is equivalent to the *work of actuation*. Additionally, we will show that this is a measure of flexibility as it is equivalent to maximizing the displacement of actuation in a particular direction.

Next, consider the limit of large κ:

$$\lim_{\kappa\to+\infty} \frac{\kappa\mathcal{C}(\phi,1)+1}{\kappa\mathcal{C}(\phi,0)+1} = \frac{\mathcal{C}(\phi,1)}{\mathcal{C}(\phi,0)}. \tag{3.43}$$

For large κ, the workpiece objective reduces to a ratio of compliances, which we will show is equivalent to the *blocking load objective* in Section 3.4.3. Because it is a ratio of stimulated to unstimulated compliances, this objective considers not only the actuation flexibility, but also the unstimulated stiffness.

3.4.2 Work of Actuation

The work of actuation is the work done against the applied load f as we go from the unactuated to the actuated states:

$$\mathcal{O}(\Phi) := -\int_{\partial_f\Omega} f\cdot(u_{S=1}-u_{S=0})\,ds = \mathcal{C}(\Phi,0)-\mathcal{C}(\Phi,1). \tag{3.44}$$

The identity follows from (3.6) and shows that the work of actuation is equal to the difference in compliance. To get further insight into this objective, consider the case where the modulus of the responsive material is independent of the stimulus. Using (3.9), the objective (3.44) can now be written as

$$\mathcal{O}(\Phi) = -\int_{\partial_f\Omega} f \cdot v \; ds, \tag{3.45}$$

where v satisfies

$$\begin{cases} -\mathrm{div}\left[\chi_s(x)\mathbb{C}_s\varepsilon(v) + \chi_r(x)\mathbb{C}_r\varepsilon(v)\right] = -\mathrm{div}\left[\chi_r(x)\mathbb{C}_r\varepsilon^*(1)\right] & \text{in } \Omega, \\ v = 0 & \text{on } \partial_u\Omega, \\ \left[\chi_s(x)\mathbb{C}_s\varepsilon(v) + \chi_r(x)\mathbb{C}_r\varepsilon(v)\right] n = \left[\chi_r(x)\mathbb{C}_r\varepsilon^*(1)\right] n & \text{on } \partial_f\Omega. \end{cases} \tag{3.46}$$

The solution v to (3.46) is the displacement induced in the structure due to only the spontaneous strain field $\chi_r(x)\mathbb{C}_r\varepsilon^*(1)$, and may be expressed as $v = \Gamma_\Phi\chi_r(x)\mathbb{C}_r\varepsilon^*(1)$ for the appropriate operator Γ_Φ. Thus, our optimal design problem is

$$\inf_{\Phi\in\mathcal{D}} \int_{\partial_f\Omega} f \cdot \left[\Gamma_\Phi\chi_r(x)\mathbb{C}_r\varepsilon^*(1)\right] \; ds, \tag{3.47}$$

or finding the arrangement of the responsive material that maximizes the resulting spontaneous displacement in the direction of f. Thus, the actuation work objective is a measure of flexibility upon stimulation.

3.4.3 Blocking Load

The blocking load is the magnitude of the applied load that nullifies the actuation. Consider the external traction as scaled by a nonzero constant $\alpha \in \mathbb{R}$, $f = \alpha\bar{f}$, where $\bar{f}$ is some (unit) loading profile. The blocking load is the value of α for which the displacement of the actuated structure in the direction of the loading profile vanishes

$$\mathcal{O}(\Phi) := \alpha \quad \text{where} \quad \mathcal{C}_\alpha(\Phi, 1) = \int_{\partial_f\Omega} \bar{f} \cdot u_{f=\alpha\bar{f},S=1} ds = 0. \tag{3.48}$$

We now show that this is equivalent to the ratio of compliances. From (3.44) and (3.45),

$$\mathcal{C}_\alpha(\Phi, 1) = \mathcal{C}_\alpha(\Phi, 0) + \int_{\partial_f\Omega} f \cdot v \, ds = \int_{\partial_f\Omega} f \cdot \left(u_{S=0,\alpha\bar{f}} + v\right) ds \tag{3.49}$$

where v solves (3.46) and is independent of f, and $u_{S=0,\alpha\bar{f}}$ minimizes the elastic energy (3.4) with $S = 0$ and $f = \alpha\bar{f}$. Assuming homogeneous Dirichlet

conditions $u_0 = 0$ on $\partial_u\Omega$, it is easy to see using the linearity of the Euler-Lagrange equations that $u_{S=0,\alpha\bar{f}} = \alpha u_{S=0,\bar{f}}$. Therefore, the zero compliance condition $\mathcal{C}_\alpha(\Phi, 1) = 0$ can then be written as

$$0 = \int_{\partial_f\Omega} f \cdot (\alpha\ \bar{u}_{S=0,\bar{f}} + v)\, ds = \alpha \int_{\partial_f\Omega} \bar{f} \cdot (\alpha\ \bar{u}_{S=0,\bar{f}} + v)\, ds, \tag{3.50}$$

or

$$0 = \int_{\partial_f\Omega} \bar{f} \cdot (\alpha\ \bar{u}_{S=0,\bar{f}} + v)\, ds. \tag{3.51}$$

The loading amplitude is then

$$\alpha = -\frac{\int_{\partial_f\Omega} \bar{f} \cdot v\, ds}{\int_{\partial_f\Omega} \bar{f} \cdot\ \bar{u}_{S=0,\bar{f}}\, ds} = -\frac{\int_{\partial_f\Omega} \bar{f} \cdot \bar{u}_{S=1,\bar{f}}\, ds}{\int_{\partial_f\Omega} \bar{f} \cdot\ \bar{u}_{S=0,\bar{f}}\, ds} + 1 = -\frac{\mathcal{C}_1(\Phi, 1)}{\mathcal{C}_1(\Phi, 0)} + 1. \tag{3.52}$$

It follows that the blocking load objective is equivalent to minimizing the ratio of the stimulated to unstimulated compliance under fixed load

$$\inf_{\Phi\in\mathcal{D}}\ \mathcal{O}(\Phi) = \frac{\mathcal{C}(\Phi, 1)}{\mathcal{C}(\Phi, 0)}. \tag{3.53}$$

We conclude with the comment comparing the two objectives, the work of actuation and the blocking load. Recalling the first identity in (3.49), we see that

$$\frac{\mathcal{C}_1(\Phi, 1)}{\mathcal{C}_1(\Phi, 0)} = 1 + \frac{1}{\mathcal{C}_1(\Phi, 0)} \int_{\partial_f\Omega} f \cdot v\, ds \tag{3.54}$$

Thus, the blocking load objective is the ratio of the work of actuation objective to the compliance of the unstimulated structure. Thus, the blocking load objective leads to a structure that balances the work of actuation and the stiffness of the structure. Finally, these objectives become equivalent when the moduli of the structural and responsive materials are equal, i.e., when $\mathbb{C}_s = \mathbb{C}_r$. This is because the compliance of the unstimulated state is independent of the design, i.e., $\mathcal{C}(\Phi, 0) = C$ is independent of Φ.

3.5 Examples of Optimal Responsive Structures

Here, we explore optimal designs for 2D rectangular lifting actuators. We present results for both the actuation work and blocking load objective, where each are computed under identical computational frameworks.

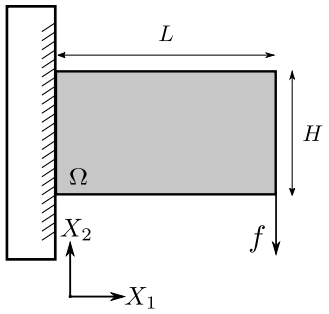

Figure 3.1: 2D Cantilever of length L and height H. The left edge at $X_1 = 0$ is fixed rigidly to the wall, with an applied point load f in the bottom right corner.

Consider a 2D rectangular domain $\Omega = (0, L) \times (0, H)$ as shown in Figure 3.1. We take the elastic modulus of both the responsive and structural materials to be isotropic and independent of actuation. We discretize with standard $p = 1$ Lagrange polynomial shape functions on a quadrilateral mesh through the C++ deal.II finite element library [10]. The density variable ϕ is taken to be constant on each element. As described in the previous section, we use a SIMP interpolation and density filter for regularization. We employ a discrete renormalizing filter as described in [14]. This ensures that the density variable is able to take values of $\phi = 1$ near the boundary. Denoting ϕ_k as the constant density value of element k, and $V(k)$ the set of elements located within distance R_f from element k, the filtered density value on element k is

$$(F * \phi)_k = \frac{\sum_{i \in V(k)} \left(\phi_i \int_i F(x - c_k)\, dx \right)}{\sum_{i \in V(k)} \int_i F(x - c_k)\, dx}, \tag{3.55}$$

where c_k is the center of element k. Sensitivities are calculated using the adjoint method, and the density is updated using the method of moving asymptotes (MMA) subject to the linear constraint on total responsive material [41]. Following convergence of these pixelated designs, a MATLAB® code traces smooth contours on the boundaries of the passive and active material domains. We initialize the design to uniform $\phi = \bar{V}_r/V$, and begin iterations thereafter.

3.5.1 Optimizing the Work of Actuation

We present optimal designs for the lifting actuator optimized for actuation work. Figure 3.2 shows the converged designs for a spontaneous strain of

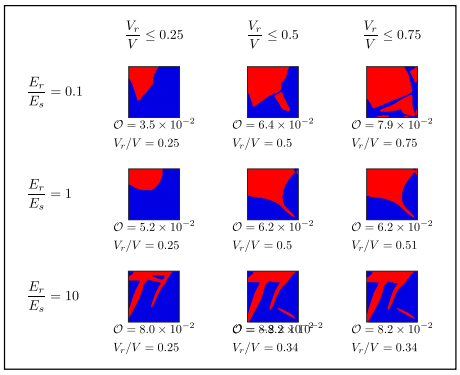

(a) $L/H = 1$

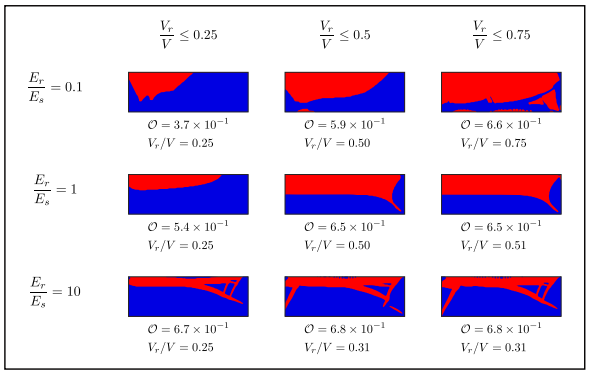

(b) $L/H = 3$

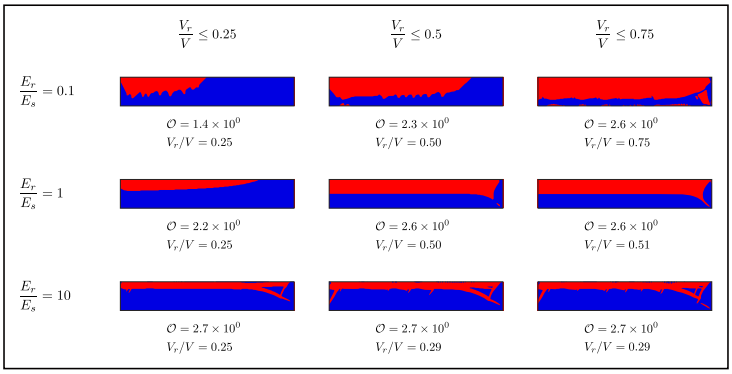

(c) $L/H = 6$

Figure 3.2: Converged bimorph designs for optimal work done through actuation. The red and blue regions are the active and passive materials, respectively. Varying aspect ratios, stiffness ratios, and responsive material volume constrains are considered. A Poisson ratio of $\nu = 0.3$ is used for both the passive and responsible materials. Normalized actuation work and volume ratios of the converged designs are shown.

$\varepsilon^*(1) = -0.1e_1 \otimes e_1 + 0.1e_2 \otimes e_2$ (elongation along the horizontal and extension along the vertical) in the responsive material upon stimulation, where $\{e_i\}$ is the standard basis aligned with the axis shown. We investigate these designs for varying domain aspect ratios L/H, responsive material volume constraints $\bar{V}_r/V$, and stiffness ratio E_r/E_s of the responsive to passive material. These were computed on uniform finite element meshes of 60×60, 60×180, and 60×360 for aspect ratios of $L/H = 1$, 3, and 6, respectively. The filter radius was taken to be 1.5 times the element width.

Figure 3.2 (a), (b) and (c) shows the designs for aspect ratios of $L/H = 1$, 3, and 6 respectively. For each aspect ratio, the rows show the designs for fixed ratio of elastic moduli E_r/E_s as the allowable ratio of active to passive

material V_r/V is varied. Similarly, the columns show the designs for fixed allowable ratio of active to passive material V_r/V but varying ratio of elastic moduli E_r/E_s. Note that the ratio of responsive to passive material V_r/V is imposed as an inequality constraint: the actual ratio used is indicated below each design. Finally, the optimal value of the objective is also indicated below each design.

To understand these results, we start with Figure 3.2 (b) where $L/H = 3$, and specifically with the middle row where $E_r/E_s = 1$. The design is similar to the bi-material strip with the active material on the top and passive material on the bottom. When stimulated, the active material contracts horizontally, causing the domain to bend upward and perform work against the load. When the allowed volume fraction of responsive material is small (left), the design uses the entire allowed volume fraction and places it close to the support since it can provide the maximum moment against the load. As the allowed volume fraction of responsive material increases, the design continues to use the entire allowed volume fraction with roughly a uniform thickness. However, at large allowed volume fraction (right), the design does not use the full allocation. Instead, it saturates at about 51% because it needs a sufficient amount of passive material to convert its horizontal contraction into work against the vertical load. The value of the objective increases with the allowed volume fraction of responsive material, but saturates when the volume fraction does.

The designs remain roughly similar as we change the ratio of the stiffness of the responsive material to that of the structural material (E_r/E_s). The design uses more responsive material when it is more compliant (top row of Figure 3.2 (b)), as it requires more of the responsive material to actuate against the stiffer structural material. The opposite is true when the responsive material is stiffer (bottom row). The value of the objective increases with the relative stiffness of the responsive material when we fix the allowed volume fraction (columns); however, the saturated value when we allow sufficient volume fraction is relatively independent of the stiffness ratio.

We now study the effect of aspect ratio L/H comparing the designs of Figure 3.2 (b) with those in Figure 3.2 (a, c). The designs and the trends against allowable volume fraction of responsive material and stiffness ratio are similar (except for high stiffness of the responsive material and short aspect ratio where the design has diagonal laminates to provide stiffness against shear).

The optimal value increases with aspect ratio.

3.5.2 Optimizing the Blocking Load

We consider the same domain and loading as described in Figure 3.1, and look to optimize the blocking load applied to the bottom right corner. The numerical schemes are identical, with the only difference being the objective function. Figure 3.3 shows the converged designs for a spontaneous strain of $\varepsilon^*(1) = -0.1e_1 \otimes e_1 + 0.1e_2 \otimes e_2$ in the responsive material upon stimulation. The designs and the trends are broadly similar to those obtained by optimizing the work of actuation. When the stiffnesses of the two materials are the same ($E_r/E_s = 1$) the designs coincide since the objectives are identical as noted above. In the other situations, the blocking load designs tend to use more stiffer material (more structural material when $E_r/E_s = 0.1$ and more responsive material when $E_r/E_s = 10$). We also see more diagonal reinforcement.

3.6 Optimizing Responsive Structures with Voids

Motivated by a structural frame actuated by muscle-like actuators, we now consider a responsive structure with voids or holes in the domain. We now have $\chi_s + \chi_r \leq 1$. We introduce a SIMP interpolation and filter as before through an additional density variable. We consider $\rho : \Omega \mapsto [\rho_{min}, 1]$ for some $1 >> \rho_{min} > 0$, which determines void or solid and consider the energy functional

$$\mathcal{E}_v(\phi, \rho, u, S) := \int_\Omega (F * \rho)^p \left(\frac{1}{2}\right) \Big[(1 - (F * \phi)^p)\mathbb{C}_s\varepsilon(u) \cdot \varepsilon(u) + (F * \phi)^p \mathbb{C}_r(S)(\varepsilon(u) - \varepsilon^*(S)) \cdot (\varepsilon(u) - \varepsilon^*(S))\Big]\, dx - \int_{\partial_f\Omega} f \cdot u \; ds. \quad (3.56)$$

The compliance is, again,

$$\mathcal{C}(\phi, \rho, S) = \int_{\partial_f\Omega} f \cdot u \; ds, \quad (3.57)$$

where u is an equilibrium solution,

$$u = \arg\min_{u \in \mathcal{U}} \; \mathcal{E}_v(\phi, \rho, u, S). \quad (3.58)$$

Note that the voids have some residual stiffness since $\rho_{min} > 0$ to maintain the coercivity of (3.56). We choose this small enough so that it has only a limited

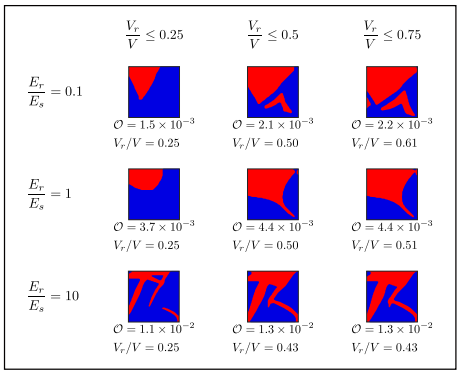

(a) $L/H = 1$

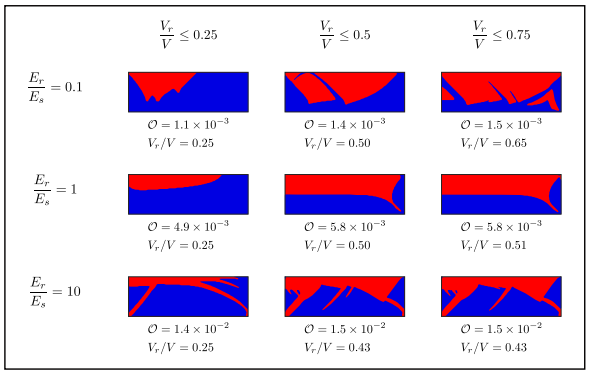

(b) $L/H = 3$

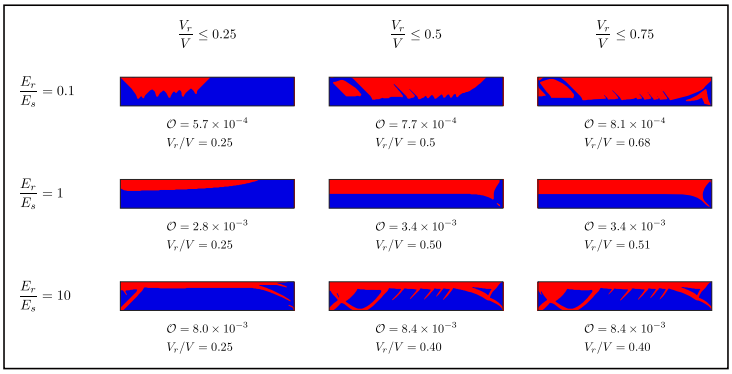

(c) $L/H = 6$

Figure 3.3: Converged bimorph designs for optimal actuation blocking load. The red and blue regions are the active and passive materials, respectively. Varying aspect ratios, stiffness ratios, and responsive material volume constrains are considered. A Poisson ratio of $\nu = 0.3$ is used for both the passive and responsible materials. Normalized blocking load values and volume ratios of the converged designs are shown.

effect on the resulting designs. We again consider a compliance dependent objective

$$\inf_{\phi \in \mathcal{D}_f,\ \rho \in \mathcal{R}_f} \mathcal{O}(\phi, \rho) := \bar{\mathcal{O}}(\mathcal{C}(\phi, \rho, S_1), \mathcal{C}(\phi, \rho, S_2)), \tag{3.59}$$

where we optimize over the space of feasible designs

$$\begin{aligned} \mathcal{D}_f &= \left\{ \phi : \phi \in [0,1] \text{ a.e. in } \Omega, \int_\Omega \rho\phi \, dx \leq \bar{V}_r \right\}, \\ \mathcal{R}_f &= \left\{ \rho : \rho \in [\rho_{min}, 1] \text{ a.e. in } \Omega, \int_\Omega \rho \, dx \leq \bar{V}_0 \right\}, \end{aligned} \tag{3.60}$$

where $\bar{V}_0$ and $\bar{V}_r$ are the allowed volumes total material and responsive material, respectively.

Theorem 3.6.1. *Recall the definition of the compliances from* (3.57)*, and set*

$$\mathcal{O}(\phi, \rho) := \bar{\mathcal{O}}(\mathcal{C}(\phi, \rho, S_1), \mathcal{C}(\phi, \rho, S_2)), \tag{3.61}$$

where $\bar{\mathcal{O}}$ *is bounded below and continuous. There exists a* $\bar{\phi} \in \mathcal{D}_f$ *and* $\bar{\rho} \in \mathcal{R}_f$ *such that,*

$$\mathcal{O}(\bar{\phi}, \bar{\rho}) = \inf_{\phi \in \mathcal{D}_f,\ \rho \in \mathcal{R}_f} \mathcal{O}(\phi, \rho). \tag{3.62}$$

Proof. The weak continuity results from Lemma 3.3.2 can be extended for the additional filtered density field ρ. The rest of the proof follows the same steps as the proof for Theorem 3.3.1. □

We now consider the two objectives that we introduced in the previous section. We begin with the work of actuation in Section 3.5.1 which is the difference between the compliances in the stimulated and unstimulated states. However, the compliances are not bounded since we have voids[1]. Thus, this objective does not satisfy the hypothesis of the theorem, and a brute-force implementation does not converge to meaningful designs.

So we focus on the blocking load or mechanical advantage introduced in Section 3.5.2. Since this objective considers the ratio of the two compliances, it remains bounded satisfying the hypothesis of the theorem above. Specifically, we consider the optimization problem

$$\inf_{\phi \in \mathcal{D}_f,\ \rho \in \mathcal{R}_f} \mathcal{O}(\phi) = \frac{\mathcal{C}(\phi, \rho, 1)}{\mathcal{C}(\phi, \rho, 0)}. \tag{3.63}$$

The numerical schemes are nearly identical to the case of no holes, except for an additional density field. We consider this density variable constant on each element. We adopt a sequential update scheme to handle the nonlinear constraint posed in (3.60). After obtaining sensitivities through the adjoint method, the discrete ρ's are updated using MMA under the linear constraint of allowable material. Then, using the newly updated ρ's to write the constraint as linear, we update the ϕ's with another MMA. This results in only applying linear constraints for updates.

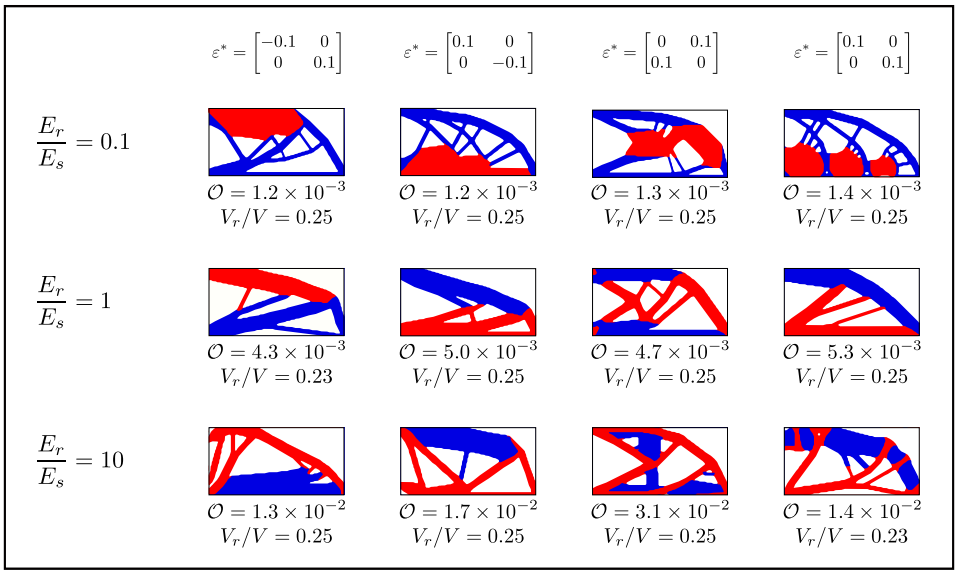

Figure 3.4: Converged designs for maximum blocking load of a 2D cantilever structure with aspect ratio $L/H = 2$. The inequality constraints $V_0/V \leq 0.5$ and $V_r/V \leq 0.25$ are enforced for all cases. The red and blue regions are the active and passive materials, respectively. Designs are shown for varying stiffness ratios for different spontaneous strains. A Poisson ratio of $\nu = 0.3$ is used for both the passive and responsible materials. Normalized blocking load values and converged responsive material volume ratios are shown. In all cases, the designs converged to $V_0/V = 0.5$.

3.6.1 Example in Two Dimensions: Lifting Actuator

We look to optimize the blocking load applied to the bottom right corner of Figure 3.1. We consider a domain aspect ratio of $L/H = 2$, and a uniform finite element mesh of 60×120 quadrilateral elements. The filter radius for both of the SIMP variables is taken as 1.5 times the element width, $R_f = 0.0125L$. We constrain the responsive materials to be a quarter of less of the total area ($V_r/V \leq 0.25$), and the combination of the structural and responsive materials to be less than half the total area ($V_0/V \leq 0.5$). The designs are all initialized to uniform $\phi = \bar{V}_r/\bar{V}_0$ and $\rho = \bar{V}_0/V$.

Figure 3.4 shows converged designs following contour smoothing in MATLAB®. Designs are shown for various spontaneous strains of responsive material and various ratios of the stiffnesses of the responsive and structural materials: the columns have the same spontaneous strain while the rows have the same stiffness ratio. Consider the first column where the spontaneous strain contracts

[1]Precisely, it is bounded by a constant that depends on ρ_{min} and becomes unbounded as $\rho_{min} \to 0$

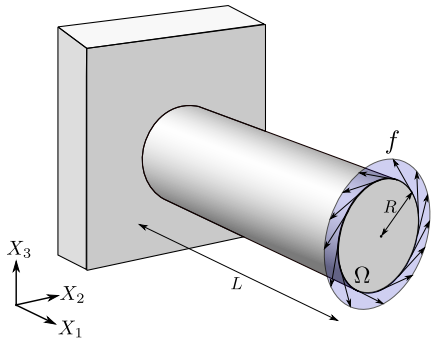

Figure 3.5: Cylindrical geometry for the torsional actuator of radius R and length L. The face at $X_1 = 0$ is fixed rigidly to the wall, and the far edge at $X_1 = L$ has uniform tangential loading.

along the horizontal and expands along the vertical. As in the situation without the voids (Figure 3.2), the active material is concentrated on the top. Also as before, in the cases of large stiffness contrast we see thick domains of the softer material, whether that be passive or responsive. However, in this situation, the stiffer material resembles a frame as in the classical problem of optimizing the compliance under a volume constraint.

The overall shape remains similar even when the spontaneous strain of responsive materials change. However, the placement of the responsive material changes significantly. For example, in the second column where the spontaneous strain is an elongation along the horizontal direction and contraction along the vertical, the responsive material is concentrated at the bottom. It should be noted that in all of these cases the designs saturated the total allowed material, converging to $V_0/V = 0.5$. Additionally, nearly all of the designs saturated the constraint on responsive material.

3.6.2 Example in Three Dimensions: Torsional Actuator

Thus far we have only considered the design of plane strain 2D structures. Here, we study the 3D design of a torsional actuator for optimal blocking load. We consider the cylindrical domain shown in Figure 3.5, with one face completely fixed to a wall and uniform tangential loading applied to its far edge. Optimizing the blocking load under this loading is analogous to maximizing the blocking torque of the actuator. We consider the formulation of the previous section for two materials with voids, with identical numerical schemes.

We consider a cylindrical domain of aspect ratio $L/R = 4$, computed on a finite element mesh of 245,760 hexahedral elements. This corresponds to a characteristic element side length of about $L/100$. To account for the variability in element sizes, the filter radius was taken rather large at 3 times this length or $R_f = 0.03L$. We investigate varying total material volume constraints V_0/V, and stiffness ratios E_r/E_s of the responsive to passive material. We consider the volume of responsive material to be constrained to $V_r/V_0 \leq 0.5$. Thus, we restrict the amount of responsive material to be less than half the amount of total material in the domain. We consider two cases of spontaneous strain upon stimulation: a transversely isotropic elongation along X_1 and contractions in the $X_2 - X_3$ plane, as well as isotropic contraction.

Figure 3.6 shows converged designs of the torsional actuator for a transversely isotropic transformation strain of $\varepsilon^*(1) = 0.1e_1 \otimes e_1 - 0.05e_2 \otimes e_2 - 0.05e_3 \otimes e_3$. As one would expect, we see the responsive material is arranged helically towards the outer edges of the domain. Similarly to the 2D case, for $E_r/E_s = 0.1$ we see thicker clumps of responsive material, where for $E_r/E_s = 10$ it is spread more thinly. For $V_0/V = 0.25$, the material is mostly concentrated towards the outer edges of the domain, with more material near the center for $V_0/V = 0.5$. This is understandable, as torsional stiffness is maximized by placing material farther from the center.

Figure 3.7 shows converged designs for the torsional actuator for an isotropic transformation strain of $\varepsilon^*(1) = -0.033\ I_{3\times3}$. The general trends outlined in the previous discussion remain valid. However, the direction of the helical responsive material now goes in the opposite direction, as the responsive material now contracts rather than expands along the X_1 direction.

For both cases of spontaneous strains, the designs completely saturate the total allowed material converging to $V_0 = \bar{V}_0$. Additionally, the volume of responsive material is nearly saturated in all cases.

In the previous 2D cases, the gradients of the objective with the design variables for the initial uniform density designs were sizeable. This lead to fast convergence through the MMA algorithm from initialization. However, for the 3D torsional actuator, the gradients of the blocking load objective with the design variable ϕ were nearly zero for a uniform density design, especially in the case of $E_r/E_s = 1$. This resulted in dozens of early iterations with small changes to design. To remedy this, we consider an initial nonuniform

configuration

$$\phi(X_1, X_2, X_3) = (V_r/V) + \epsilon \cos\left(2\theta - \frac{2\pi X_1}{L}\right), \tag{3.64}$$

where $\theta = \tan^{-1}(X_3/X_2)$. $\epsilon = 0.05$ was used for the previously described designs. This initial design is a small perturbation towards a helical ϕ with two "strands" running along the X_1 axis. This is the reason that the converged designs all have two main "strands" of responsive material. While the form of the perturbation may seem presumptuous, the magnitude of the perturbation was small. We also used the same perturbation for both cases of spontaneous strain which resulted in converged designs with helices in different directions. Additionally, initializing the designs with random perturbations resulted in designs that, while different, had objective values within 3% of that of the helical perturbation. Thus, we argue that this perturbation is an acceptable means to quicker convergence. It should be noted that while we have proven existence of solutions, there is no uniqueness. It is expected for problems of this nature to have multiple local minima and for the initial guess to have a sizeable effect on the converged design. However, so long as the final objective value does not differ markedly, the designs are all adequate.

3.7 Conclusions

We have investigated the optimal design of responsive structures through topology optimization. By considering a filtering scheme and SIMP interpolation, we have proven existence of optimal designs for a class of objective functions dependent on the compliances of the stimulated and unstimulated states. In particular, we have considered the actuation work and blocking load objective. We showed that these can both be written as functions of compliances. For each of these objectives, we presented numerical results for the design of bimorph actuators on a 2D rectangular domain. The converged designs contain complex structures that would otherwise be difficult to intruitively conjure, especially for the blocking load objective. Additionally, we considered the introduction of voids for the blocking load optimal design. This resulted in a rich array of structures highly dependent on the spontaneous strain and the stiffness ratios of the passive and responsive materials. Finally, we considered the design of a 3D torsional actuator for maximum blocking torque. We investigated the design for varying stiffness and volume ratios for

two cases of transformation strain. As expected, the converged designs had responsive material distributed in helices at the outer edges of the domain, with the direction dependent on the transformation strain.

We now discuss further directions that could extend this work. Here, we only consider linear elastic materials. As many active materials may undergo finite strains through both deformation and actuation, it may be worth investigating the design of structures under richer material models. In particular, geometric nonlinearities may lead to insightful designs. Another extension is coupling the stimulation and response. Physically, this could be realized though a number of mechanisms including magnetostriction, heat diffusion for shape memory alloys, or photo-responsive materials. The challenges would not only include the formulation and implementation for such a system, but also the choice of a suitable objective function. Additionally, in our work we considered the actuation strain to be prescribed and constant throughout the whole domain. With the recent developments in directional 3D printing in materials such as liquid crystal elastomers [23], an interesting extension might involve optimizing over the responsive materials spatially varying direction as well.

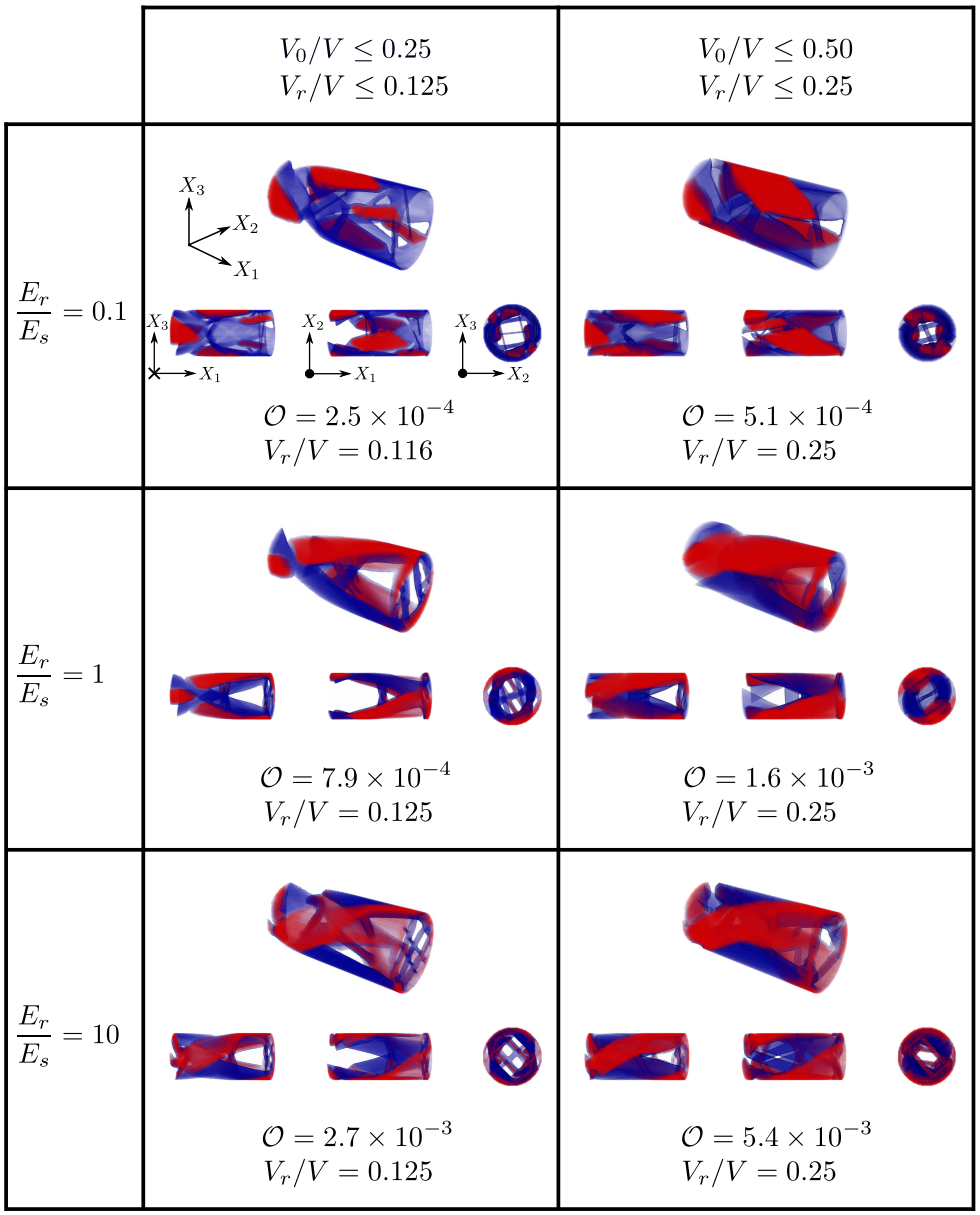

Figure 3.6: Converged designs for maximum blocking torque on the cylindrical domain for the transversly isotropic transformation strain $\varepsilon^*(1) = 0.1e_1 \otimes e_1 - 0.05e_2 \otimes e_2 - 0.05e_3 \otimes e_3$. The red is the responsive material and the blue passive. Designs are shown for varying moduli ratios and amount of total allowed material. The ratio of responsive material to passive material was constrained to $V_r/V_0 \leq 0.5$ for all cases. That is, the left column is constrained to $V_r/V \leq 0.125$ and the right to $V_r/V \leq 0.25$. Normalized blocking torque values and converged responsive material volume ratios are shown. In all cases, the designs converged to $V_0/V = 0.5$.

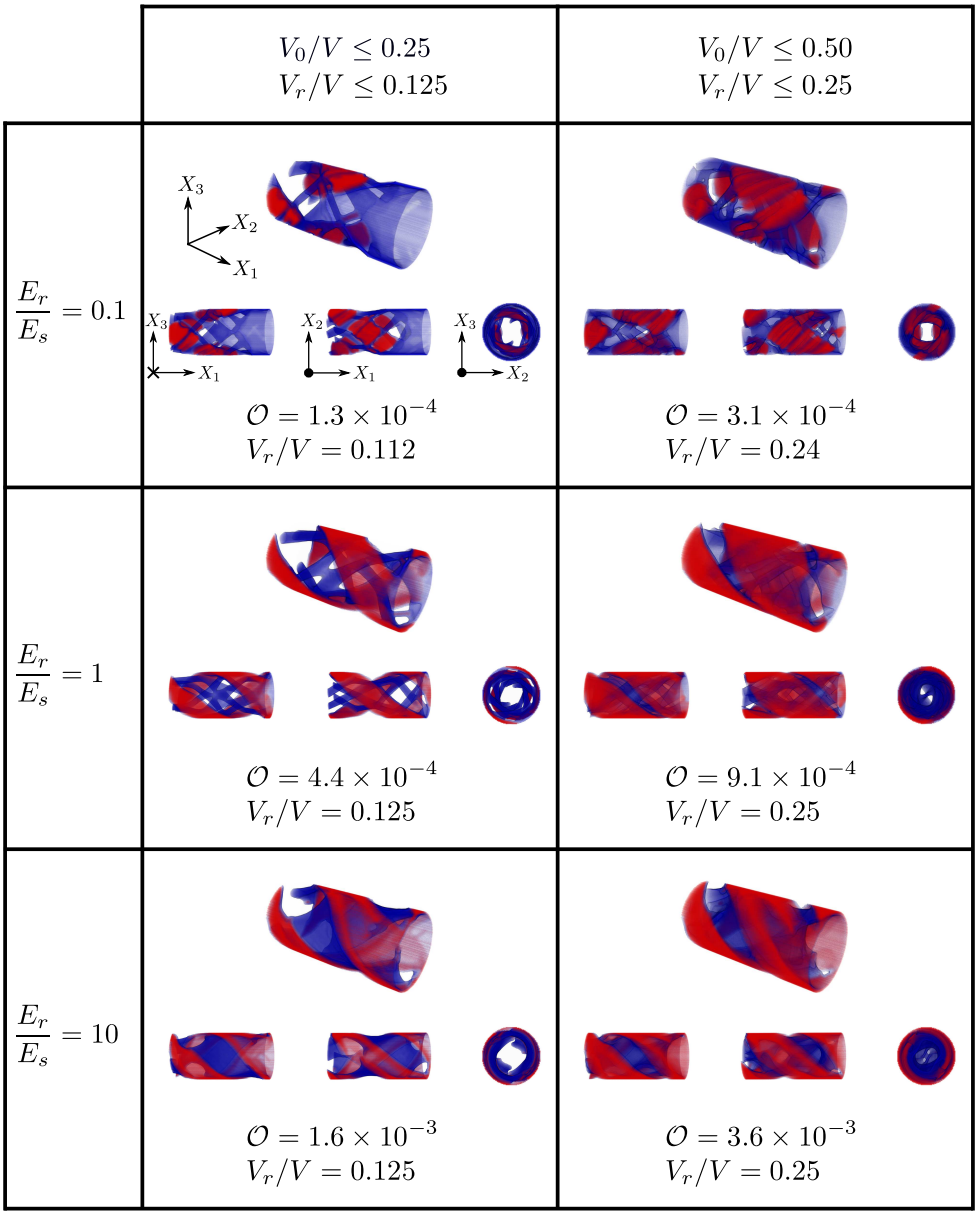

Figure 3.7: Converged designs for maximum blocking torque on the cylindrical domain for the volumetric transformation strain $\varepsilon^*(1) = -0.033\ I_{3\times3}$. The red is the responsive material and the blue passive. Designs are shown for varying moduli ratios and amount of total allowed material. The ratio of responsive material to passive material was constrained to $V_r/V_0 \leq 0.5$ for all cases. That is, the left column is constrained to $V_r/V \leq 0.125$ and the right to $V_r/V \leq 0.25$. Normalized blocking torque values and converged responsive material volume ratios are shown. In all cases, the designs converged to $V_0/V = 0.5$.

Acknowledgement We are grateful for the financial support of the U.S. National Science Foundation through "Collaborative Research: Optimal Design of Responsive Materials and Structures" (DMS:2009289 at Caltech and DMS:2009303 at LSU and McMaster University). Part of this work was performed while B.B. was the A.K. & Shirley Barton Professor of Mathematics at Louisiana State University (USA).

Conflict of Interest The authors have no financial or personal relationship with a third party whose interests could be positively or negatively influenced by the article's content.

Replication of Results The authors are willing to share the code on request. The data for the figures are available through GitHub (https://github.com/akers049/responsive_structure_data).

BIBLIOGRAPHY

[1] G. Allaire. *Shape optimization by the homogenization method*. Springer-Verlag, New York, 2002.

[2] G. Allaire and S. Aubry. On optimal microstructures for a plane shape optimization problem. *Structural optimization*, 17:86–94, 1999.

[3] G. Allaire and B. Bogosel. Optimizing supports for additive manufacturing. *Structural and Multidisciplinary Optimization*, 58(6):2493–2515, Oct 2018.

[4] G. Allaire, É. Bonnetier, G. Francfort, and F. Jouve. Shape optimization by the homogenization method. *Numerische Mathematik*, 76:27–68, 1997.

[5] G. Allaire, C. Dapogny, R. Estevez, A. Faure, and G. Michailidis. Structural optimization under overhang constraints imposed by additive manufacturing technologies. *Journal of Computational Physics*, 351:295–328, Dec 2017.

[6] G. Allaire, C. Dapogny, A. Faure, and G. Michailidis. Shape optimization of a layer by layer mechanical constraint for additive manufacturing. *Comptes Rendus Mathematique*, 355(6):699–717, Jun 2017.

[7] G. Allaire, F. Jouve, and G. Michailidis. *Variational Analysis and Aerospace Engineering*, volume 116 of *Springer Optimization and Its Applications book series*, chapter Molding Direction Constraints in Structural Optimization via a Level-Set Method, pages 1–39. Springer International Publishing, 2016.

[8] L. Ambrosio and G. Buttazzo. An optimal design problem with perimeter penalization. *Calculus of Variations and Partial Differential Equations*, 1:55–69, 1993.

[9] C. P. Ambulo, J. J. Burroughs, J. M. Boothby, H. Kim, M. R. Shankar, and T. H. Ware. Four-dimensional Printing of Liquid Crystal Elastomers. *ACS Applied Material Interfaces*, 9:37332–37339, 2017.

[10] W. Bangerth, R. Hartmann, and G. Kanschat. deal.II – a general purpose object oriented finite element library. *ACM Trans. Math. Softw.*, 33(4):24/1–24/27, 2007.

[11] M. Bendsøe and O. Sigmund. Material interpolation schemes in topology optimization. *Archive of Applied Mechanics*, 69:635–654, 1999.

[12] M. Bendsøe and O. Sigmund. *Topology Optimization: Theory, Methods and Applications*. Springer, 2nd edition, 2003.

[13] K. Bhattacharya. *Microstructure of martensite: How it forms and how it gives rise to the shape-memory effect*. Oxford University Press, 2003.

[14] B. Bourdin. Filters in topology optimization. *International Journal of Numerical Methods in Engineering*, 50:2143–2158, 2001.

[15] B. Bourdin and A. Chambolle. Design-dependent loads in topology optimization. *ESAIM: Control, Optimisation and Calculus of Variations*, 9:19–48, 2003.

[16] B. Bourdin and R. V. Kohn. Optimization of structural topology in the high-porosity regime. *Journal of Mechanics and Physics of Solids*, 56:1043–1064, 2008.

[17] P. Cesana and A. De Simone. Quasiconvex envelopes of energies for nematic elastomers in the small strain regime and applications. *Journal of the Mechanics and Physics of Solids*, 59:787–803, 2011.

[18] A. Cherkaev. *Variational methods for structural optimization*. Springer-Verlag, New York, 2000.

[19] M. Elahinia, N. S. Moghaddam, M. T. Andani, A. Amerinatanzi, B. A. Bimber, and R. F. Hamilton. Fabrication of NiTi through additive manufacturing: A review. *Progress in Materials Science*, 83:630–663, 2016.

[20] G. A. Francfort and F. Murat. Homogenization and optimal bounds in linear elasticity. *Archive for Rational Mechanics and Analysis*, 94:307–334, 1986.

[21] P. Geoffroy-Donders, G. Allaire, G. Michailidis, and O. Pantz. Coupled optimization of macroscopic structures and lattice infill. *International Journal for Numerical Methods in Engineering*, 61:2253–2269, 2020.

[22] R. Haber, C. Jog, and M. Bendsøe. A new approach to variable-topology shape design using a constraint on the perimeter. *Structural optimization*, 11:1–12, 1996.

[23] A. Kotikian, R. L. Truby, J. W. Boley, T. J. White, and J. A. Lewis. 3D Printing of Liquid Crystal Elastomeric Actuators with Spatially Programed Nematic Order. *Advanced Materials*, 30, 2018.

[24] B. S. Lazarov and O. Sigmund. Filters in topology optimization based on Helmholtz-type differential equations. *International Journal for Numerical Methods in Engineering*, 86(6):765–781, 2011.

[25] G. W. Milton. *Homogenization and Effective Moduli of Materials and Media*, volume 1 of *The IMA volumes in mathematics and its applications*, chapter Modelling the Properties of Composite by Laminates, pages 150–174. Springer-Verlag, 1986.

[26] G. W. Milton. *The Theory of Composite*. Cambridge University Press, 2002.

[27] M. Nematollahi, G. Toker, S. E. Saghaian, J. Salazar, M. Mahtabi, O. Benafan, H. Karaca, and M. Elahinia. Additive Manufacturing of Ni-Rich NiTiHf20: Manufacturability, Composition, Density, and Transformation Behavior. *Shape memory and superelasticity*, 5:113–124, 2019.

[28] J. Panetta, Q. Zhou, L. Malomo, N. Pietroni, P. Cignoni, and D. Zorin. Elastic Textures for Additive Fabrication. *ACM Transactions on Graphics*, 34, 2015.

[29] S. Park and J. Yoo. Structural optimization of a multi-physics problem considering thermal and magnetic effects. *IEEE Transactions on Magnetics*, 48(11):3883–3886, 2012.

[30] B. T. Phillips, K. P. Becker, S. Kuruyama, K. C. Galloway, G. Whittredge, D. M. Vogt, B. T. Clark, M. H. Rosen, V. A. Pieribone, D. F. Gruber, and R. J. Wood. A dexterous, glove-based teleoperable low-power soft robotic arm for delicate deep-sea biological exploration. *Scientific Reports*, 8:14779, 2018.

[31] X. Qian. Undercut and overhang angle control in topology optimization: A density gradient based integral approach. *International Journal for Numerical Methods in Engineering*, 111(3):247–272, Jan 2017.

[32] H. Rodrigue, W. Wei, B. Bhandari, and S.-H. Ahn. Fabrication of wrist-like SMA-based actuator by double smart soft composite casting. *Smart Materials and Structures*, 24:125003, 2015.

[33] H. Rodrigues and P. Fernandes. A material based model for topology optimization of thermoelastic structures. *International Journal for Numerical Methods in Engineering*, 38(12):1951–1965, 1995.

[34] T. Rosental and S. Magdassi. A New Approach to 3D Printing Dense Ceramics by Ceramic Precursor Binders. *Advanced Engineering Materials*, 21, 2019.

[35] D. Ruiz and O. Sigmund. Optimal design of robust piezoelectric micro-grippers undergoing large displacements. *Structural and Multidisciplinary Optimization*, 57(1):71–82, Jan. 2018.

[36] C. Schumacher, B. Bickel, J. Rys, S. Marschner, C. Daraio, and M. Gross. Microstructures to control elasticity in 3D printing. *ACM Transactions on Graphics*, 34:136:1–136:13, 2015.

[37] O. Sigmund. On the design of compliant mechanisms using topology optimization. *Mechanics of Structures and Machines*, 25:495–526, 1997.

[38] O. Sigmund. Systematic design of microactuators using topology optimization. In V. K. Varadan, P. J. McWhorter, R. A. Singer, and M. J. Vellekoop, editors, *Smart Structures and Materials 1998: Smart Electronics and MEMS*, volume 3328, pages 23 – 31. International Society for Optics and Photonics, SPIE, 1998.

[39] O. Sigmund. Design of multiphysics actuators using topology optimization - part i: One-material structures. *Computer Methods in Applied Mechanics and Engineering*, 190(49):6577–6604, 2001.

[40] O. Sigmund. Design of multiphysics actuators using topology optimization - part ii: Two-material structures. *Computer Methods in Applied Mechanics and Engineering*, 190(49):6605–6627, 2001.

[41] K. Svanberg. The method of moving asymptotes—a new method for structural optimization. *International Journal for Numerical Methods in Engineering*, 24(2):359–373, feb 1987.

[42] M. Tabrizi, T. H. Ware, and M. R. Shankar. Voxelated Molecular Patterning in Three-Dimensional Freeforms. *ACS Applied Materials & Interfaces*, In press:1–10, 2019.

[43] Y. Wang and Z. Kang. Structural shape and topology optimization of cast parts using level set method. *International Journal for Numerical Methods in Engineering*, 111(13):1252–1273, Jan 2017.

[44] G. H. Yoon. Topological layout design of electro-fluid-thermal-compliant actuator. *Computer Methods in Applied Mechanics and Engineering*, 209-212:28–44, 2012.

[45] P. A. York and R. J. Wood. Nitinol living hinges for millimeter-sized robots and medical devices. *International Conference on Robotics and Automation*, pages 889–893, 2019.

APPENDIX TO CHAPTER 3

3.A Proof of Lemma 3.3.2

Here, we provide the proof of Lemma 3.3.2.

Proof. We will first show by compactness that there exists a $u^\infty \in \mathcal{U}$ such that $u_k \rightharpoonup u^\infty$ in $W^{1,2}(\Omega)$. Then, we will show that we must have $u^\infty = \bar{u}$.

Since u_k is the equillibrium solution corresponding to ϕ_k for some fixed S, it satisfies

$$u_k = \arg\min_{u \in \mathcal{U}} \ \mathcal{E}_f(\phi_k, u, S), \tag{3.65}$$

and for any $\tilde{u} \in \mathcal{U}$, we have

$$\mathcal{E}_f(\phi_k, u_k, S) \leq \mathcal{E}_f(\phi_k, \tilde{u}, S). \tag{3.66}$$

Furthermore,

$$\mathcal{E}_f(\phi_k, \tilde{u}, S) \leq \int_\Omega \frac{1}{2} \left[\mathbb{C}_s \varepsilon(\tilde{u}) \cdot \varepsilon(\tilde{u}) + \mathbb{C}_r(S)(\varepsilon(\tilde{u}) - \varepsilon^*(S)) \cdot (\varepsilon(\tilde{u}) - \varepsilon^*(S))\right] \, dx - \int_{\partial_f \Omega} f \cdot \tilde{u} \, ds = M \tag{3.67}$$

where M is some constant, independent of k. So,

$$\mathcal{E}_f(\phi_k, u_k, S) \leq M. \tag{3.68}$$

Now, expanding the energy functional

$$\begin{aligned} \mathcal{E}_f(\phi_k, u_k, S) = \int_\Omega \frac{1}{2} \Big[& (1 - (F * \phi_k)^p) \mathbb{C}_s \varepsilon(u_k) \cdot \varepsilon(u_k) \\ & + (F * \phi_k)^p \mathbb{C}_r(S) \varepsilon(u_k) \cdot \varepsilon(u_k) \\ & + (F * \phi_k)^p \mathbb{C}_r(S) \varepsilon^*(S) \cdot \varepsilon^*(S) \\ & - 2(F * \phi_k)^p \mathbb{C}_r(S) \varepsilon^*(S) \cdot \varepsilon(u_k) \Big] \, dx \\ - \int_{\partial_f \Omega} f \cdot u_k \, ds, & \end{aligned} \tag{3.69}$$

and using the ellipticity from Remark 1

$$\begin{aligned}
m\|u_k\|^2_{W^{1,2}(\Omega)} - \left|\int_\Omega (F*\phi_k)^p \mathbb{C}_r(S)\varepsilon^*(S)\cdot\varepsilon(u_k)\ dx\right| - \int_{\partial_f\Omega} f\cdot u_k\ ds &\le \mathcal{E}_f(\phi_k,u_k,S),\\
m\|u_k\|^2_{W^{1,2}(\Omega)} - \int_\Omega (F*\phi_k)^p\,|\mathbb{C}_r(S)\varepsilon^*(S)\cdot\varepsilon(u_k)|\ dx - \int_{\partial_f\Omega} f\cdot u_k\ ds &\le \mathcal{E}_f(\phi_k,u_k,S),\\
m\|u_k\|^2_{W^{1,2}(\Omega)} - \int_\Omega (F*1)^p\,|\mathbb{C}_r(S)\varepsilon^*(S)\cdot\varepsilon(u_k)|\ dx - \int_{\partial_f\Omega} f\cdot u_k\ ds &\le \mathcal{E}_f(\phi_k,u_k,S),\\
m\|u_k\|^2_{W^{1,2}(\Omega)} - \int_\Omega |\mathbb{C}_r(S)\varepsilon^*(S)\cdot\varepsilon(u_k)|\ dx - \int_{\partial_f\Omega} f\cdot u_k\ ds &\le \mathcal{E}(\phi_k,u_k,S),\\
m\|u_k\|^2_{W^{1,2}(\Omega)} - \|\mathbb{C}_r(S)\varepsilon^*(S)\|_{L^2(\Omega)}\|\varepsilon(u_k)\|_{L^2(\Omega)} - \int_{\partial_f\Omega} f\cdot u_k\ ds &\le \mathcal{E}_f(\phi_k,u_k,S),\\
m\|u_k\|^2_{W^{1,2}(\Omega)} - c\|u_k\|_{W^{1,2}(\Omega)} - \int_{\partial_f\Omega} f\cdot u_k\ ds &\le \mathcal{E}_f(\phi_k,u_k,S)
\end{aligned} \tag{3.70}$$

for some constants $m, c > 0$, independent of k. Additionally,

$$\begin{aligned}
m\|u_k\|^2_{W^{1,2}(\Omega)} - c\|u_k\|_{W^{1,2}(\Omega)} - \left|\int_{\partial_f\Omega} f\cdot u_k\ ds\right| &\le \mathcal{E}_f(\phi_k,u_k,S),\\
m\|u_k\|^2_{W^{1,2}(\Omega)} - c\|u_k\|_{W^{1,2}(\Omega)} - \|f\|_{L^2(\partial_f\Omega)}\|u_k\|_{L^2(\partial_f\Omega)} &\le \mathcal{E}(\phi_k,u_k,S),\\
m\|u_k\|^2_{W^{1,2}(\Omega)} - c\|u_k\|_{W^{1,2}(\Omega)} - \|f\|_{L^2(\partial_f\Omega)}\|u_k\|_{L^2(\partial\Omega)} &\le \mathcal{E}_f(\phi_k,u_k,S),\\
m\|u_k\|^2_{W^{1,2}(\Omega)} - c\|u_k\|_{W^{1,2}(\Omega)} - a\|u_k\|_{W^{1,2}(\Omega)} &\le \mathcal{E}_f(\phi_k,u_k,S),
\end{aligned} \tag{3.71}$$

for some constant $a > 0$. Then,

$$m\|u_k\|^2_{W^{1,2}(\Omega)} - b\|u_k\|_{W^{1,2}(\Omega)} \le M \implies \|u_k\|_{W^{1,2}(\Omega)} \le d, \tag{3.72}$$

for some constant $b > 0$, where $d > 0$ is a constant independent of k. Thus, u_k is a bounded sequence in $W^{1,2}(\Omega)$, and there exists a $u^\infty \in \mathcal{U}$ such that

$$u_k \rightharpoonup u^\infty \text{ in } W^{1,2}(\Omega) \text{ when } k \to +\infty, \tag{3.73}$$

up to a subsequence. Next, consider $\bar{u} \in \mathcal{U}$ such that

$$\bar{u} = \arg\min_{u\in\mathcal{U}} \mathcal{E}_f(\bar{\phi}, u, S). \tag{3.74}$$

Then

$$\mathcal{E}_f(\bar{\phi},\bar{u},S) \le \mathcal{E}_f(\bar{\phi},u^\infty,S). \tag{3.75}$$

Similarly,

$$\begin{aligned}
\mathcal{E}_f(\phi_k,u_k,S) \le \mathcal{E}_f(\phi_k,\bar{u},S) = \mathcal{E}_f(\phi_k,\bar{u},S) - \mathcal{E}_f(\bar{\phi},\bar{u},S) + \mathcal{E}_f(\bar{\phi},\bar{u},S)\\
- \mathcal{E}_f(\bar{\phi},u_k,S) + \mathcal{E}_f(\bar{\phi},u_k,S),
\end{aligned} \tag{3.76}$$

or

$$\begin{aligned}\mathcal{E}_f(\bar{\phi}, u_k, S) \leq & \mathcal{E}_f(\bar{\phi}, \bar{u}, S) + \mathcal{E}_f(\phi_k, \bar{u}, S) \\ & - \mathcal{E}_f(\bar{\phi}, \bar{u}, S) + \mathcal{E}_f(\bar{\phi}, u_k, S) - \mathcal{E}_f(\phi_k, u_k, S).\end{aligned} \tag{3.77}$$

Then taking limits, and using the strong convergence of the convolution gives

$$\lim_{k\to\infty} \mathcal{E}_f(\bar{\phi}, u_k, S) \leq \mathcal{E}_f(\bar{\phi}, \bar{u}, S). \tag{3.78}$$

The convexity of the energy integrand in ∇u and u for a given ϕ and S gives lower semi-continuity of our energy function

$$\mathcal{E}_f(\bar{\phi}, u^\infty, S) \leq \lim_{k\to\infty} \mathcal{E}_f(\bar{\phi}, u_k, S), \tag{3.79}$$

so

$$\mathcal{E}_f(\bar{\phi}, u^\infty, S) \leq \mathcal{E}_f(\bar{\phi}, \bar{u}, S). \tag{3.80}$$

Then from (3.75),

$$\mathcal{E}_f(\bar{\phi}, u^\infty, S) = \mathcal{E}_f(\bar{\phi}, \bar{u}, S). \tag{3.81}$$

From the uniqueness of the minimizer of $\mathcal{E}_f(\bar{\phi}, \cdot, S)$ we have

$$u^\infty = \bar{u}. \tag{3.82}$$

Then, as desired,

$$u_k \rightharpoonup \bar{u} \text{ in } W^{1,2}(\Omega) \text{ when } k \to +\infty. \tag{3.83}$$

□

3.B Workpiece Objective as Force in Spring

Here we show the workpiece objective is equivalent to maximizing the load of a point spring. This is equivalent to the objective used by Sigmund in an earlier work to study thermal actuators [38]. However, we include the derivation here for completeness. Consider a linear spring in direction $\hat{n}$ of spring constant $\kappa > 0$ connected to the boundary of the domain at some point of interest $x_0 \in \partial_f\Omega$. The aim is to maximize the load carried by this spring upon actuation. Thus, we look to maximize the load in the spring:

$$\sup\{f_0 : f_0 = -\kappa u(x_0) \cdot \hat{n}, \Phi \in \mathcal{D}\} \tag{3.84}$$

where u is the equilibrium solution corresponding to $S = 1$ and $f = f_0\delta(x - x_0)\hat{n}$. Assuming homogeneous Dirichlet conditions $u_0 = 0$ on $\partial_u\Omega$, it is easy to see using the linearity of the Euler-Lagrange equations

$$u = v + u_{S=0, f_0\hat{n}} \tag{3.85}$$

where $u_{S=0,f_0\hat{n}}$ minimizes the elastic energy (3.4) with $S = 0$ and $f = f_0\delta(x - x_0)\hat{n}$. Invoking linearity again gives $u_{S=0,f_0\hat{n}} = f_0 u_{S=0,\hat{n}}$. The displacement can then be written as

$$u = v + f_0 u_{S=0,\hat{n}}. \tag{3.86}$$

Evaluating at $x = x_0$, taking an inner product with $\hat{n}$, and using the constraint that $f_0 = -\kappa u(x_0) \cdot \hat{n}$ gives

$$-\frac{f_0}{\kappa} = v(x_0) \cdot \hat{n} + f_0 u_{S=0,\hat{n}}(x_0) \cdot \hat{n}. \tag{3.87}$$

Rearranging gives

$$f_0 = \frac{-\kappa v(x_0) \cdot \hat{n}}{\kappa u_{S=0,\hat{n}}(x_0) \cdot \hat{n} + 1} = \frac{-\kappa v(x_0) \cdot \hat{n} - \kappa u_{S=0,\hat{n}}(x_0) \cdot \hat{n} - 1}{\kappa u_{S=0,\hat{n}}(x_0) \cdot \hat{n} + 1} - 1 \tag{3.88}$$

or

$$f_0 = \frac{-\kappa u_{S=1,\hat{n}}(x_0) \cdot \hat{n} - 1}{\kappa u_{S=0,\hat{n}}(x_0) \cdot \hat{n} + 1} - 1. \tag{3.89}$$

We recognize $u_{S=0,\hat{n}}(x_0) \cdot \hat{n}$ and $u_{S=1,\hat{n}}(x_0) \cdot \hat{n}$ as the unactuated and actuated compliances under loading $f = \delta(x - x_0)\hat{n}$. Thus, the workpiece objective can then be written as a function of compliancies,

$$\inf_{\Phi \in \mathcal{D}} \mathcal{O}(\Phi) = \frac{\kappa \mathcal{C}_{\hat{n}}(\Phi, 1) + 1}{\kappa \mathcal{C}_{\hat{n}}(\Phi, 0) + 1} \tag{3.90}$$

Chapter 4

OPTIMAL DESIGN OF 3D PRINTED SOFT RESPONSIVE ACTUATORS

Abstract

With recent advances in both responsive material synthesis and fabrication techniques, it is now possible to construct integrated multifunctional structures composed of both passive and active materials. Additionally, developments in 3D printing of anisotropic materials, such as liquid crystal elastomers, have facilitated the realization of structures with arbitrary morphology and tailored material orientation. However, the design of these structures is complicated by trade-offs between properties such as flexibility and stiffness, especially when finite strains are considered. Additionally, the manufacturing process constrains the design as extrusion-based 3D printing aligns nematic directors along the print path. We have developed an efficient and robust numerical method to optimally design simultaneously structural layout and material orientation for manufacturable structures, while also yielding the print path. We use this formulation to investigate a variety of lifting actuators. Then, we demonstrate the method by producing physical realizations of the designs through advanced 3D printing processes.

4.1 Introduction

Wearable technology, biomedical devices, and soft robotics applications require flexible actuators that generate large forces in compact form factors. While pneumatic [26, 28] and piezoelectric [17, 22] actuators remain popular, they suffer from reliance on external pumps, limited displacements, or inflexibility. Recent advances in material synthesis technologies have allowed responsive materials – ones that deform upon stimulus application – to shift towards a "material as the machine" approach [10]. Rather than using dedicated actuators at discrete joints, the material which composes the structure performs the actuation through micro-scale reconfiguration leading to macro-scopic shape change. This is observed in metallic shape memory alloys where temperature change or mechanical loading causes a solid-to-solid phase transformation [9].

Additionally, there are a wide variety of responsive polymers which may respond to other stimuli such as light [32], pH [19], or moisture [1].

Of these responsive polymers, liquid crystal elastomers (LCEs) have enormous potential. Composed of rod-like liquid crystal mesogens embedded in a polymeric matrix, these materials undergo a temperature induced phase transformation [31, 27]. At the mico-scale, these mesogens transition from a disordered to aligned state, pulling the polymeric matrix, and leading to large deformations of up to 55% contraction. This results in an unprecedented work output density reported up to 2.6 J/Kg [30], all while maintaining a soft mechanical response.

More recently, researchers have now been able to apply advanced manufacturing techniques to produce integrated structures composed of both LCEs and support material through 3D printing methods [20, 4]. This may realize structures of arbitrary material layout with tailored micro-structural orientation. However, researchers have used these and other advanced manufacturing techniques to predominately designed shape changing structures which only utilize free recovery [29, 21]. That is, structures that are not designed for load carrying capacity, and therefore do not take full advantage of these materials' high work output density. But designing these structures for load bearing applications is difficult. When 3D printing these materials, the extrusion through the nozzle aligns the nematic directors along the print path [20, 4]. These manufacturing constraints along with the large deformation actuation mechanics makes designing integrated responsive actuators, which balance both actuation flexibility and structural stiffness, extremely challenging.

To address this difficult design problem, we borrow ideas from the field of structural optimization. Here, the design of a structure is posed as an optimization problem before being solved computationally. Thus, we may realize high-performance structures through a systematic and robust design approach. This removes the reliance on human intuition and guesswork, which may break down when applied to complicated scenarios. While these ideas were originally developed to design minimum compliance structure for small deformations [8, 25, 7], they have since been applied to a wide range of actuating systems such as micro-electromechanical systems [23], magneto-responsive structures [33], electro-mechanical systems [3], and small-deformation responsive structures [2]. However, these methods must be heavily extended to design

integrated LCE actuators which remain compatible with 3D printing methods.

To this end, we formulate a rigorous optimal design formulation which accounts for microstructural evolution leading to actuation, finite deformation mechanics, and manufacturing constraints to design 3D printed multi-material responsive actuators composed of both LCE and support polymer. We demonstrate the methodology by considering a variety of soft responsive lifting actuators. Finally, we use the optimized designs and recovered print paths to realize physical 3D printed LCE actuators.

To develop the formulation, we start from simplified linearized kinematics before building the theory to include finite deformation and manufacturing constraints. We begin in Section 4.2 by considering design of both structure and material orientation in the linearized setting for actuators composed of anisotropic responsive materials. Then, in Section 4.3, we extend the theory to handle finite deformations and the associated micostructural evolution using a classical model for LCEs. Here, particular attention is put towards regularization, as there exist fundamental distinctions between the small strain and finite deformation settings. In Section 4.4, we study lifting actuators in 2D and 3D using the developed formulations. We notice that these structures are infeasible to manufacture. The micromechanics of the 3D printing process for LCEs creates a coupling between the design and the manufacturing pathway. We adapt the formulation to include manufacturing constraints in Section 4.5, and revisit the lifting actuator. Additionally, we present physical realizations of these structures through advanced 3D printing processes. We conclude in Section 4.6 by summarizing our finding and discuss directions moving forward.

4.2 Design for Small Strains

To develop a fundamental understanding of the design problem, we first consider the simplified case of linearized kinematics. We formulate the design of both structure and material orientation for a transversely isotropic actuation strain. We investigate mathematical regularization by applying filtering methods to the material densities. However, we still must address the possible fine structure formation in the material orientations. By exploiting the linearity of the system and considering a particular class of objective functions, we prove well posed-ness of the design problem without any further regularization to the material orientation.

4.2.1 Transversely Isotropic Responsive Materials

As in [2], we consider a linear elastic responsive material which may change shape or stiffness in response to a stimulus with energy density

$$W(\varepsilon, a, S) := \frac{1}{2}(\varepsilon(u) - \varepsilon^*(S,a)) \cdot \mathbb{C}(S)(\varepsilon(u) - \varepsilon^*(S,a)), \tag{4.1}$$

where $\varepsilon(u) = (\nabla u + \nabla u^T)/2$ is the linearized strain, $S \in [0,1]$ the stimulus (assumed here to be a scalar), $\varepsilon^*(S,a)$ is the stimulus-dependent actuation or spontaneous strain, and $\mathbb{C}(S)$ is the possibly stimulus-dependent elastic modulus. In the linearized setting, the spontaneous strain takes the form [15]

$$\varepsilon^*(S,a) = \frac{\varepsilon_0(S)}{n-1}\left[I_{n\times n} - n(a \otimes a)\right]. \tag{4.2}$$

Here, the spontaneous strain is a volume-preserving and transversely isotropic about axis $a \in \mathbb{R}^n$ with magnitude ε_0, where $n = 2, 3$ is the spatial dimension. In 3D this corresponds to a contraction along a by ε_0 and extension along directions perpendicular to a by $\varepsilon_0/2$. This is inspired by contraction along directors in active materials such as LCE's when transforming from a nematic to isotropic state. We assume here that $\varepsilon_0(0) = 0$.

4.2.2 Optimization

Consider an integrated functional structure occupying a bounded region $\Omega \subset \mathbb{R}^n$ of volume V, consisting of a structural material and a responsive material. Let $\chi_s, \chi_r : \Omega \mapsto \{0,1\}$ be the characteristic functions of the regions that the structural and responsive materials occupy. We allow for a spatially varying isotropy axis of the responsive material. Let $\mathcal{S}^{n-1}$ be the unit sphere on $\mathbb{R}^n$,

$$\mathcal{S}^{n-1} = \{v \in \mathbb{R}^n : \|v\|_{l^2} = 1\}. \tag{4.3}$$

$a : \Omega_{\chi_r=1} \mapsto \mathcal{S}^{n-1}$ is the extension axis of the responsive material as described in (4.2). $\Phi := (\chi_s, \chi_r, a)$ then describes the design. In this section, we first assume that there are no voids, i.e., $\chi_s + \chi_r = 1$.

Subject to a traction $t \in L^2(\partial_f\Omega)$ on $\partial_t\Omega$ and displacement u_0 on $\partial_u\Omega$, the energy function describing this structure for a given displacement field u under stimulus $S \in [0,1]$ is

$$\begin{aligned}\mathcal{E}(\Phi, u, S) := \int_\Omega \frac{1}{2}[&\chi_s\varepsilon(u) \cdot \mathbb{C}_s\varepsilon(u) \\ &+ \chi_r(\varepsilon(u) - \varepsilon^*(S,a)) \cdot \mathbb{C}_r(S)(\varepsilon(u) - \varepsilon^*(S,a))]\, dx \\ &- \int_{\partial_t\Omega} t \cdot u \, ds,\end{aligned} \tag{4.4}$$

where $\mathbb{C}_s$ and $\mathbb{C}_r$ denote, respectively, the non-degenerate Hooke's laws of the structural and responsive materials. The compliance of a design is

$$\mathcal{C}(\Phi, S) := \int_{\partial_t \Omega} t \cdot u \, ds, \tag{4.5}$$

where u is the displacement given by the equilibrium condition

$$u = \arg\min_{u \in \mathcal{U}} \ \mathcal{E}(\Phi, u, S), \tag{4.6}$$

where

$$\mathcal{U} := \{u \in W^{1,2}(\Omega) : u = u_0 \text{ on } \partial_u \Omega\}. \tag{4.7}$$

The task is to find the design Φ that minimizes an objective function, which we assume to be dependent on the compliances of two states with different stimuli. Thus, we consider a class of optimization problems

$$\inf_{\Phi \in \mathcal{D}} \ \mathcal{O}(\Phi) := \bar{\mathcal{O}}(\mathcal{C}(\Phi, S_1), \mathcal{C}(\Phi, S_2)), \tag{4.8}$$

where $\bar{\mathcal{O}} : \mathbb{R} \times \mathbb{R} \mapsto \mathbb{R}$ is a given continuous function, amongst the set of allowable designs:

$$\mathcal{D} = \{\Phi : \chi_r + \chi_s = 1 \text{ on } \Omega, \ \int_\Omega \chi_r \ dV \leq \bar{V}_r, \ a(x) \in \mathcal{S}^{n-1} \text{ on } \Omega_{\chi_r = 1}\}. \tag{4.9}$$

Here, we have specified the allowable designs such that the materials occupy the whole domain and consider a restriction on the volume of responsive material, where $\bar{V}_r \leq V$ is the maximum allowed. The above problem is often ill-posed, suffering from the same issues as that of the standard compliance optimization. Thus, we introduce a SIMP interpolation and a filter as discussed in the previous chapter. We also relax the transformation strains and consider optimizing over this relax set. We will show well posedness of this new problem. Additionally, we will show that for a certain class of objective functions, the optimal transformation strains will be of the form (4.2).

4.2.3 Relaxation and Penalization

We relax the energy for the responsive structure through a SIMP interpolation of penalty factor $p > 1$ with the field $\phi : \Omega \mapsto [0, 1]$ describing the topology. Regions of $\phi = 0$ and $\phi = 1$ corresponding to passive and active material, respectively. We also relax the transformation strains to instead consider the convexification of the original space of transversly isotropic transformation

strains [11]. This being the space of all effective transformation strains achievable through fine mixtures. Thus, we consider the energy function

$$\begin{aligned}\mathcal{E}_f(\phi,\hat{\varepsilon}^*,u,S) :=& \\ &\int_\Omega \frac{1}{2}\Big\{(1-(f*\phi)^p)\mathbb{C}_s\varepsilon(u)\cdot\varepsilon(u) \\ &\quad + (f*\phi)^p\mathbb{C}_r(S)\left[\varepsilon(u)-\varepsilon_0(S)\hat{\varepsilon}^*\right]\cdot\left[\varepsilon(u)-\varepsilon_0(S)\hat{\varepsilon}^*\right]\Big\}\,dx \\ &- \int_{\partial_t\Omega} t\cdot u\; ds,\end{aligned} \tag{4.10}$$

where f is the filter function of characteristic length $R_f > 0$ satisfying

$$\begin{aligned} &f \in W^{1,2}(\mathbb{R}^n), \\ &\text{Supp}(f) \subset B_{R_f}, \\ &f \geq 0 \;\text{ a.e. in }\; B_{R_f}, \\ &\int_{B_{R_f}} f\; dx = 1, \end{aligned} \tag{4.11}$$

and B_{R_f} denotes the open ball of radius R_f of $\mathbb{R}^n$. We define the convolution over the bounded region Ω as

$$(f*\phi)(x) := \int_\Omega f(x-y)\phi(y)\; dy. \tag{4.12}$$

Notice that since the integral in (4.12) is over Ω, the filtered density near the boundary will not be able to take values near unity. In practice, we renormalize the convolution following the lines of [14] to avoid such boundary effects. The compliance of a design is, again,

$$\mathcal{C}(\phi,\hat{\varepsilon}^*,S) := \int_{\partial_t\Omega} t\cdot u\, ds, \tag{4.13}$$

where u is the displacement associated with the design Φ and stimulus S minimizing $\mathcal{E}_f(\phi,u,S)$. Assuming non-degenerate elastic moduli, u is the unique solution of the Euler-Lagrange equations,

$$\mathcal{Q}_f(\phi,\hat{\varepsilon}^*,u,v,S) = 0 \quad \forall\; v \in \mathcal{U}_0, \tag{4.14}$$

with

$$\begin{aligned}\mathcal{Q}_f(\phi,\hat{\varepsilon}^*,u,v,S) := \int_\Omega &\Big\{(1-(f*\phi)^p)\mathbb{C}_s\varepsilon(u)\cdot\varepsilon(v) \\ &+ (f*\phi)^p\mathbb{C}_r(S)\left[\varepsilon(u)-\varepsilon_0(S)\hat{\varepsilon}^*\right]\cdot(\varepsilon(v))\Big\}\,dx - \int_{\partial_t\Omega} t\cdot v\; ds,\end{aligned} \tag{4.15}$$

and

$$\mathcal{U}_0 := \{u \in W^{1,2}(\Omega) : u = 0 \text{ on } \partial_u\Omega\}. \tag{4.16}$$

Rather than consider the space of transversly isotropic transformation strains, we relax the problem to account for all fine mixtures of transformations. Thus, we consider

$$\inf_{\phi\in\mathcal{D}_\phi,\ \hat{\varepsilon}^*\in\mathcal{D}_\varepsilon^{QC}} \mathcal{O}(\phi,\hat{\varepsilon}^*) := \bar{\mathcal{O}}(\mathcal{C}(\phi,\hat{\varepsilon}^*,S_1),\mathcal{C}(\phi,\hat{\varepsilon}^*,S_2)), \tag{4.17}$$

where we optimize over the sets

$$\mathcal{D}_\phi := \left\{\phi :\ \phi(x)\in[0,1]\ \text{ a.e. on } \Omega, \int_\Omega \phi\ dx \le \bar{V}_r\right\}, \tag{4.18}$$

$$\begin{aligned}\mathcal{D}_\varepsilon^{QC} := \{\hat{\varepsilon}^* :\ &\hat{\varepsilon}^*(x) = [\hat{\varepsilon}^*(x)]^T,\ \mathrm{Tr}(\hat{\varepsilon}^*(x)) = 0,\\ &\text{with principle values } -1 \le \varepsilon_1,\varepsilon_2,\varepsilon_3 \le 1/2 \text{ for all } x\in\Omega\}.\end{aligned} \tag{4.19}$$

Here, we are considering a spatial dimension of $n = 3$. The following analysis is easily extended to $n = 2$.

Remark 3. *Ellipticity: From the definition of $\mathcal{D}$, the properties of the Hooke's laws* (3.5)*, and the properties of the filter, there exists a constant $m > 0$, only depending on Ω and S such that for any ϕ and $u \in \mathcal{U}$ the following holds:*

$$\begin{aligned}\int_\Omega \frac{1}{2}\left[(1-(f*\phi)^p)\mathbb{C}_s\varepsilon(u)\cdot\varepsilon(u) + (f*\phi)^p\mathbb{C}_r(S)\varepsilon(u)\cdot\varepsilon(u)\right]\ dx\\ \ge m\|u\|^2_{W^{1,2}(\Omega)}.\end{aligned} \tag{4.20}$$

We will now prove existence of structures and relaxed transformation strains that minimize a compliance dependent objective. The proof follows closely to that of Theorem 2.1 of [2]. As such, we require the following supporting lemmas. These establish weak continuity of solutions to the elasticity problem and weak continuity of the compliance.

Lemma 4.2.1 (Weak continuity of elastic solutions)**.** *Let $\{u_k\} \subset \mathcal{U}$ be the sequence of equilibrium solutions to* (4.14) *corresponding to sequence $\{\phi_k, \hat{\varepsilon}^*_k\} \subset \mathcal{D}_\phi \times \mathcal{D}_\varepsilon^{QC}$, for some fixed S. If*

$$(f*\phi_k)^p \to (f*\bar{\phi})^p \text{ uniformly on } \Omega \text{ when } k\to+\infty \tag{4.21}$$

and

$$\hat{\varepsilon}^*_k \rightharpoonup \bar{\varepsilon}^* \quad \text{in } L^2(\Omega) \text{ when } k\to+\infty, \tag{4.22}$$

then

$$u_k \rightharpoonup \bar{u} \text{ in } W^{1,2}(\Omega) \text{ when } k \to +\infty, \tag{4.23}$$

up to a subsequence, where $\bar{u} \in \mathcal{U}$ *is the equilibrium configuration corresponding to* $\bar{\phi} \in \mathcal{D}_\phi$ *and* $\bar{\varepsilon}^* \in \mathcal{D}_\varepsilon^{QC}$

$$\bar{u} = \arg\min_{u \in \mathcal{U}} \ \mathcal{E}_f(\bar{\phi}, \bar{\varepsilon}^*, u, S). \tag{4.24}$$

Proof. It is estabilished in [2] that u_k is uniformly bounded in $W^{1,2}(\Omega)$, and thus there exists a $\bar{u} \in \mathcal{U}$ such that

$$u_k \rightharpoonup \bar{u} \text{ in } W^{1,2}(\Omega) \text{ when } k \to +\infty, \tag{4.25}$$

up to a subsequence. Then,

$$\begin{aligned}(1-(f*\phi_k)^p)\mathbb{C}_s\varepsilon(u_k) + (f*\phi_k)^p\mathbb{C}_r(S)\left[\varepsilon(u_k) - \varepsilon_0(S)\hat{\varepsilon}_k^*\right] \rightharpoonup \\ (1-(f*\bar{\phi})^p)\mathbb{C}_s\varepsilon(\bar{u}) + (f*\bar{\phi})^p\mathbb{C}_r(S)\left[\varepsilon(\bar{u}) - \varepsilon_0(S)\bar{\varepsilon}^*\right] \\ \text{in } L^2(\Omega) \text{ when } k \to +\infty.\end{aligned} \tag{4.26}$$

Then, from (4.14), $\bar{u}$ is the unique equilibrium solutions corresponding to $\bar{\phi}$ and $\bar{\varepsilon}^*$,

$$\bar{u} = \arg\min_{u \in \mathcal{U}} \ \mathcal{E}_f(\bar{\phi}, \bar{\varepsilon}^*, u, S). \tag{4.27}$$

□

Lemma 4.2.2 (Continuity of the compliance)**.** *Let* $\{u_k\} \subset \mathcal{U}$ *be the sequence of equilibrium solutions corresponding to sequence* $\{\phi_k\} \subset \mathcal{D}_\phi$, $\{\hat{\varepsilon}_k^*\} \subset \mathcal{D}_\varepsilon^{QC}$ *for some fixed* S*. If*

$$u_k \rightharpoonup \bar{u} \text{ in } W^{1,2}(\Omega) \text{ when } k \to +\infty, \tag{4.28}$$

where $\bar{u} \in \mathcal{U}$ *is the equilibrium configuration corresponding to* $\bar{\phi} \in \mathcal{D}_\phi$ *and* $\bar{\varepsilon}^* \in \mathcal{D}_\varepsilon^{QC}$ *then*

$$\lim_{k \to \infty} \ \mathcal{C}(\phi_k, \hat{\varepsilon}_k^*, S) = \mathcal{C}(\bar{\phi}, \bar{\varepsilon}^* S). \tag{4.29}$$

Proof. This is clear from the definition of the compliance and the weak convergence of $\{u_k\}$. □

We are now ready to prove existence of solutions for relaxed transformation strains.

Theorem 4.2.3 (Existence for relaxed transformation strains)**.** *Recall the definition of the compliances from* (4.13)*, and set*

$$\mathcal{O}(\phi, \hat{\varepsilon}^*) := \bar{\mathcal{O}}(\mathcal{C}(\phi, \hat{\varepsilon}^*, S_1), \mathcal{C}(\phi, \hat{\varepsilon}^*, S_2)), \tag{4.30}$$

where $\bar{\mathcal{O}}$ *is bounded below and continuous. There exists* $\bar{\phi} \in \mathcal{D}_\phi$ *and* $\bar{\varepsilon}^* \in \mathcal{D}_\varepsilon^{QC}$ *such that,*

$$\mathcal{O}(\bar{\phi}, \bar{\varepsilon}^*) = \inf_{\phi \in \mathcal{D}_\phi,\ \hat{\varepsilon}^* \in \mathcal{D}_\varepsilon^{QC}} \mathcal{O}(\phi, \hat{\varepsilon}^*). \tag{4.31}$$

Proof. Let $\{\phi_k, \hat{\varepsilon}_k^*\} \subset \mathcal{D}_\phi \times \mathcal{D}_\varepsilon^{QC}$ be a minimizing sequence for (4.31). $\mathcal{D}_\phi$ implies that ϕ_k is uniformly bounded in $L^2(\Omega)$ and thus there exists $\bar{\phi} \in \mathcal{D}_\phi$ such that

$$\phi_k \rightharpoonup \bar{\phi} \ \text{ in } L^2(\Omega) \text{ when } k \to +\infty, \tag{4.32}$$

up to a sub-sequence. Because $F \in L^2(\mathbb{R}^n)$,

$$(f * \bar{\phi})(x) - \lim_{k\to\infty} (f * \phi_k)(x) = \lim_{k\to\infty} \int_\Omega f(x-y) \left(\bar{\phi}(y) - \phi_k(y)\right)\, dy = 0. \tag{4.33}$$

Since this holds for all $x \in \Omega$,

$$f * \phi_k \to f * \bar{\phi} \text{ uniformly on } \Omega \text{ when } k \to +\infty. \tag{4.34}$$

Because $(f * \phi)(x)$ is bounded for all $\phi \in \mathcal{D}_\phi$,

$$(f * \phi_k)^p \to (f * \bar{\phi})^p \text{ uniformly on } \Omega \text{ when } k \to +\infty. \tag{4.35}$$

Additionally, $\hat{\varepsilon}_k^*$ is uniformly bounded in $L^2(\Omega)$. Because $\mathcal{D}_\varepsilon^{QC}$ is sequentially compact, there exists a $\bar{\varepsilon}^* \in \mathcal{D}_\varepsilon^{QC}$ such that

$$\hat{\varepsilon}_k^* \rightharpoonup \bar{\varepsilon}^* \ \text{ in } L^2(\Omega) \text{ when } k \to +\infty, \tag{4.36}$$

up to a sub-sequence. Let u_{1k}, $u_{2k} \in \mathcal{U}$ be the equilibrium solutions to (4.14) corresponding to ϕ_k, $\hat{\varepsilon}_k^*$ for $S = S_1$ and $S = S_2$, respectively:

$$u_{1k} = \arg\min_{u\in\mathcal{U}} \ \mathcal{E}_f(\phi_k, \hat{\varepsilon}_k^*, u, S_1), \qquad u_{2k} = \arg\min_{u\in\mathcal{U}} \ \mathcal{E}_f(\phi_k, \hat{\varepsilon}_k^*, u, S_2). \tag{4.37}$$

Then, from Lemma 4.2.1,

$$\begin{aligned} u_{1k} &\rightharpoonup \bar{u}_1 \text{ in } W^{1,2}(\Omega) \text{ when } k \to +\infty, \\ u_{2k} &\rightharpoonup \bar{u}_2 \text{ in } W^{1,2}(\Omega) \text{ when } k \to +\infty, \end{aligned} \tag{4.38}$$

where $\bar{u}_1, \bar{u}_2 \in \mathcal{U}$ are the equilibrium configurations corresponding to $\bar{\phi}$ and $\bar{\varepsilon}^*$ for $S = S_1$ and $S = S_2$:

$$\bar{u}_1 = \arg\min_{u \in \mathcal{U}} \ \mathcal{E}_f(\bar{\phi}, \bar{\varepsilon}^*, u, S_1), \qquad \bar{u}_2 = \arg\min_{u \in \mathcal{U}} \ \mathcal{E}_f(\bar{\phi}, \bar{\varepsilon}^*, u, S_2). \tag{4.39}$$

From Lemma 4.2.2,

$$\lim_{k\to\infty} \ \mathcal{C}(\phi_k, \hat{\varepsilon}_k^*, S_1) = \mathcal{C}(\bar{\phi}, \bar{\varepsilon}^*, S_1), \qquad \lim_{k\to\infty} \ \mathcal{C}(\phi_k, \hat{\varepsilon}_k^*, S_1) = \mathcal{C}(\bar{\phi}, \bar{\varepsilon}^*, S_2). \tag{4.40}$$

It follows

$$\lim_{k\to\infty} \ \bar{\mathcal{O}}(\mathcal{C}(\phi_k, \hat{\varepsilon}_k^*, S_1), \mathcal{C}(\phi_k, \hat{\varepsilon}_k^*, S_2)) = \bar{\mathcal{O}}(\mathcal{C}(\bar{\phi}, \bar{\varepsilon}^*, S_1), \mathcal{C}(\bar{\phi}, \bar{\varepsilon}^*, S_2)). \tag{4.41}$$

Therefore,

$$\lim_{k\to\infty} \ \mathcal{O}(\phi_k, \hat{\varepsilon}_k^*) = \mathcal{O}(\bar{\phi}, \bar{\varepsilon}^*). \tag{4.42}$$

Since $\{\phi_k\}$, $\{\hat{\varepsilon}_k^*\}$ is a minimizing sequence,

$$\mathcal{O}(\bar{\phi}, \bar{\varepsilon}^*) = \inf_{\phi \in \mathcal{D}_\phi, \ \hat{\varepsilon}^* \in D_\varepsilon^{QC}} \ \mathcal{O}(\phi, \hat{\varepsilon}^*). \tag{4.43}$$

□

Thus far, we have shown well-posedness of the optimization problem over the relaxed space of transformation strains. We will now show that there exists optimal solutions that have transformation strains of the form (4.2) for a certain class of objective functions. That is, solutions exist without relaxing the transformation strains which are optimal for the relaxed problem. We consider the space of transversly isotropic transformation strains

$$\mathcal{D}_\varepsilon = \left\{ \hat{\varepsilon}^* : \hat{\varepsilon}^*(x) = \frac{1}{2}[3a(x) \otimes a(x) - I_{3\times 3}], \ a(x) \in \mathcal{S}^2, \ \text{for all } x \in \Omega \right\}. \tag{4.44}$$

Theorem 4.2.4 (Optimality of transversely isotropic transformation strains)**.** *Consider an objective that depends on both an actuated and un-actuated compliance,*

$$\mathcal{O}(\phi, \hat{\varepsilon}^*) := \bar{\mathcal{O}}(\mathcal{C}(\phi, \hat{\varepsilon}^*, S), \mathcal{C}(\phi, \hat{\varepsilon}^*, 0)). \tag{4.45}$$

If $\bar{\mathcal{O}}$ is affine in the actuated compliance, then there exists $\bar{\phi} \in \mathcal{D}_\phi$ and $\bar{\varepsilon}^* \in \mathcal{D}_\varepsilon$ such that,

$$\mathcal{O}(\bar{\phi}, \bar{\varepsilon}^*) = \inf_{\phi \in \mathcal{D}_\phi, \ \hat{\varepsilon}^* \in \mathcal{D}_\varepsilon} \ \mathcal{O}(\phi, \hat{\varepsilon}^*) = \inf_{\phi \in \mathcal{D}_\phi, \ \hat{\varepsilon}^* \in \mathcal{D}_\varepsilon^{QC}} \ \mathcal{O}(\phi, \hat{\varepsilon}^*). \tag{4.46}$$

Proof. From Theorem 4.2.3, there exists $\bar{\phi} \in \mathcal{D}_\phi$ and $\bar{\varepsilon}^* \in \mathcal{D}_\varepsilon^{QC}$ such that

$$\mathcal{O}(\bar{\phi}, \bar{\varepsilon}^*) = \inf_{\phi \in \mathcal{D}_\phi,\ \hat{\varepsilon}^* \in \mathcal{D}_\varepsilon^{QC}} \mathcal{O}(\phi, \hat{\varepsilon}^*). \tag{4.47}$$

Because $\bar{\mathcal{O}}$ is affine in the actuated compliance,

$$\mathcal{O}(\phi, \hat{\varepsilon}^*) = h_0(\mathcal{C}(\phi, \hat{\varepsilon}^*, 0)) + h_1(\mathcal{C}(\phi, \hat{\varepsilon}^*, 0))\mathcal{C}(\phi, \hat{\varepsilon}^*, S), \tag{4.48}$$

where h_0 and h_1 are some functions of the un-actuated compliance. The actuated compliance may be written as

$$\mathcal{C}(\phi, \hat{\varepsilon}^*, S) = \int_{\partial_t \Omega} t \cdot v \ dx + \mathcal{C}(\phi, \hat{\varepsilon}^*, 0), \tag{4.49}$$

where v satisfies

$$\begin{cases} -\nabla \cdot [(1 - (f * \phi)^p)\mathbb{C}_s \varepsilon(v) + (f * \phi)^p \mathbb{C}_r \varepsilon(v)] & \\ \qquad = -\nabla \cdot [(f * \phi)^p \mathbb{C}_r \varepsilon_0(S) \hat{\varepsilon}^*] & \text{in } \Omega, \\ v = 0 & \text{on } \partial_u \Omega, \\ [(1 - (f * \phi)^p)\mathbb{C}_s \varepsilon(v) + (f * \phi)^p \mathbb{C}_r \varepsilon(v)]\, n & \\ \qquad = [(f * \phi)^p \mathbb{C}_r (f * \varepsilon_0(S)) \hat{\varepsilon}^*]\, n & \text{on } \partial_f \Omega. \end{cases} \tag{4.50}$$

Clearly, v is linear in $\hat{\varepsilon}^*$. Thus, there exists some fundamental solution, G, such that

$$v(x) = \int_\Omega G(x, y) \hat{\varepsilon}^*(y) \ dy \tag{4.51}$$

almost everywhere. Then, the objective can be written as

$$\begin{aligned} \mathcal{O}(\phi, \hat{\varepsilon}^*) &= h_0(\mathcal{C}(\phi, \hat{\varepsilon}^*, 0)) + h_1(\mathcal{C}(\phi, \hat{\varepsilon}^*, 0)) \left[\int_{\partial_t \Omega} t \cdot v \ dx + \mathcal{C}(\phi, \hat{\varepsilon}^*, 0) \right] \\ &= h_0(\mathcal{C}(\phi, \hat{\varepsilon}^*, 0)) \\ &\quad + h_1(\mathcal{C}(\phi, \hat{\varepsilon}^*, 0)) \left[\int_{\partial_t \Omega} t \cdot \int_\Omega G(x, y) \hat{\varepsilon^*}(y) dy \ dx + \mathcal{C}(\phi, \hat{\varepsilon}^*, 0) \right] \end{aligned} \tag{4.52}$$

or

$$\begin{aligned} &\mathcal{O}(\phi, \hat{\varepsilon}^*) = \\ &\quad h_0(\mathcal{C}(\phi, \hat{\varepsilon}^*, 0)) \\ &\quad + h_1(\mathcal{C}(\phi, \hat{\varepsilon}^*, 0)) \left[\int_\Omega \int_{\partial_t \Omega} t(x) \cdot G(x, y) \hat{\varepsilon^*}(y) \ dx \ dy + \mathcal{C}(\phi, \hat{\varepsilon}^*, 0) \right]. \end{aligned} \tag{4.53}$$

For a fixed ϕ, we consider

$$\inf_{\hat{\varepsilon}^* \in \mathcal{D}_\varepsilon^{QC}} \mathcal{O}(\phi, \hat{\varepsilon}^*). \tag{4.54}$$

The unactuated compliance is independent of $\hat{\varepsilon}^*$, so we may localize to

$$\min_{\hat{\varepsilon}^*(y)\in\mathcal{D}_\varepsilon^{QC}} I(\hat{\varepsilon}^*(y), y) := h_1 \int_{\partial_t\Omega} t(x)\cdot G(x,y)\hat{\varepsilon^*}(y)\, dx \tag{4.55}$$

for each $y \in \Omega$. Suppose this minimum is attained by

$$\hat{\varepsilon}^*(y) = \sum_{i=1}^{3} \varepsilon_i e_i \otimes e_i \tag{4.56}$$

where ε_i and e_i the principle values and corresponding axis of $\hat{\varepsilon}^*$. We must have that

$$\begin{aligned} \{\varepsilon_1,\varepsilon_2,\varepsilon_3\} = \arg\min_{\varepsilon_1,\varepsilon_2,\varepsilon_3} \quad & I(\hat{\varepsilon}^*(y), y) = \sum_{i=1}^{3} I_i(y)\varepsilon_i \\ \text{s.t.} \quad & -1 \le \varepsilon_1,\varepsilon_2,\varepsilon_3 \le 1/2 \\ & \varepsilon_1+\varepsilon_2+\varepsilon_3 = 0 \end{aligned} \tag{4.57}$$

where

$$I_i(y) := h_1 \int_{\partial_t\Omega} t(x)\cdot G(x,y)e_i\otimes e_i\, dx. \tag{4.58}$$

This is a standard linear programming problem. It is established that extremum values are guaranteed to be found at a vertex. In this case, it is when one of $\{\varepsilon_1,\varepsilon_2,\varepsilon_3\}$ takes the value -1 and the others $1/2$. This holds for all $y \in \Omega$, so there exists a $\bar{\varepsilon}^* \in \mathcal{D}_\varepsilon$ and $\bar{\phi} \in \mathcal{D}_\phi$ which minimizes (4.47). Because $\mathcal{D}_\varepsilon \subset \mathcal{D}_\varepsilon^{QC}$,

$$\mathcal{O}(\bar{\phi},\bar{\varepsilon}^*) = \inf_{\phi\in\mathcal{D}_\phi,\ \hat{\varepsilon}^*\in\mathcal{D}_\varepsilon} \mathcal{O}(\phi,\hat{\varepsilon}^*) = \inf_{\phi\in\mathcal{D}_\phi,\ \hat{\varepsilon}^*\in\mathcal{D}_\varepsilon^{QC}} \mathcal{O}(\phi,\hat{\varepsilon}^*). \tag{4.59}$$

□

4.2.4 With Voids

We now consider a responsive structure with voids or holes in the domain. In this case, $\chi_s + \chi_r \le 1$. We introduce a SIMP interpolation and filter as before through an additional density variable. We consider $\rho : \Omega \mapsto [\rho_{min}, 1]$ for some $1 >> \rho_{min} > 0$, which determines void or solid and consider the energy functional

$$\begin{aligned} \mathcal{E}_v(\phi,\rho,\hat{\varepsilon}^*,u,S) := \int_\Omega (f*\rho)^p \left(\frac{1}{2}\right)\Big\{ & (1-(f*\phi)^p)\mathbb{C}_s\varepsilon(u)\cdot\varepsilon(u) \\ + (f*\phi)^p\mathbb{C}_r(S)\left[\varepsilon(u)-\varepsilon_0(S)\hat{\varepsilon}^*\right]\cdot\left[\varepsilon(u)-\varepsilon_0(S)\hat{\varepsilon}^*\right]\Big\}\, dx - \int_{\partial_t\Omega} t\cdot u\, ds. \end{aligned} \tag{4.60}$$

The compliance is, again,

$$\mathcal{C}(\phi, \rho, \hat{\varepsilon}^*, S) = \int_{\partial_t \Omega} t \cdot u \; ds, \tag{4.61}$$

where u is an equilibrium solution,

$$u = \arg\min_{u \in \mathcal{U}} \; \mathcal{E}_v(\phi, \rho, \hat{\varepsilon}^*, u, S). \tag{4.62}$$

As $\rho_{min} > 0$, the voids have some residual stiffness as to maintain the coercivity of 4.60. We choose this residual stiffness to be small as to have a negligible effect on the design. We again consider a compliance dependent objective

$$\inf_{\phi \in \mathcal{D}_\phi, \; \rho \in \mathcal{D}_\rho, \; \hat{\varepsilon}^* \in \mathcal{D}_\varepsilon} \; \mathcal{O}(\phi, \rho, \hat{\varepsilon}^*) := \bar{\mathcal{O}}(\mathcal{C}(\phi, \rho, \hat{\varepsilon}^*, S_1), \mathcal{C}(\phi, \rho, \hat{\varepsilon}^*, S_2)), \tag{4.63}$$

where we optimize over the space of feasible designs

$$\begin{aligned} \mathcal{D}_\phi &= \left\{ \phi : \phi \in [0,1] \text{ a.e. in } \Omega, \int_\Omega \rho\phi \; dx \leq \bar{V}_r \right\}, \\ \mathcal{D}_\rho &= \left\{ \rho : \rho \in [\rho_{min}, 1] \text{ a.e. in } \Omega, \int_\Omega \rho \; dx \leq \bar{V}_0 \right\}, \end{aligned} \tag{4.64}$$

where $\bar{V}_0$ and $\bar{V}_r$ are the allowed volumes total material and responsive material, respectively.

Theorem 4.2.5 (Existence for transversely isotropic transformation strains and voids)**.** *Consider an objective that depends on both an actuated and unactuated compliance,*

$$\mathcal{O}(\phi, \rho, \hat{\varepsilon}^*) := \bar{\mathcal{O}}(\mathcal{C}(\phi, \rho, \hat{\varepsilon}^*, S), \mathcal{C}(\phi, \rho, \hat{\varepsilon}^*, 0)). \tag{4.65}$$

If $\bar{\mathcal{O}}$ is affine in the actuated compliance, then there exists $\bar{\phi} \in \mathcal{D}_\phi$, $\bar{\rho} \in \mathcal{D}_\rho$ and $\bar{\varepsilon}^* \in \mathcal{D}_\varepsilon$ such that,

$$\begin{aligned} \mathcal{O}(\bar{\phi}, \bar{\rho}, \bar{\varepsilon}^*) &= \inf_{\phi \in \mathcal{D}_\phi, \; \rho \in \mathcal{D}_\rho, \; \hat{\varepsilon}^* \in \mathcal{D}_\varepsilon} \; \mathcal{O}(\phi, \rho, \hat{\varepsilon}^*) \\ &= \inf_{\phi \in \mathcal{D}_\phi, \; \rho \in \mathcal{D}_\rho, \; \hat{\varepsilon}^* \in \mathcal{D}_\varepsilon^{QC}} \; \mathcal{O}(\phi, \rho, \hat{\varepsilon}^*). \end{aligned} \tag{4.66}$$

Proof. The proof almost exactly the same as the case without voids in Theorem 4.2.4. □

4.3 Design for Finite Strains

We now extend the formulation to consider the design through finite deformation theory. In particular, we consider an integrated responsive structure where the active material is a liquid crystal elastomer (LCE). We formulate the design problem again for both structure and material orientation. We investigate the regularization, however, the finite deformation kinematics severely complicates the mathematics. We begin by detailing the adopted material model, before discussing the chosen objective function and optimization formulation.

4.3.1 Material Model

Upon heating, LCEs transform from an ordered nematic state where mesogens prefer to be aligned, to a disordered isotropic state without such preference. This induces large deformation which must be treated by finite deformation kinematics. Here, we consider the LCE to be manufactured in the nematic state with a spatially varying initial alignment direction with order parameter $r_0 > 1$. Upon stimulation, the order parameter r decreases where a value of unity represents a completely isotropic, nematic state. We analyze the problem in a 3D setting, as the 2D problem is strictly easier. We consider an open, bounded region $\Omega \subset \mathbb{R}^3$. Again, we assume a boundary load t acting on boundary $\partial_t\Omega \subset \partial\Omega$, and fixed displacements $u = u_0$ on boundary $\partial_u\Omega \subset \partial\Omega$. Additionally, we consider $a : \Omega \mapsto \mathcal{S}^2$ as the spatially varying initial alignment. We assume the internal strain energy density of the LCE to be [16]

$$W_l(a, r, r_0, F) = \tilde{W}_l(\ell^{-1/2}(r) F \ell_0^{1/2}(r_0)), \tag{4.67}$$

for some deformation gradient F. We assume $\tilde{W}$ to be an isotropic, compressible Mooney-Rivlin energy density

$$\begin{aligned} \tilde{W}_l(M) =& \frac{\mu_l}{2}\left(\|M\|_M^2 - 3 - 2\log(\mathrm{Det}M)\right) \\ &+ \frac{\alpha\mu_l}{2}\left(\|\mathrm{Adj}M\|_M^2 - 3 - 4\log(\mathrm{Det}M)\right) \\ &+ \frac{\mu_l\nu}{1-2\nu}(\mathrm{Det}M - 1)^2, \end{aligned} \tag{4.68}$$

$\|\cdot\|_M$ denotes the Frobenius norm. μ_l and ν_l are the shear modulus and the Poisson ratio, while $\alpha << 1$ is a small constant to ensure near Neo-Hookean behavior while preserving coercivity. $\ell_0^{1/2}$ is the transversely isotropic deformation experienced by the material from an isotropic state to the nematic state

along direction a,

$$\ell_0^{1/2}(r_0) = r_0^{-1/6}(I_{3x3} + (r_0^{1/2} - 1)a \otimes a). \tag{4.69}$$

$\ell^{1/2}$ is the deformation experienced by the material through re-orientation of the mesogens. Here, we assume the LCE to be heavily cross-linked. Thus, the re-orientation of the nematic director is described by the deformation of its orthogonal plane [16]

$$\ell^{-1/2}(r) = r^{1/6}\left(I_{3x3} + (r^{-1/2} - 1)\frac{F^{-T}a}{\|F^{-T}a\|} \otimes \frac{F^{-T}a}{\|F^{-T}a\|}\right). \tag{4.70}$$

In the transformed, isotropic state, the order parameter takes the value of unity. Thus, $\ell^{-1/2}(1) = I_{3\times3}$, and the material experiences a spontaneous deformation of $\ell_0^{-1/2}(r_0)$, which corresponds to a contraction along a by $r^{-1/3}$ and extension along the perpendicular directions by $r^{1/6}$. We consider a structure composed of both the LCE as well as a passive, finite elastic material described by internal energy density W_p. As in (4.4), we consider a relaxed energy for displacement field $u : \Omega \mapsto \mathbb{R}^3$

$$\begin{aligned} \mathcal{E}(\phi, a, u, r) &:= \mathcal{W}(\phi, a, u, S) - \int_{\partial_t\Omega} t \cdot u \; d\Omega, \\ \mathcal{W}(\phi, a, u, r) &:= \int_\Omega \left[(1 - (f * \phi)^p)W_p(F) + (f * \phi)^p W_l(a, r, r_0, F)\right] \; d\Omega, \end{aligned} \tag{4.71}$$

where $F(u) := \nabla u + I_{3\times3}$ is the deformation gradient. W_p is a poly-convex strain energy function

$$W_p(F) = \bar{W}_p(F, \mathrm{Adj}F, \mathrm{Det}F), \tag{4.72}$$

where $\bar{W}_p$ is convex in each of its arguments, and satisfy the growth conditions outlined in [5].

To characterize designs, we consider deformations which minimize this energy. Thus, we prove existence of such minimizers.

Lemma 4.3.1. *Suppose W_p is polyconvex with $W_p(B) \geq C_1\|B\|_F^p - C_2$, for $p > 3$, W_l is of the form (4.67) with $\tilde{W}_l$ as the Mooney-Rivlin energy density from (4.68), and $t \in L^1(\partial_t\Omega)$. There exists a solution $u^{eq} \in \mathcal{U}$ such that*

$$\begin{aligned} \mathcal{E}(\phi, a, u^{eq}, S) &= \inf_{u\in\mathcal{U}} \mathcal{E}(\phi, a, u, S), \\ \mathcal{U} &:= \{u \in W^{1,p} : \; u = u_0 \text{ on } \partial_u\Omega\}. \end{aligned} \tag{4.73}$$

Proof. It suffices to show polyconvexity of $W_l(a, r, r_0, F)$ in F. We do so for $r_0 = 1$ and then extend this for arbitrary $r_0 > 1$. Substituting $M = \ell^{-1/2}F$ in (4.68),

$$\begin{aligned} W_l(a, r, 1, F) &= \tilde{W}_l(\ell^{-1/2}F) \\ &= \frac{\mu}{2}\left(\operatorname{Tr}\left(F^T\ell^{-1}F\right) - 3 - 2\log\det(\ell^{-1/2}F)\right) \\ &\quad + \frac{\alpha\mu}{2}\left(\operatorname{Tr}\left(\operatorname{adj}(\ell^{-1/2}F)\operatorname{adj}(\ell^{-1/2}F)^T\right) - 3 - 4\log\det(\ell^{-1/2}F)\right) \\ &\quad + \frac{\mu\nu}{1-2\nu}(\det(\ell^{-1/2}F) - 1)^2. \end{aligned} \tag{4.74}$$

It is a straight-forward calculations to show that

$$\operatorname{Tr}\left(F^T\ell^{-1}F\right) = r^{1/3}\left(\|F\|_M^2 + (r^{-1} - 1)\left(a \cdot F^{-1}F^{-T}a\right)^{-1}\right). \tag{4.75}$$

Recalling that $\operatorname{adj} M = (\det M)M^{-T}$ when $\det M \neq 0$,
$\operatorname{adj}(\ell^{-1/2}F) = \operatorname{adj}(\ell^{-1/2})\operatorname{adj}(F) = \ell^{1/2}\operatorname{adj}(F)$. Further,
$\ell^{1/2} = r^{-1/6}(I + (r^{1/2} - 1)(\operatorname{adj} Fa \otimes \operatorname{adj} Fa)/\|\operatorname{adj} Fa\|^2)$. It follows that

$$\begin{aligned} &\operatorname{Tr}\left(\operatorname{adj}(\ell^{-1/2}F)\operatorname{adj}(\ell^{-1/2}F)^T\right) = \\ &\qquad r^{1/3}\left(\|\operatorname{adj} F\|_M^2 + (r-1)\frac{\left\|(\operatorname{adj} F)^T(\operatorname{adj} F)a\right\|^2}{\|\operatorname{adj} Fa\|^2}\right). \end{aligned} \tag{4.76}$$

Finally, $\det(\ell^{-1/2}F) = \det F$. Putting these together,

$$W_l(a, r, 1, F) = \frac{\mu r^{1/3}}{2}W_1(F) + \frac{\alpha\mu r^{-1/3}}{2}W_2(\operatorname{adj} F) + W_3(\det F) \tag{4.77}$$

where

$$\begin{aligned} W_1(A) &= \|A\|_M^2 + (r^{-1} - 1)\left(a \cdot A^{-1}A^{-T}a\right)^{-1} - 3r^{-1/3}, \\ W_2(A) &= \|A\|_M^2 + (r-1)\frac{\left\|(A)^TAa\right\|^2}{\left\|Aa^2\right\|} - 3r^{1/3}, \\ W_3(x) &= -(\mu + 2\alpha\mu)\log(\det(x)) + \frac{\mu\nu}{1-2\nu}(x-1)^2. \end{aligned} \tag{4.78}$$

Note that W_1, W_2 are homogeneous of degree 2. Define

$$\begin{aligned} m_1 &= \max_{\|A\|_M=1, \|B\|_M=1} B \cdot \left(\frac{\partial^2}{\partial A^2}\left(a \cdot A^{-1}A^{-T}a\right)^{-1}\right) B, \\ m_2 &= \max_{\|A\|_M=1, \|B\|_M=1} B \cdot \left(\frac{\partial^2}{\partial A^2}\frac{\left\|A^TAa\right\|^2}{\left\|Aa^2\right\|}\right) B. \end{aligned} \tag{4.79}$$

It is easy to see that m_1, m_2 exist and are finite. Therefore, there exists $r^* > 1$ such that the second derivatives of W_1, W_2 are positive definite and therefore W_1, W_2 are convex for any $r \in [1, r^*]$. Finally, W_3 is convex, and therefore $W_l(a, r, 1, F)$ is polyconvex in F for any given $a, r \in [1, r^*]$. Therefore, existence follows in light of the growth conditions [5, 13].

Turning now to the general case $r_0 > 1$, observe that

$$W_l(a, r, r_0, F) = W_l(a, r, 1, F\ell_0^{1/2}). \tag{4.80}$$

The polyconvexity and the growth conditions are preserved, and therefore existence follows.

□

4.3.2 Optimization

To characterize the design, we consider the stimulus dependent compliance. In the small strain setting this is $\int_{\partial_t\Omega} t \cdot u \, d\Omega$, where u is the energy minimizer. However, because the possible multiplicity of the solutions, we instead consider

$$\mathcal{C}(\phi, a, r) := \inf_{u \in \mathcal{U}_{min}(\phi,a,r)} \int_{\partial_t\Omega} t \cdot u \, d\Omega, \tag{4.81}$$

where $\mathcal{U}_{min}(\phi, a, r)$ is the set of energy minimizing configurations. This is the technique used in [24]. While we might be concerned with the worst-case compliance, that is the maximum over equilibrium solutions, this lacks sequential weak lower semicontinuity. Thus, we will consider the minimum compliance over equilibrium solutions, as we will see it allows us to prove existence to the optimal design problem.

We must now choose a suitable objective to optimize. In [2], it is shown that minimizing the ratio of the stimulated to un-stimulated compliance in the small-strain setting is equivalent maximizing the blocking load. However, optimizing for blocking load does not exploit the large deformations and shape-change the structure may undergo through actuation. Thus, we choose to consider the compliance ratio,

$$\inf_{\phi \in \mathcal{D}_\phi,\ a \in \mathcal{N}} \quad \frac{\mathcal{C}(\phi, a, 1)}{\mathcal{C}(\phi, a, r)}, \tag{4.82}$$

where $\mathcal{N}$ is the space of unit vector fields on Ω,

$$\mathcal{N} := \{a : a(x) \in \mathcal{S}^{n-1} \text{ a.e. on } \Omega\}. \tag{4.83}$$

In the small strain setting, we proved that additional regularization was not necessary. However, in the current setting there may be fine structure formation in a; the nonlinearity in the kinematics and material model now allow fine mixtures of actuation strains to be favorable. To address this, we consider a modified problem where we regularize a through penalizing the gradients of the director field,

$$\inf_{\phi\in\mathcal{D}_\phi,\ a\in\mathcal{D}_a} \quad \mathcal{O}(\phi,a) := \frac{\mathcal{C}(\phi,a,1)}{\mathcal{C}(\phi,a,r)} + \mathcal{P}(a), \tag{4.84}$$

where

$$\mathcal{P}(a) := \int_\Omega \left[\frac{r_g}{4}\|\nabla a\|^4\right]\, d\Omega, \tag{4.85}$$

$$\mathcal{D}_a := \{a \in W^{1,4}(\Omega),\ a(x) \in \mathcal{S}^{n-1} \text{ a.e. on } \Omega\}, \tag{4.86}$$

and we reuse the definition of $\mathcal{D}_\phi$ from (4.64). We may prove existence to the optimization problem under some suitable assumptions. Following a similar study which analyzed existence for finite deformation structures [24], we require two lemmas to support this. The first being the sequential lower-semicontinuity of the energy function, and the second being its $\Gamma-$convergence. This enables us to establish lower-semincontinuity of the compliancs, which we then use to prove existence.

Lemma 4.3.2. *Suppose W_p is isotropic and polyconvex with $W_p(B) \geq C_1\|B\|_F^p - C_2$, for $p > 3$, W_l is of the form (4.67) with $\tilde{W}_l$ as the Mooney-Rivlin energy density from (4.68), and $t \in L^1(\partial_t\Omega)$. Then $\mathcal{W}(\phi,a,u,S)$ is sequentially lower semi-continuous along sequences $\{\phi_k,a_k,u_k\} \subset \mathcal{D}_\phi \times \mathcal{D}_n \times \mathcal{U}$ with $\phi_k \rightharpoonup \bar{\phi}$ in $L^2(\Omega)$, $a_k \rightharpoonup \bar{a}$ in $W^{1,s}(\Omega)$, $s > 3$, $u_k \rightharpoonup \bar{u}$ in $W^{1,p}(\Omega)$ with $(F(u_k), Adj\, F(u_k), Det\, F(u_k)) \rightharpoonup (F(\bar{u}), Adj\, F(\bar{u}), Det\, F(\bar{u}))$ in $L^p(\Omega)\times L^q(\Omega)\times L^r(\Omega)$ for $q,r > 1$.*

Proof. Notice that since $\tilde{W}_l$ is isotropic,

$$W_l(a,r,r_0,F) = W_l(e,r,r_0,FR(a)) \tag{4.87}$$

where $R(a) \in SO(3)$ is the minimal rotation that maps a constant unit vector $e \in \mathbb{R}^3$ to a. As $\{a_k\}$ is a bounded sequence in $W^{1,s}(\Omega)$, the compact embedding of $W^{1,s}(\Omega)$ in $L^\infty(\Omega)$ gives $a_k \to \bar{a}$ strongly in $L^\infty(\Omega)$. Additionally,

$R(a_k) \to R(\bar{a})$ strongly in $L^\infty(\Omega)$. Then,

$$\begin{aligned}(F(u_k)R(a_k),\ \mathrm{Adj}(F(u_k)R(a_k)),\ \mathrm{Det}(F(u_k)R(a_k))) &\rightharpoonup \\ (F(\bar{u})R(\bar{a})),\ \mathrm{Adj}(F(\bar{u})R(\bar{a})),\ \mathrm{Det}(F(\bar{u})R(\bar{a}))) & \\ \text{in } L^p(\Omega) \times L^q(\Omega) \times L^r(\Omega). &\end{aligned} \tag{4.88}$$

Following the arguments of [24] and using the continuity of $\mathcal{W}$ with $f * \phi$ and the strong convergence of $f * \phi_k \to f * \bar{\phi}$ gives the required result. Additionally, the linearity of $\mathcal{C}$ and the convergence of $\{u_k\}$ give sequential weak lower semi-continuity of the energy function $\mathcal{E}$. □

Lemma 4.3.3. *Suppose W_p is isotropic and polyconvex with $W_p(B) \geq C_1\|B\|_F^p - C_2$, for $p > 3$, W_l is of the form (4.67) with $\tilde{W}_l$ as the Mooney-Rivlin energy density from (4.68), and $t \in L^1(\partial_t\Omega)$. For a sequence $\{\phi_k, a_k\} \subset L^2(\Omega) \times W^{1,s}$, $s > 3$, where $\phi_k \rightharpoonup \bar{\phi}$ in $L^2(\Omega)$, $a_k \rightharpoonup \bar{a}$ in $W^{1,s}$, then*

$$\Gamma - \lim_{k\to\infty} \mathcal{E}(\phi_k, a_k, \cdot, S) = \mathcal{E}(\bar{\phi}, \bar{a}, \cdot, S). \tag{4.89}$$

Proof. As in [24], we only need to show Γ-convergence of $\mathcal{W}$. To establish this, we first show the lim-inf followed by the lim-sup condition [14].

Let $u_k \rightharpoonup \bar{u}$ in $W^{1,p}(\Omega)$ with $\limsup_{k\to\infty} \mathcal{W}(\phi_k, a_k, u_k, S) < \infty$. From the growth conditions of W we obtain boundedness of $(\mathrm{Adj}\ F(u_k), \mathrm{Det}\ F(u_k))$ in $L^{p/2}(\Omega) \times L^{p/3}(\Omega)$ and thus the weak convergence of a subsequence. Then, from [5], we find that $(F(u_k), \mathrm{Adj}\ F(u_k), \mathrm{Det}\ F(u_k)) \rightharpoonup$ $(F(\bar{u}), \mathrm{Adj}\ F(\bar{u}), \mathrm{Det}\ F(\bar{u}))$ in $L^p(\Omega) \times L^{p/2}(\Omega) \times L^{p/3}(\Omega)$. Lemma 4.3.2 yields the lim inf condition $\mathcal{W}(\bar{\phi}, \bar{a}, \bar{u}, S) \leq \liminf_{k\to\infty} \mathcal{W}(\phi_k, a_k, u_k, S)$.

For the lim sup condition we consider the convergence of $\mathcal{W}(\phi_k, a_k, \bar{u}, S)$. From the weak convergence of ϕ_k, the properties of the filter, and the strong convergence of a_k in L^∞, the integrand of $\mathcal{W}(\phi_k, a_k, \bar{u}, S)$ converges pointwise to the integrand of $\mathcal{W}(\bar{\phi}, \bar{a}, \bar{u}, S)$. Additionally,

$$\begin{aligned}(1 - (f * \phi)^p)W_p(F(\bar{u})) + (f * \phi)^p W_l(a_k, r, r_0, F(\bar{u})) & \\ \leq W_p(F(\bar{u})) + W_l(a_k, r, r_0, F(\bar{u})). &\end{aligned} \tag{4.90}$$

As a_k is uniformly bounded in $L^\infty(\Omega)$, we may assume that $W_l(a_k, r, r_0, F(\bar{u}))$ is uniformly bounded. Thus

$$(1 - (f * \phi)^p)W_p(F(\bar{u})) + (f * \phi)^p W_l(a_k, r, r_0, F(\bar{u})) \leq G(\bar{u}), \tag{4.91}$$

where G is some measurable function independent of k. Then, by Lebesque dominated convergence, $\lim_{k\to\infty} \mathcal{W}(\phi_k, a_k, \bar{u}, S) = \mathcal{W}(\bar{\phi}, \bar{a}, \bar{u}, S)$. For a recovery sequence $u_k = \bar{u}$ for all k, $\limsup_{k\to\infty} \mathcal{W}(\phi_k, a_k, u_k, S) = \mathcal{W}(\bar{\phi}, \bar{a}, \bar{u}, S)$. This proves the lim sup condition. □

Before we prove existence to the optimization problem 4.84, we require weak lower-semicontinuity of $\mathcal{C}(\phi, a, r)$ along sequences of designs.

Theorem 4.3.4. *Suppose W_p is isotropic and polyconvex with $W_p(B) \geq C_1\|B\|_F^p - C_2$, for $p > 3$, W_l is of the form (4.67) with $\tilde{W}_l$ as the Mooney-Rivlin energy density from (4.68), and $t \in L^1(\partial_t\Omega)$. Then $\mathcal{C}(\phi, a, r)$ is sequentially lower semi-continuous along sequences $\{\phi_k, a_k\} \subset \mathcal{D}_\phi \times \mathcal{D}_n$ with $\phi_k \rightharpoonup \bar{\phi}$ in $L^2(\Omega)$, $a_k \rightharpoonup \bar{a}$ in $W^{1,s}(\Omega)$, $s > 3$.*

Proof. We may consider an energy minimizing solution $u_k \in \mathcal{U}_{min}(\phi_k, a_k, 1)$ associated with the minimum actuated compliance such that $\int_{\partial_t\Omega} t \cdot u_k \, d\Omega = \mathcal{C}(\phi_k, a_k, r)$. Then, using that u_k is an energy minimizing solution, the growth conditions on W_p and W_l gives a uniform bound on the $W^{1,4}(\Omega)$ norm. Thus, there exists a $\bar{u} \in W^{1,4}(\Omega)$ such that $u_k \rightharpoonup \bar{u}$ in $W^{1,4}(\Omega)$ up to a subsequence. Then, the Γ-convergence of Lemma 4.3.3 ensures that $\bar{u} \in \mathcal{U}_{min}(\bar{\phi}, \bar{a}, 1)$. The compact embedding of $W^{1,4}(\Omega)$ in $L^\infty(\Omega)$ gives $u_k \to \bar{u}$ strongly in $L^\infty(\Omega)$ and $L^\infty(\partial_t\Omega)$. Then, $\mathcal{C}(\phi_k, a_k, 1)$ converges to $\int_{\partial_t\Omega} t \cdot \bar{u} \, d\Omega$. As $\mathcal{C}(\bar{\phi}, \bar{a}, r) \leq \int_{\partial_t\Omega} t \cdot \bar{u} \, d\Omega$, we recover sequential lower semi-continuity of $\mathcal{C}(\phi_k, a_k, r)$.

□

With the lower semi-continuity of the compliance established, we are now ready to prove existence of optimal designs to (4.84) under some suitable assumption.

Theorem 4.3.5. *Suppose W_p is isotropic and polyconvex with $W_p(B) \geq C_1\|B\|_F^p - C_2$, for $p > 3$, W_l is of the form (4.67) with $\tilde{W}_l$ as the Mooney-Rivlin energy density from (4.68), and $t \in L^1(\partial_t\Omega)$. Consider*

$$\mathcal{O}(\phi, a) := \frac{\mathcal{C}(\phi, a, 1)}{\mathcal{C}(\phi, a, r)} + \mathcal{P}(a). \tag{4.92}$$

If the prescribed boundary displacements $u_0 = 0$ and there exists some $\{\tilde{\phi}, \tilde{a}\} \in \mathcal{D}_\phi \times \mathcal{D}_a$ such that $O(\tilde{\phi}, \tilde{a}) \leq 0$, then there exists an optimal design $\{\bar{\phi}, \bar{a}\} \in$

$\mathcal{D}_\phi \times \mathcal{D}_a$ *such that*

$$\mathcal{O}(\bar{\phi}, \bar{a}) = \inf_{\phi \in \mathcal{D}_\phi,\ a \in \mathcal{D}_a} \mathcal{O}(\phi, a). \tag{4.93}$$

Proof. We may assume that for $t \neq 0$ that $\mathcal{C}(\phi, a, r) > 0$ for all $\{\phi, a\} \in \mathcal{D}_\phi \times \mathcal{D}_a$. As $\mathcal{C}(\phi, a, 1)$ is bounded from below, $\mathcal{O}(a, \phi)$ is bounded from below.

Consider a minimizing sequence $\{\phi_k, a_k\} \subset \mathcal{D}_\phi \times \mathcal{D}_a$, and extract a subsequence such that a_k is uniformly bounded in $W^{1,4}(\Omega)$. Thus there exists a $\bar{a} \in W^{1,4}(\Omega)$ such that $a_k \rightharpoonup \bar{a}$ in $W^{1,4}(\Omega)$ up to a subsequence. From the compact embedding of $L^\infty(\Omega)$ in $W^{1,4}(\Omega)$, $a_k \to \bar{a}$ strongly in $L^\infty(\Omega)$. As magnitude is preserved under strong convergence, $\bar{a} \in \mathcal{D}_a$. Additionally, from the definition of D_ϕ, there exists a $\bar{\phi} \in \mathcal{D}_\phi$ such that $\phi_k \rightharpoonup \bar{\phi}$ in $L^2(\Omega)$ up to a subsequence. Theorem 4.3.4 gives the the sequential weak lower semicontinuity of the compliances $\mathcal{C}(\phi_k, a_k, r)$ and $\mathcal{C}(\phi_k, a_k, 1)$ as $\phi_k \rightharpoonup \bar{\phi}$ and $a_k \rightharpoonup \bar{a}$. From the condition that there exists of designs with non-positive objectives, we assume $\mathcal{C}(\phi_k, a_k, 1) \leq 0$ for $k > K$. Then, since $\mathcal{C}(\phi_k, a_k, 1) \leq 0$ and $\mathcal{C}(\phi_k, a_k, r) > 0$, the ratio $\mathcal{C}(\phi_k, a_k, 1)/\mathcal{C}(\phi_k, a_k, 0)$ remains sequentially weakly lower semicontinuous. The sequential weak lower semicontinuity of $\mathcal{P}(a)$ implies that of $\mathcal{O}(\phi_k, a_k)$, which completes the proof. □

4.3.3 With Voids

We may consider the introduction of voids in the finite elastic setting in a similar manner to Section 4.2.4. Then, Theorem 4.3.5 and the associated lemmas can straightforwardly be extended to the case for voids. We introduce the additional scalar field $\rho : \Omega \mapsto [\rho_{min}, 1]$ which indicates solid or void, and consider the energy

$$\begin{aligned} \mathcal{E}(\phi, \rho, a, u, r) &:= \mathcal{W}(\phi, \rho, a, u, r) - \int_{\partial_t \Omega} t \cdot u \; d\Omega, \\ \mathcal{W}(\phi, \rho, a, u, r) &:= \int_\Omega (f * \rho)^p [(1 - (f * \phi)^p) W_p(F) \\ &\qquad + (f * \phi)^p W_l(a, r, r_0, F)] \; d\Omega. \end{aligned} \tag{4.94}$$

Again, we consider the the minimum compliance,

$$\mathcal{C}(\phi, \rho, a, r) := \inf_{u \in \mathcal{U}_{min}(\phi, \rho, a, S)} \int_{\partial_t \Omega} t \cdot u \; d\Omega, \tag{4.95}$$

where $\mathcal{U}_{min}(\phi, \rho, a, r)$ is the set of energy minimizing displacement fields. Then, we consider minimizing the compliance ratio with the added penalty terms on

a,

$$\inf_{\phi\in\mathcal{D}_\phi,\ \rho\in\mathcal{D}_\rho,\ a\in\mathcal{D}_a} \quad \mathcal{O}(\phi,\rho,a) := \frac{\mathcal{C}(\phi,\rho,a,1)}{\mathcal{C}(\phi,\rho,a,r)} + \mathcal{P}(a), \tag{4.96}$$

where we re-use the definitions of the design spaces from (4.64) and (4.86). The existence proof for two-material designs in Theorem 4.3.5 may be simply extended for the inclusion of voids.

Theorem 4.3.6. *Suppose W_p is isotropic and polyconvex with $W_p(B) \geq C_1\|B\|_F^p - C_2$, for $p > 3$, W_l is of the form (4.67) with $\tilde{W}_l$ as the Mooney-Rivlin energy density from (4.68), and $t \in L^1(\partial_t\Omega)$. Consider*

$$\mathcal{O}(\phi,\rho,a) := \frac{\mathcal{C}(\phi,\rho,a,1)}{\mathcal{C}(\phi,\rho,a,r)} + \mathcal{P}(a). \tag{4.97}$$

If the prescribed boundary displacements $u_0 = 0$ and there exists some $\{\tilde{\phi},\tilde{\rho},\tilde{a}\} \in \mathcal{D}_\phi \times \mathcal{D}_\rho \times \mathcal{D}_a$ such that $O(\tilde{\phi},\tilde{\rho},\tilde{a}) \leq 0$, then there exists an optimal design $\{\bar{\phi},\bar{\rho},\bar{a}\} \in \mathcal{D}_\phi \times \mathcal{D}_\rho \times \mathcal{D}_a$ such that

$$\mathcal{O}(\bar{\phi},\bar{a}) = \inf_{\phi\in\mathcal{D}_\phi,\ a\in\mathcal{D}_a} \mathcal{O}(\phi,a). \tag{4.98}$$

Proof. The proof follows almost exactly as Theorem 4.3.5, where the associated lemmas and theorem may be simply extended to the case of the additional design variable. □

4.4 Examples of Lifting Actuators

We consider numerical examples using the formulations detailed in Section 4.2 and 4.3. We consider 2D and 3D lifting actuators occupying rectangular domains for both the small strain and finite deformation setting. We detail the parameterization, the numerical solution scheme, and present the converged designs. Throughout all of the presented examples, we consider a standard Galerkin finite element discretization with Largrange polynomial shape functions. As conventional, we use a discontinuous Galerkin approximation for the density variables ρ and ϕ, where their values are assumed constant on each element. The continuous filter is replaced by the discrete renormalizing filter in 2.29. The adjoint method is used to obtain the design sensitivities, and gradient-based updates are performed using the classical Method of Moving Asymptotes algorithm [41].

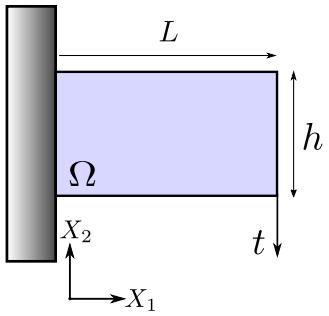

Figure 4.1: Rectangular domain of length L and height h for the 2D lifting actuator. Here, we apply a downward force t to the bottom right corner.

4.4.1 2D Lifting Actuator

Small Strains To simplify the computations in the small strain setting, we parameterize the director field through a single scalar angle $\theta : \Omega \mapsto [0, \pi)$ such that

$$a(x) = \cos(\theta(x))e_1 + \sin(\theta(x))e_2, \tag{4.99}$$

where $\{e_1, e_2\}$ is the standard basis in $\mathbb{R}^2$. Then, for optimizing a structure with voids, we consider

$$\inf_{\phi\in\mathcal{D}_\phi,\ \rho\in\mathcal{D}_\rho,\ \theta\in[0,\pi)} \mathcal{O}(\phi, \rho, a(\theta)) := \bar{\mathcal{O}}(\mathcal{C}(\phi, \rho, a, S_1), \mathcal{C}(\phi, \rho, a, S_2)). \tag{4.100}$$

We consider the optimal design of a lifting actuator on the 2D rectangular domain shown in Figure 4.1, with a vertical load applied to the bottom right-hand corner. We look to minimize the compliance ratio

$$\inf_{\phi\in\mathcal{D}_\phi,\ \rho\in\mathcal{D}_\rho,\ \theta\in[0,\pi)} \mathcal{O}(\phi, \rho, a(\theta)) = \frac{\mathcal{C}(\phi, \rho, a, 1)}{\mathcal{C}(\phi, \rho, a, 0)}. \tag{4.101}$$

We discretize the domain with a 80×40 mesh and consider a standard Galerkin finite element formulation with first order elements [12]. We set the densities ϕ and ρ to be constant on each element, as well as the material orientation angle θ. After computing the actuated and un-actuated displacement for a given design and calculating the objective, sensitivities are computed using the adjoint method. Then, we update the design through the gradient-based Method of Moving Asymptotes (MMA) [9]. This is implemented in the C++ deal.ii finite element library [6].

Figure 4.2 shows the converged designs for varying elastic modulus ratios for the responsive vs passive material, E_r/E_s. We use a fixed Poisson ratio of

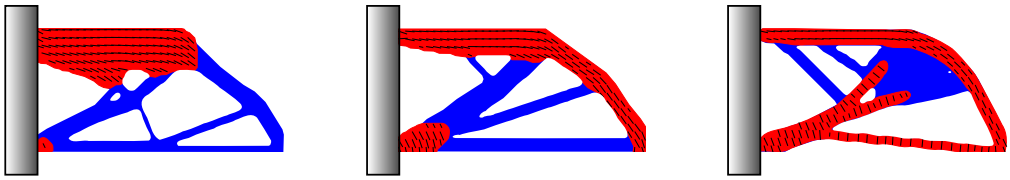

(a) $\frac{E_r}{E_s} = 0.2$ (b) $\frac{E_r}{E_s} = 1$ (c) $\frac{E_r}{E_s} = 5$

Figure 4.2: Converged designs for the rectangular lifting actuator of Figure 4.1 in the small strain setting for varying stiffness ratios for the active vs passive material. The red indicates responsive material while blue denotes passive. The director field a is shown in black lines.

$\nu = 0.48$, and aspect ratio $L/h = 2$. We see that for the case of softer responsive material, the structure contains large regions of responsive material. Conversely, for the case of stiffer responsive material, it is distributed thinly as a frame. When the stiffness of the responsive and passive material is identical, the design resembles that of a standard minimum compliance structure. Throughout all of these, the director field is oriented nearly vertical on the bottom of the structure, and horizontal at the top. This allows it to lengthen horizontally along the bottom edge and contract at the top, creating a hinging effect, and thus lifting the load.

Finite Strains In the finite strain setting, we look to optimize the same actuator shown in Figure 4.1. Here, we model both the passive and responsive materials as compressible Neo-Hookean with strain energy functions

$$\begin{aligned} \tilde{W}_l(F) &= \frac{\mu_l}{2}\left(\|F\|_F^2 - 2 - 2\log(\mathrm{Det}F)\right) + \frac{2\mu_l\nu_l}{1-2\nu_l}\left(\mathrm{Det}\ F - 1\right)^2, \\ W_p(F) &= \frac{\mu_p}{\mu_l}\tilde{W}_l(F), \end{aligned} \tag{4.102}$$

where μ_l and μ_p are the shear moduli for the LCE and passive material. We use a Poisson ratio of $\nu_l = 0.48$ as to give a near-incompressable response while avoiding locking issues which may arise numerically from a fully incompressible material model. Similar to the small strain regime, we discretize the densities ϕ and ρ as constant on each element. However, as we need to evaluate gradients of the director, we discretize this field through vector-valued first order finite elements. Thus, we consider the director field a as parameterized through its two scalar components

$$a(x) = a_1(x)e_1 + a_2(x)e_2, \tag{4.103}$$

where $\{e_1, e_2\}$ is the standard basis in $\mathbb{R}^2$. Then, after updating these through MMA, we apply a radial return to a unit vector at each nodal point.

Figure 4.3 shows converged designs for optimal compliance ratio in (4.84) for varying shear moduli ratios of responsive to passive materials for a domain aspect ratio of $L/h = 2$. This shares the general trends discussed for the small strain setting of Figure 4.2. However, they differ in that these designs use a large distribution of the responsive material along the bottom edge of the structure. Here, the finite deformation kinematics allow for the lengthening of these members to cause considerable vertical displacement.

4.4.2 3D Lifting Actuator

Small Strains In 3D, a parameterization through angles leads to a non-uniform discretization of the unit sphere. Thus, we consider the direction a parameterized through its 3 scalar components

$$a(x) = a_1(x)e_1 + a_2(x)e_2 + a_3(x)e_3 \tag{4.104}$$

where, again $\{e_i\}$ is the standard basis on $\mathbb{R}^3$.

We consider maximizing the blocking load of an actuator occupying a cantelevered rectangular prism under a uniform distributed load over a circular region on the far face shown in Figure 4.4. We update the director field through method of moving asymptotes, where we a apply a radial return to a unit vector at each element after updating. Again, we consider a Poisson ratio of $\nu = 0.48$, and domain aspect ratio $L/h = 2$. Figure 4.5 shows converged designs computed on a $80 \times 40 \times 40$ mesh. These designs are quite similar in nature to their 2D counterparts shown in 4.2.

Finite Strains In the finite strain setting, we look to optimize the same actuator shown in Figure 4.4. We consider both the passive and responsive materials as compressible Mooney-Rivlin material,

$$W_p(F) = \frac{\mu_p}{\mu_l}\tilde{W}_l(F), \tag{4.105}$$

where $\tilde{W}_l$ is the compressible Mooney-Rivlin model from (4.68). Here, we choose the $\alpha = 0.05$ to give near Neo-Hookean response while maintaining coercivity. Again, we choose a Poisson ratio of $\nu_l = 0.48$ and domain aspect

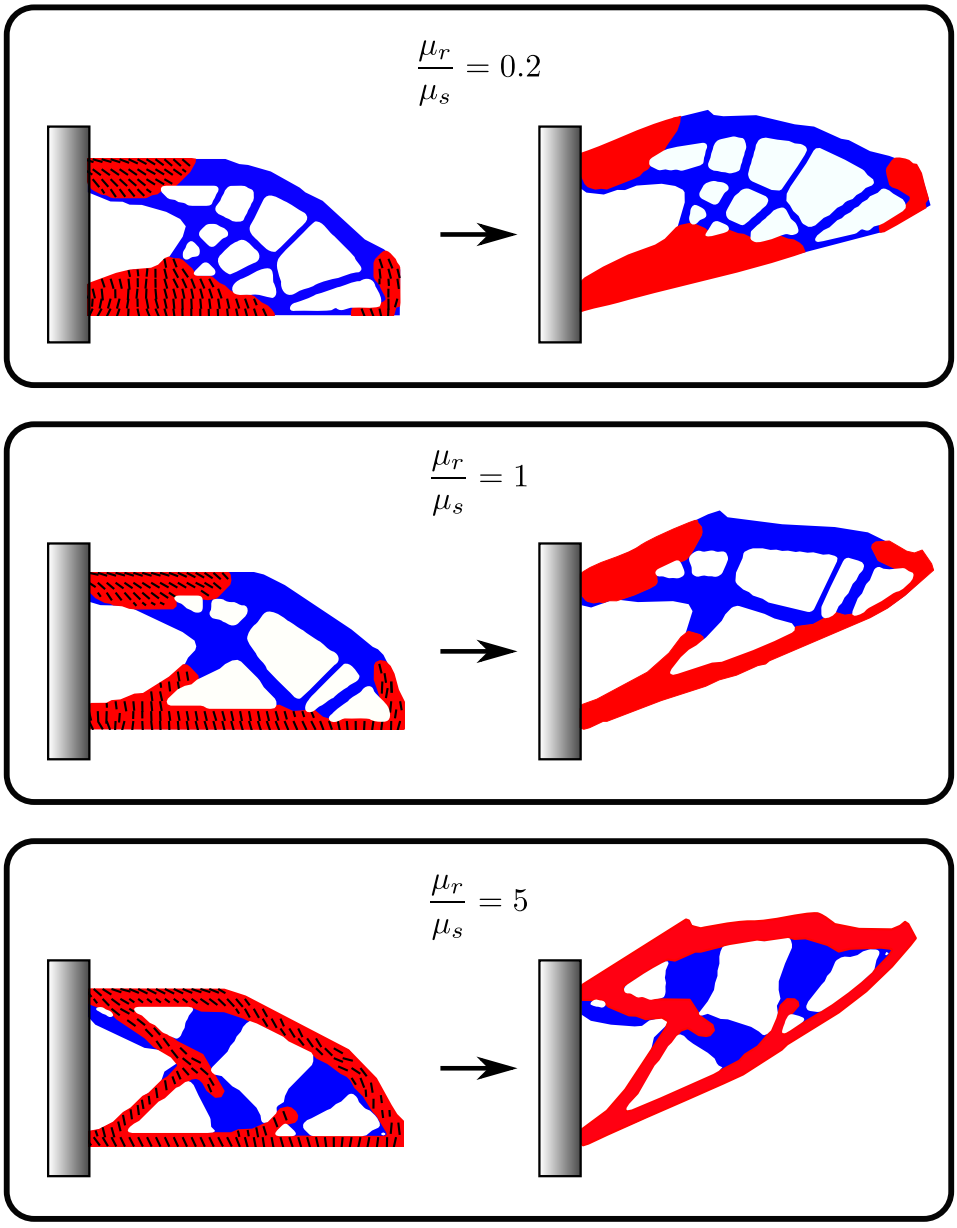

Figure 4.3: Converged designs for the rectangular lifting actuator of Figure 4.1 in the finite strain setting for varying stiffness ratios for the active vs passive material. The red indicates responsive material while blue denotes passive. The left column shows the reference configuration, with director fields a is shown in black lines. The right column shows the deformed configuration after actuation.

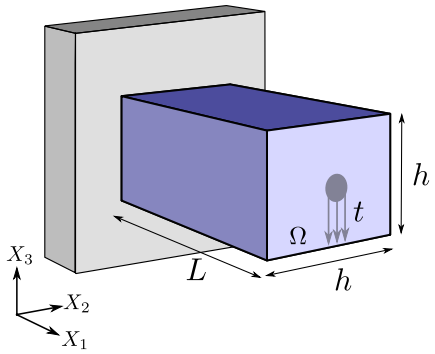

Figure 4.4: 3D rectangular domain of side lengths $L \times h \times h$ for the lifting actuator. A uniform, downward distributed load t is applied to a circular region at the center of the far face of the domain.

ratio $L/h = 2$. The director field a is parameterized through (4.104) and discretized using a first order vector-valued finite element space. Again, we update the director field through MMA, where we apply a radial return at each node after updates.

Figure 4.5 shows converged designs computed on a $80 \times 40 \times 40$ mesh. While similar to the small-strain designs of 4.5, these have a smoother variation of the director field which arises from the penalty term.

4.5 Simultaneous Design with Printing Constraints

The converged designs shown in Section 4.4 are optimized without considerations for manufacturing constraints. This results in structures that could be difficult to produce from a practical standpoint. Thus, we look to restrict the design space to those which are feasible to produce. We detail how the manufacturing pathways for LCEs impacts the structural design. Then, we present a print-aware design formulation. By restricting the space to solenoidal director fields, we ensure manufacturability through emerging 3D printing techniques. We prove well posedness in this setting, and demonstrate the formulation by revisiting the previously explored lifting actuator, designing both the structure and material orientation while recovering print paths. We observe that including these print constraints in the formulation drastically alters the design.

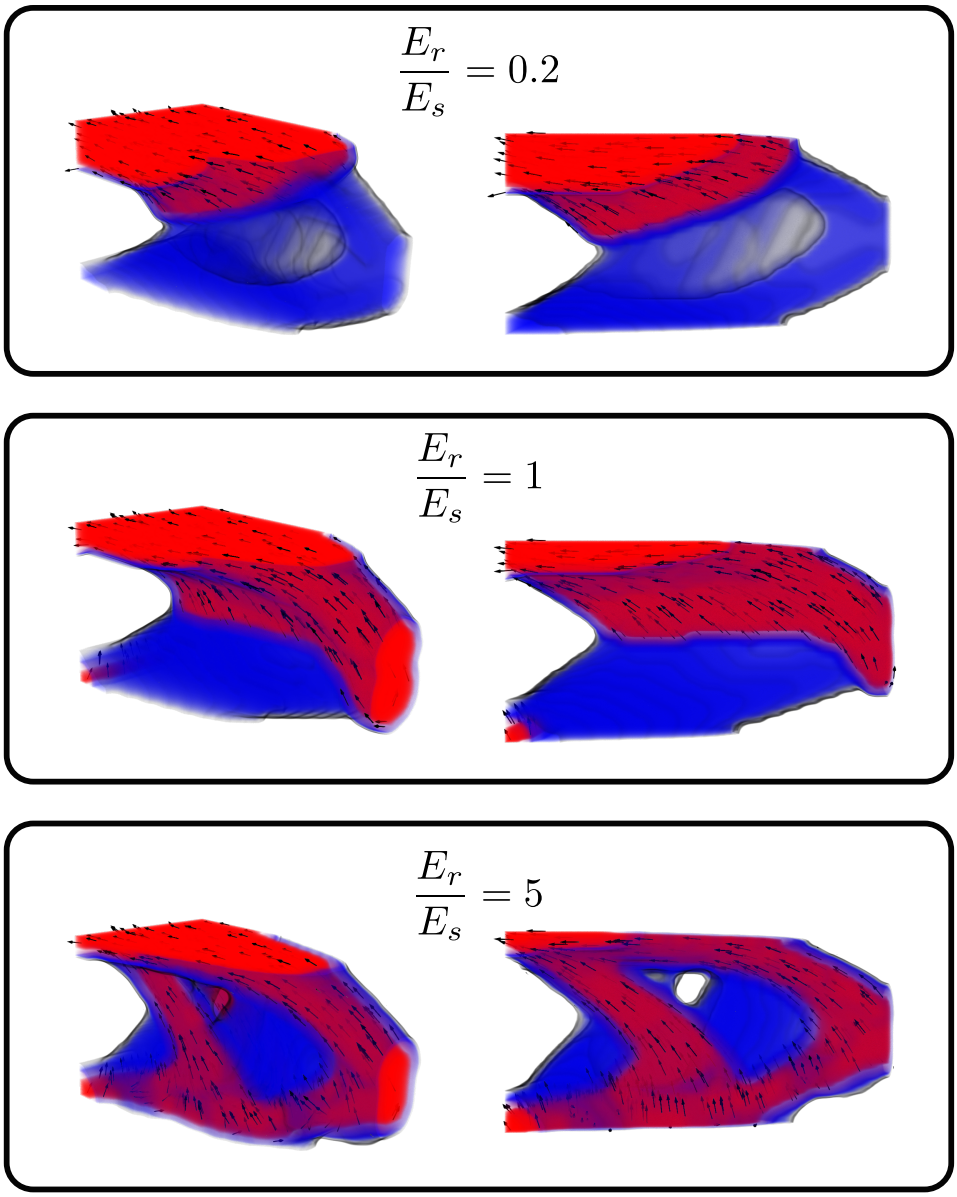

Figure 4.5: Converged designs for the 3D rectangular lifting actuator of Figure 4.4 in the small strain setting for varying stiffness ratios for the active vs passive material. The red indicates responsive material while blue denotes passive. The director field a is shown in black arrows.

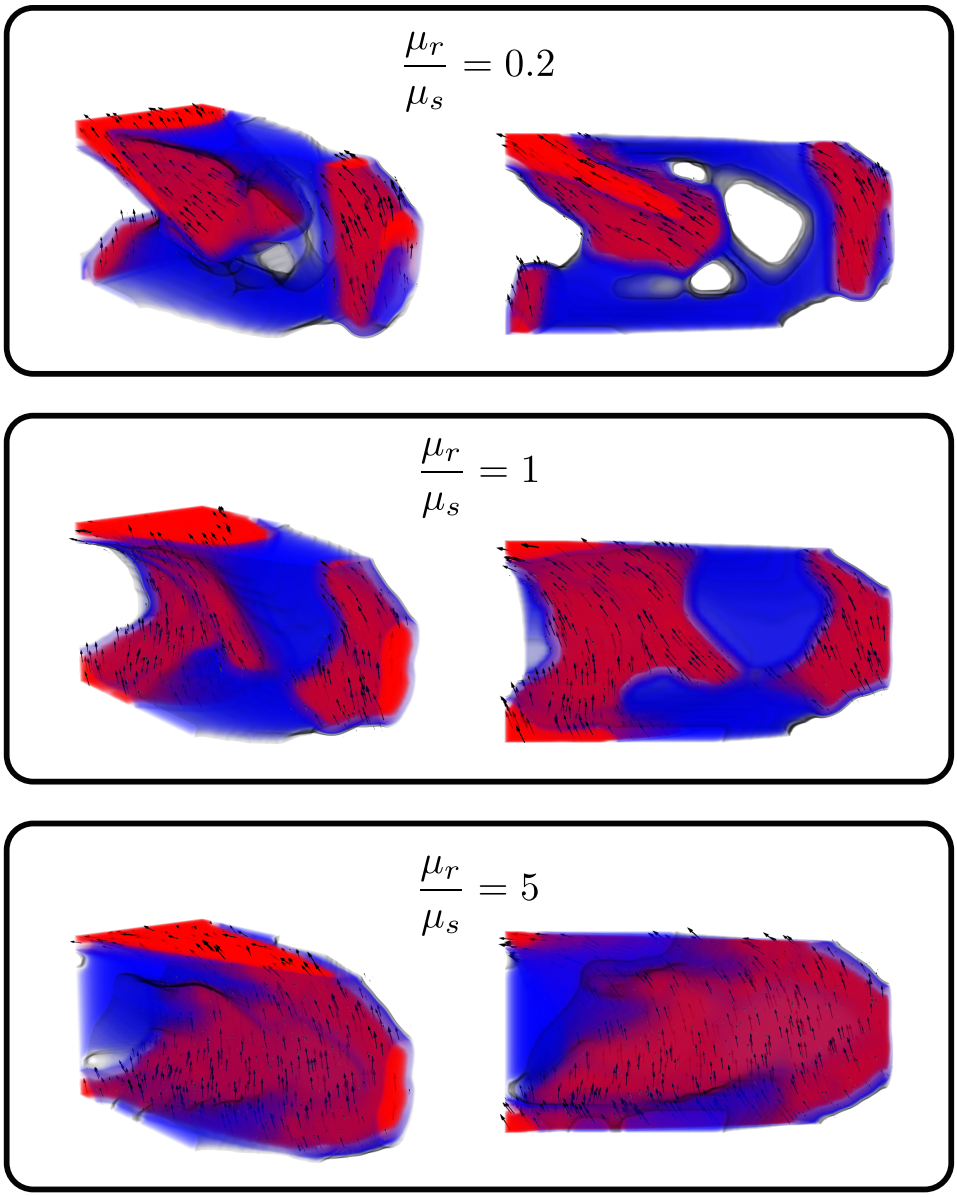

Figure 4.6: Converged designs for the 3D rectangular lifting actuator of Figure 4.4 in the finite strain setting for varying stiffness ratios for the active vs passive material. The red indicates responsive material while blue denotes passive. The director field a is shown in black arrows.

4.5.1 Formulation

LCEs are typically printed using extrusion methods, with the mesogens aligned along the extrusion axis [20, 4]. Thus, slender struts with nematic orientation misaligned with the member are inefficient to print, requiring a large number of passes. Additionally, structures with direction fields that vary heavily may not have a printable path to match both the structure and nematic direction. To this end, we look to incorporate these constraints to design both effective and manufactureable responsive structures. We analyze this in a 2D setting, as 3D printing for arbitrary directions is severely limited by the typical "layer-by-layer" methods.

We introduce the scalar valued function $\Psi : \Omega \mapsto \mathbb{R}$ whose contours describe the print path in the responsive structure domain. We constrain $\nabla\Psi \cdot a = 0$, which orients the contours along the nematic direction. Additionally, we constrain $\|\nabla\Psi\| = 1$, which ensures that these contours are evenly space. We note that the first constraint may be satisfied by $\nabla\Psi = Ra$, where $R \in SO(2)$ is a counter-clockwise $\pi/2$ rotation. Thus, Ra is a gradient field, and thus has zero curl, $\nabla \times Ra = 0$. This implies $\nabla \cdot a = 0$. Therefore, we may enforce the constraint that contours lie tangent to the direction field by ensuring that a is solenoidal. An additional requirement is reducing the number of times the print path alters course. This affects the print resolution as undesired material is layed when the print head turns around. Additionally, this increases the manufacturing duration and extends the time in which the partially cured polymer is exposed to the environment. To this end, we also penalize print paths which lie tangent to responsive material boundaries. This may occur either on the boundary of the design domain, or in the interior near holes or material interfaces.

To accomplish these requirements, we introduce an additional penalty on the director field,

$$\begin{aligned}\mathcal{P}_{print}(\phi,\rho,a) := \int_\Omega \Big[&\frac{c_1}{2} g(\rho_f) g(\phi_f) (\nabla \cdot a)^2 \\ &+ c_2 \left(g(\rho_f) \left| a \cdot \nabla \phi_f \right| + g(\phi_f) \left| a \cdot \nabla \rho_f \right| \right) \Big] d\Omega \\ &+ \int_{\partial\Omega} c_2 g(\phi_f) g(\rho_f) |a \cdot m| \, d\Gamma,\end{aligned} \tag{4.106}$$

where m is the outward unit normal of $\partial\Omega$ and the subscript f denotes filtered fields. Here, $c_1, c_2 \in \mathbb{R}^+$ are scalar constants. The first term in $\mathcal{P}_{print}$ penalizes

deviations from solenoidal director fields in the responsive structure domain. The second term penalizes director fields perpendicular to the boundary of the responsive structure inside the domain. Finally, the boundary integral penalizes director fields which are perpendicular to the boundary of the domain for responsive solid. The absence of these constraints in void or passive solid regions allow for restructuring of Ψ in these regions, which allows for accommodation of print paths in disconnected regions of active material. It is expected that $c_1 >> c_2$, as the solenoidal condition is a hard requirement while the print path altering course is only softly penalized. g is a monotonically increasing function which is chosen to ensure regions of intermediate density are not favorable. Thus, we consider

$$g(q) = 1 - (1-q)^p. \tag{4.107}$$

This penalizes intermediate densities with similar weight as fully solid or responsive regions.

The print path may be obtained by solving

$$\inf_{\Psi \in \mathcal{D}_\Psi} \quad \mathcal{O}_{print} := \int_\Omega \phi_f \rho_f \left[\frac{c_3}{2} \left(\nabla \Psi \cdot a \right)^2 + \frac{c_4}{2} (\nabla \Psi \cdot Ra - 1)^2 \right] \, d\Omega \tag{4.108}$$

where

$$\mathcal{D}_\Psi := \left\{ \Psi \in H^1(\Omega), \ \int_{\partial\Omega} \Psi \, d\Gamma = 0 \right\}. \tag{4.109}$$

By adding $\mathcal{P}_{print}$ to (4.96), we may obtain a printable structure. Then, solving (4.108) recovers the print path. We extend the proof of Theorem 4.3.6 to include the print constraints $\mathcal{P}_{print}$.

Theorem 4.5.1. *Suppose W_p is isotropic and polyconvex with $W_p(B) \geq C_1 \|B\|_F^p - C_2$, for $p > 3$, W_l is of the form (4.67) with $\tilde{W}_l$ as the Mooney-Rivlin energy density from (4.68), and $t \in L^1(\partial_t \Omega)$. Consider*

$$\mathcal{O}(\phi, \rho, a) := \frac{\mathcal{C}(\phi, \rho, a, 1)}{\mathcal{C}(\phi, \rho, a, r)} + \mathcal{P}(a) + \mathcal{P}_{print}(\phi, \rho, a). \tag{4.110}$$

If the prescribed boundary displacements $u_0 = 0$ and there exists some $\{\tilde{\phi}, \tilde{\rho}, \tilde{a}\} \in \mathcal{D}_\phi \times \mathcal{D}_\rho \times \mathcal{D}_a$ such that $O(\tilde{\phi}, \tilde{\rho}, \tilde{a}) < 0$, then there exists an optimal design $\{\bar{\phi}, \bar{\rho}, \bar{a}\} \in \mathcal{D}_\phi \times \mathcal{D}_\rho \times \mathcal{D}_a$ such that

$$\mathcal{O}(\bar{\phi}, \bar{a}) = \inf_{\phi \in \mathcal{D}_\phi, \ a \in \mathcal{D}_a} \mathcal{O}(\phi, a). \tag{4.111}$$

Proof. We need only to establish sequential lower-semicontinuity of $\mathcal{P}_{print}$ along sequences $\{\phi_k, \rho_k, a_k\} \subset \mathcal{D}_\phi \times \mathcal{D}_\rho \times \mathcal{D}_a$ with $\phi_k \rightharpoonup \bar{\phi}$ in $L^2(\Omega)$, $\rho_k \rightharpoonup \bar{\rho}$ in $L^2(\Omega)$, and $a_k \rightharpoonup \bar{a}$ in $W^{1,s}(\Omega)$, $s > 3$. Of course $f * \phi_k \to f * \bar{\rho}$, $f * \rho_k \to f * \bar{\rho}$ point-wise. As

$$\nabla(f * \psi)(x) = \int_\Omega \nabla f(x - y)\psi(y)\, dy, \tag{4.112}$$

$\nabla(f * \phi_k) \to \nabla(f * \bar{\phi})$, $\nabla(f * \rho_k) \to \nabla(f * \bar{\rho})$ point-wise as well. Additionally, $a_k \to \bar{a}$ in $L^\infty(\Omega)$. Then, as the last three terms of (4.106) are clearly uniformly bounded, Lebesgue dominated convergence implies these terms are continuous along such sequences. Finally, the convexity of $(\nabla \cdot a)^2$ in ∇a gives lower semi-continuity of the first term. □

4.5.2 Revisited 2D Lifting Actuator

Figure 4.7 shows converged designs for identical parameters which were used to generate Figure 4.3. We first examine the case of $\mu_r/\mu_s = 1$ in the middle rows of Figure 4.7 and Figure 4.3. We observe that the print considerations have a drastic impact on the design. While the free design acts as a pushing actuator with responsive material distributed along the bottom edge with nearly vertical director alignment, the print-aware design acts mainly as a pulling actuator with responsive material distributed along the top of the structure. Additionally, the nematic directors in the print-aware case are aligned with the main strut of active material. This trend is echoed in the other cases of $\mu_r/\mu_s = 0.2$ and $\mu_r/\mu_s = 5$.

4.5.3 Physical Realization of Printed Structure

With the optimal design and print paths in the responsive material regions, we may now manufacture the actuators. Prof. Taylor Ware, his student Seelay Tasmim, and his postdoctoral scholar Asaf Dana fabricated the structures at Texas A&M University. Figure 4.8 shows a design which is 3D printed using liquid crystal elastomer and passive polymer as in [4]. That is, through layer-by-layer extrusion based 3D printing followed a UV cure after the entire structure is printed. Figure 4.9 shows the actuation through heating in an oil bath. We see the expected lifting motion, verifying that the material synthesis director orientation is suitable.

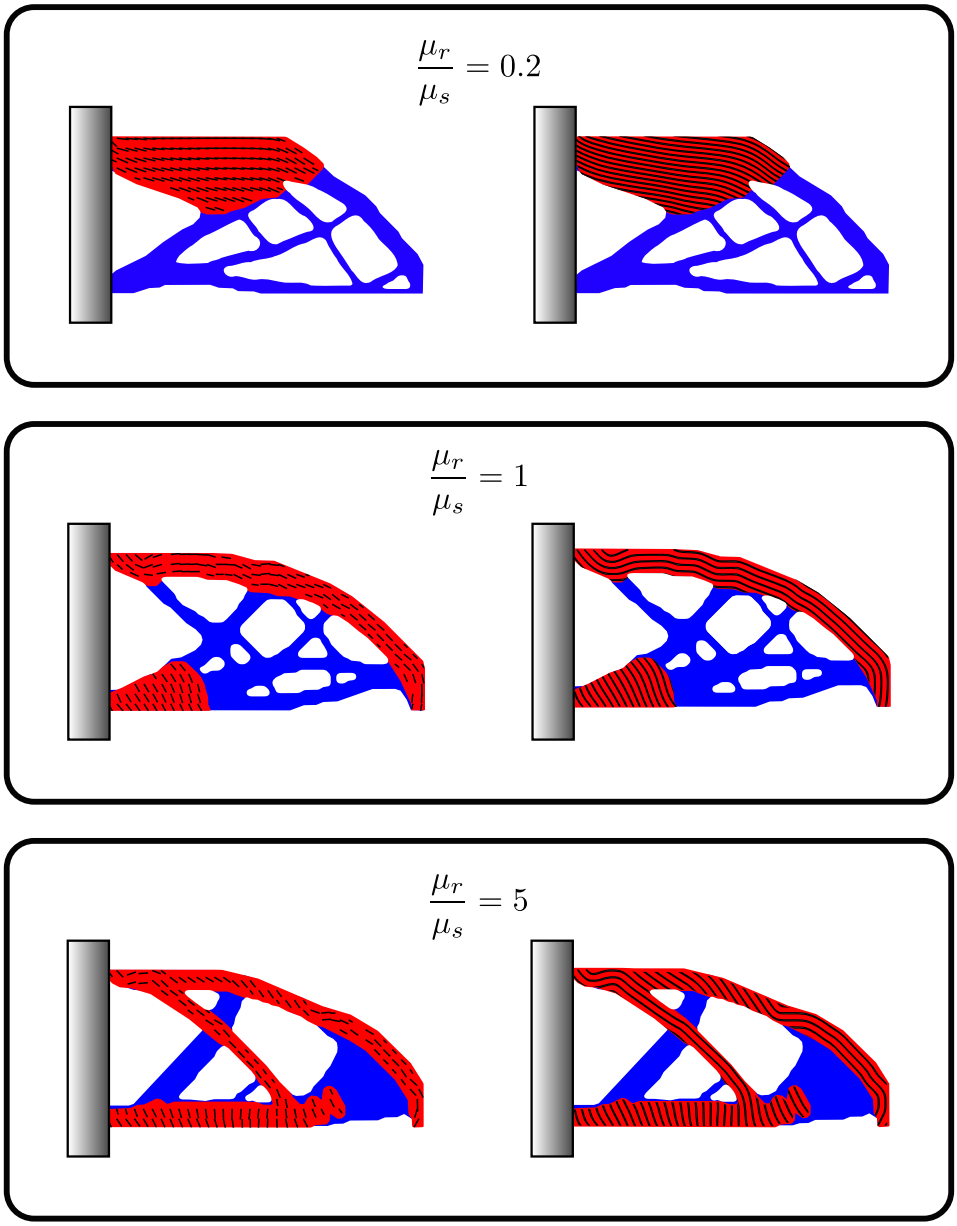

Figure 4.7: Converged designs for the rectangular lifting actuator of Figure 4.1 in the finite strain setting with the inclusion of manufacturing constraints. Designs for varying stiffness ratios for the active vs passive material are shown. The red indicates responsive material while blue denotes passive. Left column shows the reference configurations, with the director field a shown in black lines. The associated print paths for the active material domains are shown in the right column.

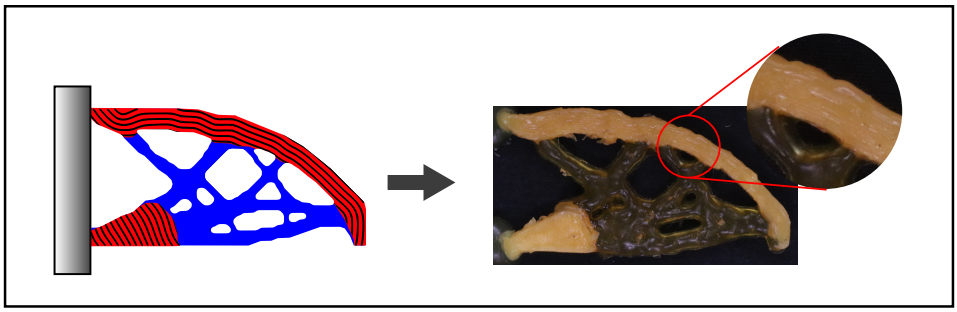

Figure 4.8: Optimal design and print path of the rectangular lifting actuator (right), along with printed structure (left). The darker yellow is the responsive material, while the transparent material is passive. We see that the print lines of the responsive structure follows the desired paths quite well.

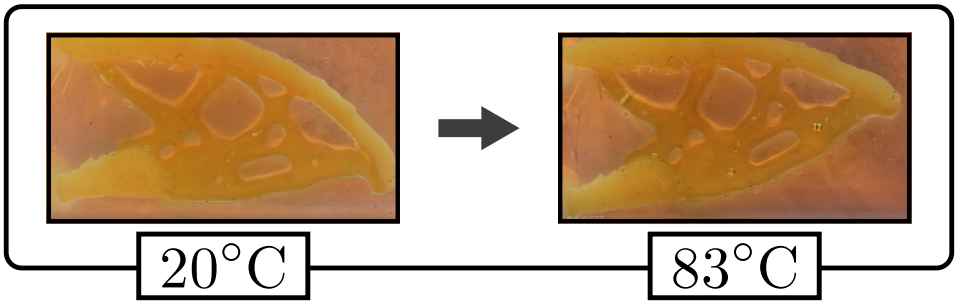

Figure 4.9: Printed structure undergoing actuation in a heated oil bath. We see that the actuation is a lifting motion as expected.

Currently, these designs are undergoing testing in a mechanical testing apparatus. We plan to compare the compliance ratio for the loaded structure to that of intuitive designs to verify optimality.

4.6 Conclusion

We have developed a general optimal design framework for soft responsive actuators. Starting with the simplified case of linearized kinematics, we developed the theory to account for finite deformation, microstructure reconfiguration, and manufacturing constraints for the model LCE system. We addressed key issues of mathematical regularization while including considerations for the fabrication pathway's effect on the material orientation. Through this, we developed a robust framework for designing actuators which take full advantage of these emerging materials and manufacturing technologies. We demonstrated this by designing lifting actuators which we physically realize through advanced 3D printing methods.

While the developed formulation is effective for the studied scenarios, it is not without its shortcomings. Here, we designed for quasi-static conditions with complete disregard for the kinetics driving actuation. In most applications, speed of response is tremendously important. Thus, the kinetics leading to actuation (e.g., heat diffusion), must be modeled and accounted for in the design formulation. Additionally, researchers have begun to develop responsive material systems with multiple actuation modes [18]. Thus, incorporating multifunctionality into the optimization framework would be a natural progression. On the theoretical side, there remains mathematical intricacies which must be solved. In particular, structural instabilities must be rigorously treated for a fully robust design approach. However, the mathematical formulation in such settings is quite unclear. This is in part due to instability phenomena being driven by the evolution of local energy minimizers, whereas the presented treatment works with global minimization. A rigorous mathematical study into these issues is required.

Even with these limitations, this work may serve as a starting point to guide actuator design towards a myriad of applications. It is straightforward to adapt the formulation to other responsive material systems including magneto-responsive structures, hydrogels, and shape memory alloys. Additionally, an identical treatment of the print constraints may be used for other anisotropic 3D printed materials. Finally, the rigorous mathematical approach we take may be extended to include design considerations necessary for application deployment such as actuation kinetics and strucrual instabilities.

BIBLIOGRAPHY

[1] E. M. Ahmed. Hydrogel: Preparation, characterization, and applications: A review. *Journal of Advanced Research*, 6(2):105–121, 2015.

[2] A. Akerson, B. Bourdin, and K. Bhattacharya. Optimal design of responsive structures. *Structural and Multidisciplinary Optimization*, 65, 03 2022.

[3] L. T. Akerson, A. Mechanics, Modeling, and Shape Optimization of Electrostatic Zipper Actuators. *In Preparation*, 2023.

[4] C. P. Ambulo, M. J. Ford, K. Searles, C. Majidi, and T. H. Ware. 4d-printable liquid metal–liquid crystal elastomer composites. *ACS Applied Materials & Interfaces*, 13(11):12805–12813, 2021.

[5] J. M. Ball. Convexity conditions and existence theorems in nonlinear elasticity. *Archive for Rational Mechanics and Analysis*, 63:337–403, 1976.

[6] W. Bangerth, R. Hartmann, and G. Kanschat. Deal.II - -A general-purpose object-oriented finite element library. *ACM Transactions on Mathematical Software*, 33(4):1–27, 2007.

[7] M. Bendsøe and O. Sigmund. *Topology Optimization: Theory, Methods and Applications*. Springer, 2nd edition, 2003.

[8] M. P. Bendsøe. Optimal shape design as a material distribution problem. *Structural Optimization*, 1(4):193–202, 1989.

[9] K. Bhattacharya. *Microstructure of Martensite*. University of Minnesota, 1991.

[10] K. Bhattacharya and R. D. James. The material is the machine. *Science*, 307(5706):53–54, 2005.

[11] P. Cesana and A. DeSimone. Quasiconvex envelopes of energies for nematic elastomers in the small strain regime and applications. *Journal of the Mechanics and Physics of Solids*, 59(4):787–803, 2011.

[12] P. G. Ciarlet. *The Finite Element Method for Elliptic Problems*. Society for Industrial and Applied Mathematics, 2002.

[13] B. Dacorogna. *Direct Methods in the Calculus of Variations*. Applied Mathematical Sciences. Springer Berlin Heidelberg, 1989.

[14] G. Dal Maso. *An introduction to* Γ*-convergence*, volume 8. Springer Science & Business Media, 2012.

[15] M. de Luca and A. D. Simone. Mathematical and numerical modeling of liquid crystal elastomer phase transition and deformation. *MRS Online Proceedings Library*, 1403:37–42, 2012.

[16] A. Desimone and L. Teresi. Elastic energies for nematic elastomers. *The European physical journal. E, Soft matter*, 29:191–204, 07 2009.

[17] X. Gao, J. Yang, J. Wu, X. Xin, Z. Li, X. Yuan, X. Shen, and S. Dong. Piezoelectric actuators and motors: Materials, designs, and applications. *Advanced Materials Technologies*, 5, 1 2020.

[18] Q. He, Z. Wang, Y. Wang, A. Minori, M. T. Tolley, and S. Cai. Electrically controlled liquid crystal elastomer–based soft tubular actuator with multimodal actuation. *Science Advances*, 5(10):eaax5746, 2019.

[19] G. Kocak, C. Tuncer, and V. Bütün. ph-responsive polymers. *Polym. Chem.*, 8:144–176, 2017.

[20] A. Kotikian, R. L. Truby, J. W. Boley, T. J. White, and J. A. Lewis. 3d printing of liquid crystal elastomeric actuators with spatially programed nematic order. *Advanced Materials*, 30(10):1706164, 2018.

[21] Y. Li, H. Yu, K. Yu, X. Guo, and X. Wang. Reconfigurable three-dimensional mesotructures of spatially programmed liquid crystal elastomers and their ferromagnetic composites. *Advanced Functional Materials*, 31(23):2100338, 2021.

[22] S. Mohith, A. R. Upadhya, K. P. Navin, S. M. Kulkarni, and M. Rao. Recent trends in piezoelectric actuators for precision motion and their applications: a review. *Smart Materials and Structures*, 30, 1 2021.

[23] N. L. Pedersen. Topology optimization of laminated plates with prestress. *Computers and Structures*, 80(7-8):559–570, 2002.

[24] P. Penzler, M. Rumpf, and B. Wirth. A phase-field model for compliance shape optimization in nonlinear elasticity. *ESAIM: Control, Optimisation and Calculus of Variations*, 18(1):229–258, 2012.

[25] G. Rozvany and W. Prager. *Structural Design Via Optimality Criteria: The Prager Approach to Structural Optimization*. Mechanics of Elastic and Inela. Springer Netherlands, 1989.

[26] A. Talhan and S. Jeon. Pneumatic actuation in haptic-enabled medical simulators: A review. *IEEE Access*, 6:3184–3200, 12 2017.

[27] S. W. Ula, N. A. Traugutt, R. H. Volpe, R. R. Patel, K. Yu, and C. M. Yakacki. Liquid crystal elastomers: an introduction and review of emerging technologies. *Liquid Crystals Reviews*, 6:78–107, 2018.

[28] J. Walker, T. Zidek, C. Harbel, S. Yoon, F. S. Strickland, S. Kumar, and M. Shin. Soft robotics: A review of recent developments of pneumatic soft actuators. *Actuators*, 9, 3 2020.

[29] Z. Wang, Z. Wang, Y. Zheng, Q. He, Y. Wang, and S. Cai. Three-dimensional printing of functionally graded liquid crystal elastomer. *Science advances*, 6(39):eabc0034, 2020.

[30] T. H. Ware, M. E. McConney, J. J. Wie, V. P. Tondiglia, and T. J. White. Voxelated liquid crystal elastomers. *Science*, 347(6225):982–984, 2015.

[31] M. Warner and E. Terentjev. *Liquid Crystal Elastomers*. International Series of Monographs on Physics. OUP Oxford, 2007.

[32] T. White. *Photomechanical Materials, Composites, and Systems: Wireless Transduction of Light into Work*. 05 2017.

[33] Z. Zhao and X. S. Zhang. Topology optimization of hard-magnetic soft materials. *Journal of the Mechanics and Physics of Solids*, 158:104628, 2022.

Chapter 5

OPTIMAL STRUCTURES FOR FAILURE RESISTANCE UNDER IMPACT

A. Akerson, Optimal structures for failure resistance under impact, *Journal of Mechanics and Physics of Solids* 172 105172, 2023.

Abstract

The complex physics and numerous failure modes of structural impact creates challenges when designing for impact resistance. While simple geometries of layered material are conventional, advances in 3D printing and additive manufacturing techniques have now made tailored geometries or integrated multi-material structures achievable. Here, we apply gradient-based topology optimization to the design of such structures. We start by constructing a variational model of an elastic-plastic material enriched with gradient phase-field damage, and present a novel method to efficiently compute its transient dynamic time evolution. We consider a finite element discretization with explicit updates for the displacements. The damage field is solved through an augmented Lagrangian formulation, splitting the operator coupling between the nonlinearity and non-locality. Sensitivities over this trajectory are computed through the adjoint method, and we develop a numerical method to solve the resulting adjoint dynamical system. We demonstrate this formulation by studying the optimal design of 2D solid-void structures undergoing blast loading. Then, we explore the trade-offs between strength and toughness in the design of a spall-resistant structure composed of two materials of differing properties undergoing dynamic impact.

5.1 Introduction

The design of structures for impact or blast loading is encumbered by the complex interactions between wave propagation, plasticity, and material dam-

age. This leads to failure modes such as plugging, fracture, petaling, and spall which are highly dependent on the material parameters, loading conditions, and structural layout [4]. This is further complicated by the trade-offs between properties such as strength and toughness when designing integrated structures of multiple materials. In practice, engineers typically start with industry standards and intuition, followed by sophisticated dynamical simulations to iterate on a design before it undergoes physical testing. Usually, these designs consist of simple geometries of layered materials [23, 25, 20]. However, with recent advances in additive manufacturing and 3D printing, we may now look to tailored designs with complex geometries and integrated materials [40, 2, 18]. Additionally, the exponential growth of computational capabilities makes algorithmic optimal design methods feasible. This may allow us to efficiently design structures of unprecedented impact performance in scenarios where intuitive design is not sufficient.

Of the optimal structural design formulations, topology optimization has proven to be one of the most powerful methodologies. Density-based methods consider the density of material at each point in the domain as the unknown before the design is posed as an optimization problem over these densities. Then, gradient-based optimization methods are used to iteratively update the design, where sensitivities are usually computed through the adjoint method. Originally introduced to optimize the compliance of linear elastic structures [8], density-based topology optimization has since been applied to a wide range of applications including acoustic band-gaps [44], piezoelectric transducers [45], micro-electro-mechanical systems [37], energy conversion devices [14], and fluid structure interaction [51]. Another common method is level-set topology optimization. Here, the boundary of the structure is defined as a level set of a scalar-valued function, and optimization is performed over this function using the shape-gradient [1]. Finally, phase-field approaches remain popular as their variational form yields a favorable mathematical structure [10].

For the optimal design of impact problems, it is necessary to include transient dynamics, rate-dependent plasticity, and damage mechanics when modeling the material response. Past studies have addressed optimal design for transient dynamic evolution with elastic material models [43, 33]. Additionally, plasticity has been considered in both quasi-static [42, 49, 15, 48, 30] and dynamic settings [32, 22]. However, a structure with damage has only been considered

in the quasi-static case. This has been studied in both the ductile [26, 27] and quasi-brittle [16, 34, 6] regime to design damage resistant structures. A variational mechanics model, where solutions are computed through energy principles, are favored to accurately model the physics and provide mathematical structure. Furthermore, an efficient computational method for these fields is necessary, as the iterative design process requires repeatedly simulating the dynamics for updated designs.

To address the above mentioned requirements, we consider small-strain, rate-dependent plasticity enriched with continuum damage through a variational phase-field model in a transient dynamic setting. To efficiently simulate the dynamic response, we consider a finite element discretization where we employ an explicit update scheme for the displacement fields, and an implicit update for both the plasticity and damage. Because these irreversible damage updates are both nonlinear and non-local in nature, a direct computation would be prohibitively expensive. To this end, we use an operator-splitting augmented Lagrangian alternating direction method of multipliers. By introducing an auxiliary damage and Lagrange multiplier field, we accurately and efficiently solve for the damage updates by iterating between a nonlinear local problem, a linear global problem, and a Lagrange multiplier update.

We look to optimize the material placement of the structure over the dynamic trajectory for a given objective function. By assuming the material parameters are dependent on a continuous design variable, we derive sensitivities through the adjoint method. This results in an adjoint dynamical system that we solve in a manner which shares similarities to the forward problem numerics. We use a explicit update scheme for the adjoint displacement variable, and another augmented Lagrangian method for the adjoint damage variable. However, the adjoint problem is solved backwards in time, and the adjoint damage operator is linear rather than the nonlinear operator seen in the forward problem. With the adjoint solution, we compute the sensitivities and update the design.

We start in Section 5.2 by presenting the energy functional for system, then discuss the dynamic equilibrium relations. We apply the adjoint method, where sensitivities and adjoint relations are derived for a general objective. In Section 5.3 we detail the solution process. First, we apply an augmented Lagrangian to operator split the damage updates. Then, using a finite element discretization, we solve the system with explicit displacement updates,

followed by implicit plasticity and damage updates. We demonstrate the accuracy and efficiency of the numerical scheme by considering the solution convergence and time-scaling for a model problem. We use a similar numerical scheme for the adjoint system and the associated dual variables. Next, in Section 5.4, we discuss material interpolation schemes through intermediate densities for both solid-void structures and multi-material designs. In Section 5.5, we demonstrate the methodology by looking at two examples. First we consider the design of 2D solid-void structures optimized for blast loading. Next, we explore the trade-offs between strength and toughness in a two material spall-resistant structure undergoing impact. Finally, in Section 5.6, we summarize our findings and discuss further directions.

5.2 Theoretical Formulation

5.2.1 Forward Problem

We consider an elastic-plastic material capable of sustaining damage occupying a bounded, open domain $\Omega \subset \mathbb{R}^n$ in its reference configuration over time $[0, T]$. We assume prescribed loads on $\partial_f \Omega \subset \partial\Omega$ and prescribed displacements on $\partial_u \Omega \subset \partial\Omega$. We consider small-strain, rate-dependent J-2 plasticity with isotropic hardening to model the plasticity [35, 29]. Damage is measured by the phase-field scalar quantity $a : \Omega \times [0, T] \mapsto [0, 1]$, where values of 0 and 1 correspond to the undamaged and fully damaged states. Here, we use a phase-field fracture model which we adapt for damage by considering a finite length scale [11]. These models have been modified for ductile fracture by including small-strain plasticity [13], and we adopt a similar formulation. We assume the material parameters are dependent on a design field $\eta : \Omega \mapsto [0, 1]$ which determines the species of material at each point. We consider a variational structure, where minimization principles yields the internal variable evolution [36]. Thus, we consider the incremental energy

$$\begin{aligned}\mathcal{E}(u,q,\varepsilon^p,a,\eta) = \int_\Omega \Bigg\{ & W^e(\varepsilon,\varepsilon^p,a,\eta) \\ & + d(a)\left[W^p(q,\eta) + \int_0^t g^*(\dot{q},\eta)\,dt\right] \\ & + \frac{G_c(\eta)}{4c_w}\left[\frac{w^a(a,\eta)}{\ell(\eta)} + \ell(\eta)\|\nabla a\|^2\right] \\ & + \int_0^t \psi^*(\dot{a},\eta)dt\Bigg\} d\Omega,\end{aligned} \tag{5.1}$$

where $u : \Omega \times [0,T] \mapsto \mathbb{R}^n$ is the displacement field, $\varepsilon^p : \Omega \times [0,T] \mapsto \mathbb{R}^{n\times n}$ is the volume preserving plastic strain, and $q : \Omega \times [0,T] \mapsto \mathbb{R}^+$ is the accumulated plastic strain whose evolution is defined by

$$\dot{q} = \sqrt{\frac{2}{3}\dot{\varepsilon}^p \cdot \dot{\varepsilon}^p}. \tag{5.2}$$

W^e is the stored elastic energy density, which accounts for the tension-compression asymmetry in its damage dependence [3],

$$W^e(\varepsilon,\varepsilon^p,a,\eta) = \frac{K(\eta)}{2}\,\mathrm{tr}^-(\varepsilon^e)^2 + d(a)\left[\frac{K(\eta)}{2}\,\mathrm{tr}^+(\varepsilon^e)^2 + \mu(\eta)\varepsilon^e_D : \varepsilon^e_D\right], \tag{5.3}$$

where K and μ are the bulk and shear moduli. $d(a)$ models the weakening of the material with damage,

$$d(a) = (1-a)^2 + d_1 a^2, \tag{5.4}$$

where $d_1 << 1$. $\varepsilon^e = \varepsilon - \varepsilon^p$ is the elastic strain, and ε^e_D is its deviatoric component. $\mathrm{tr}^+(\varepsilon)$ and $\mathrm{tr}^-(\varepsilon)$ are the positive and negative parts of the strain trace,

$$\mathrm{tr}^+(\varepsilon) = \max(\mathrm{tr}(\varepsilon),0), \qquad \mathrm{tr}^-(\varepsilon) = \min(\mathrm{tr}(\varepsilon),0). \tag{5.5}$$

This decomposition of the volumetric strain allows for tension-compression asymmetry in the damage model; the tensile bulk modulus is affected by damage, while the compressive bulk modulus remains unaffected. W^p and w^a are the plastic and damage hardening functions, respectively. The damage parameters G_c and ℓ control the toughness and damage length scale, with c_w as a normalization constant. Finally, the rate dependence of both the damage and plastic hardening is handled by the dissipation potentials ψ^* and g^*, respectively. These functions also account for irreversibility, as they take a value of

$+\infty$ for negative rates,

$$g^*(\dot{q},\eta) = \begin{cases} \bar{g}^*(\dot{q},\eta) & \dot{q} \geq 0 \\ \infty & \dot{q} < 0 \end{cases}, \qquad \psi^*(\dot{a},\eta) = \begin{cases} \bar{\psi}^*(\dot{a},\eta) & \dot{a} \geq 0 \\ \infty & \dot{a} < 0 \end{cases}. \tag{5.6}$$

For the plastic potentials, we consider power-law hardening and rate-sensitivity functions

$$\begin{aligned} W^p(q,\eta) &= \sigma_y \left[q + \frac{n\varepsilon_0^p}{n+1} \left(\frac{q}{\varepsilon_0^p} \right)^{(n+1)/n} \right], \\ \bar{g}^*(\dot{q},\eta) &= \frac{m\sigma_y \dot{\varepsilon}_0^p}{m+1} \left(\frac{\dot{q}}{\dot{\varepsilon}_0^p} \right)^{(m+1)/m}. \end{aligned} \tag{5.7}$$

ε_0^p and $\dot{\varepsilon}_0^p$ are the reference plastic strain and strain rate and σ_y is the initial yield stress. n and m are the powers for the hardening and rate sensitivity, with the perfecty plastic and rate-indepdendent cases occurring as $n \to \infty+$ and $m \to \infty+$, respectively [35]. These plastic hardening and rate-hardening parameters may all depend on η. For the damage hardening, we consider a quadratic function

$$w^a(a,\eta) = w_1 a + (1 - w_1)a^2, \tag{5.8}$$

where $w_1 \in [0,1]$, which ensures $w^a(1) = 1$, and may be dependent on η. For simplicity, we consider the damage to be rate-independent by choosing $\bar{\psi}^*(\dot{a},\eta) = 0$. Here, we scale both the plastic potential and shear modulus with the same damage function $d(a)$. Thus, the yield strength and Mises stress have the same damage dependence, leading to damage independent plastic updates. A further discussion on the behavior of a similar material model can be found in [13]. However, this choice of constitutive is not essential, and the methodologies we present below remain general.

We consider dynamic evolution through the incremental action integral

$$\begin{aligned} \mathcal{L}(u,q,\varepsilon^p,a,\eta) = \int_{t_1}^{t_2} \Big\{ \mathcal{E}(u,q,\varepsilon^p,a,\eta) - \int_\Omega \frac{\rho(\eta)}{2} |\dot{u}|^2 d\Omega \\ - \int_\Omega f_b \cdot u \, d\Omega - \int_{\partial_f \Omega} f \cdot u \, dS \Big\} dt, \end{aligned} \tag{5.9}$$

where f_b and f are the body force and surface tractions, and ρ is the material density. Stationarity of this action integral gives the dynamic evolution and the kinetics of the internal variables [31]

$$0 = \int_\Omega \left[\rho \ddot{u} \cdot \delta u + \frac{\partial W^e}{\partial \varepsilon} \cdot \nabla \delta u - f_b \cdot \delta u \right] d\Omega$$
$$- \int_{\partial_f \Omega} f \cdot \delta u \, d\Omega \qquad \forall \delta u \in \mathcal{U}, \tag{5.10a}$$
$$0 \in \bar{\sigma}_M - \frac{\partial W^p}{\partial q} - \partial g^*, \qquad \text{on } \Omega, \tag{5.10b}$$
$$0 = \dot{\varepsilon^p} - \dot{q} M \qquad \text{on } \Omega, \tag{5.10c}$$
$$0 \in \frac{\partial W^e}{\partial a} + \frac{\partial d}{\partial a} \left(W^p + \int_0^t g^*(\dot{q}) \, dt \right)$$
$$- \nabla \cdot \left(\frac{G_c \ell}{2 c_w} \nabla a \right) + \frac{G_c}{4 c_w \ell} \frac{\partial w^a}{\partial a} + \partial \psi^* \qquad \text{on } \Omega, \tag{5.10d}$$
$$a = 0 \ \text{ on } \partial_u \Omega, \qquad \nabla a \cdot n = 0 \ \text{ on } \partial_f \Omega. \tag{5.10e}$$

Here, we assume quiescent initial conditions. $\mathcal{U}$ is the space of admissible displacement variations

$$\mathcal{U} = \{ u \in H^1(\Omega), \ u = 0 \text{ on } \partial_u \Omega \}. \tag{5.11}$$

(5.10a) is the second-order dynamic evolution of the displacement field. (5.10b) and (5.10c) are the yield relation and the evolution of the plastic strain, where $\bar{\sigma}_M$ is the normalized Mises stress (divided through by d(a)), and M is the direction of plastic flow. (5.10d) is the irreversible evolution of the damage field, with (5.10e) being the boundary conditions for a. The differential inclusion in the yield relation and damage equilibrium enforces the irreversibility of their respective internal variables. A further discussion on the damage evolution relation (5.10d) can be found in [28].

We briefly comment on the regularity of the solution to the forward problem. The plastic strains may be discontinuous in space, however, they remain continuous in time as the rate-dependence provides temporal regularity. The damage field, $a \in L^\infty((0,T); H^1(\Omega; \mathbb{R}^n))$, is continuous in space while being possibly discontinuous in time in the rate-independent case ($\bar{\psi}^*(\dot{a}, \eta) = 0$). Finally, the displacement field, $u \in H^1((0,T); H^1(\Omega; \mathbb{R}^n))$, is continuous in both space and time as the inertia provides temporal regularity.

5.2.2 Sensitivities and Adjoint Problem

We look to find the design field $\eta(x)$ such that an objective, dependent on the dynamic trajectory, is minimized. Thus, we consider a general objective of

integral form

$$\begin{aligned} \min_{\eta(x)} \quad & \mathcal{O}(\eta) := \int_0^T \int_\Omega o(u, q, \varepsilon^p, a, \eta)\, d\Omega\ dt \\ \text{subject to:} \quad & \text{Equillibrium relations in (5.10).} \end{aligned} \tag{5.12}$$

To conduct gradient-based optimization, the variation of the objective with η must be computed. For this, we employ the adjoint method [38]. We introduce fields ξ, γ, μ, and b as the dual variables to the displacement, plastic hardening, plastic strain, and the damage fields, respectively. We consider the necessary Kuhn-Tucker conditions for the irreversible equilibrium relations, and carry out the adjoint calculation. The full details of this can be found in 5.A. This gives the total variation of the objective as

$$\begin{aligned} \mathcal{O}_{,\eta}\delta\eta = \int_0^T \int_\Omega \Bigg\{ & \frac{\partial o}{\partial \eta} + \frac{\partial \rho}{\partial \eta}\ddot{u} \cdot \xi + \frac{\partial^2 W^e}{\partial \varepsilon \partial \eta} \cdot \nabla \xi \\ & + b\dot{a}\left(\frac{\partial^2 W^e}{\partial a \partial \eta} + \frac{\partial d}{\partial a}\frac{\partial W^p}{\partial \eta} + \frac{\partial d}{\partial a}\int_0^t \frac{\partial g^*}{\partial \eta} d\tau \right) \\ & + \frac{1}{2c_w}\frac{\partial (G_c \ell)}{\partial \eta}\nabla(b\dot{a}) \cdot \nabla a + b\dot{a}\left(\frac{w^{a\prime}}{4c_w}\frac{\partial (G_c/\ell)}{\partial \eta} + \frac{\partial^2 \psi^*}{\partial \dot{a} \partial \eta} \right) \\ & + \gamma\dot{q}\left(\frac{\partial \bar{\sigma}_M}{\partial \eta} - \frac{\partial \sigma_0}{\partial \eta} - \frac{\partial^2 g^*}{\partial \dot{q} \partial \eta} \right) \Bigg\}\, \delta\eta\, d\Omega\, dt, \end{aligned} \tag{5.13}$$

where the adjoint variables satisfy the dynamic evolution

$$
\begin{aligned}
0 = \int_\Omega \Bigg[& \Bigg(\nabla\xi \cdot \frac{\partial^2 W^e}{\partial\varepsilon\partial\varepsilon} + b\dot{a}\frac{\partial^2 W^e}{\partial a\partial\varepsilon} \\
& \quad + \gamma\dot{q}\frac{\partial\bar{\sigma}_M}{\partial\varepsilon} - \dot{q}\mu\cdot\frac{\partial M}{\partial\varepsilon}\Bigg)\cdot\nabla\delta_\eta u \\
& \quad + \rho\ddot{\xi}\cdot\delta_\eta u + \frac{\partial o}{\partial u}\cdot\delta_\eta u\Bigg]\, d\Omega \qquad \forall\delta_\eta u\in\mathcal{U}, \qquad (5.14a)
\end{aligned}
$$

$$
\begin{aligned}
& \frac{\mathrm{d}}{\mathrm{d}t}\Bigg[\gamma\left(\bar{\sigma}_M - \sigma_0 - \frac{\partial\bar{g}^*}{\partial\dot{q}}\right) - \gamma\dot{q}\frac{\partial^2\bar{g}^*}{\partial\dot{q}^2} \\
& \quad + \frac{\partial\bar{g}^*}{\partial\dot{q}}\left(\int_t^T b\dot{a}d'(a)d\tau\right) - \mu\cdot M\Bigg] \\
& \qquad = \frac{\partial o}{\partial q} + b\dot{a}d'(a)\frac{\partial W^p}{\partial q} - \gamma\dot{q}\frac{\partial\sigma_0}{\partial q} \qquad \text{on } \Omega, \qquad (5.14b)
\end{aligned}
$$

$$
\begin{aligned}
& \frac{\mathrm{d}\mu}{\mathrm{d}t} = \frac{\partial o}{\partial\varepsilon^p} + \nabla\xi\cdot\frac{\partial^2 W^e}{\partial\varepsilon\partial\varepsilon^p} + b\dot{a}\frac{\partial^2 W^e}{\partial a\partial\varepsilon^p} \\
& \quad + \gamma\dot{q}\frac{\partial\bar{\sigma}_M}{\partial\varepsilon^p} - \dot{q}\mu\cdot\frac{\partial M}{\partial\varepsilon^p} \qquad \text{on } \Omega, \qquad (5.14c)
\end{aligned}
$$

$$
\begin{aligned}
\frac{\mathrm{d}}{\mathrm{d}t}\left[D_a b + \frac{\partial^2\bar{\psi}^*}{\partial\dot{a}^2}b\dot{a}\right] &= \frac{\partial o}{\partial a} + \frac{\partial^2 W^e}{\partial a\partial\varepsilon}\cdot\nabla\xi \\
&\quad + b\dot{a}\left(\frac{\partial^2 W^e}{\partial a^2} + \frac{G_c}{4c_w\ell}\frac{\partial^2 w^a}{\partial a^2}\right) \\
&\quad + b\dot{a}d''\left(W^p + \int_0^t g^* d\tau\right) \\
&\quad - \nabla\cdot\left(\frac{G_c\ell}{2c_w}\nabla(b\dot{a})\right) \qquad \text{on } \Omega, \qquad (5.14d)
\end{aligned}
$$

$$
\xi|_{t=T} = 0, \quad \dot{\xi}|_{t=T} = 0,
$$

$$
\gamma|_{t=T} = 0, \quad \mu|_{t=T} = 0, \quad b|_{t=T} = 0,
$$

where

$$
D_a = \frac{\partial W^e}{\partial a} + \frac{\partial d}{\partial a}\left(W^p + \int_0^t g^*\, d\tau\right) - \nabla\cdot\left(\frac{G_c\ell}{2c_w}\nabla a\right) + \frac{G_c}{4\ell c_w}\frac{\partial w^a}{\partial a} + \frac{\partial\bar{\psi}^*}{\partial\dot{a}}. \quad (5.15)
$$

These are dependent on the forward problem solution and must be solved backwards in time. Once the forward problem is solved in time for $u(t), a(t), q(t)$, and $\varepsilon^p(t)$, they can be used to solve the adjoint problem backwards in time for $\xi(t), b(t), \gamma(t)$, and $\mu(t)$. The sensitivities can then be computed from (5.13). Details of the numerical methods to solve the forward and adjoint problem are discussed in the proceeding section.

It should be noted that both the adjoint problem and expression for the sensitivities may have issues with well-posedness. As we have used an elastic energy function which remains strongly convex, the Hessian which appears above is well defined. However, for a different choice of elastic energy this may not be the case. Furthermore, the convexity of the adjoint problem with respect to the entire variable set $\{\xi, \gamma, \mu, b\}$ is not established, which may lead to an ill-posed problem. While inertia is thought to provide some temporal regularity, the reader is nontheless cautioned in this regard. Additionally, issues may arise from the possible temporal discontinuities of the damage field discussed previously in Section 5.2.1. Thus, the $\dot{a}$ found in the adjoint relations may not be well-defined. A rigorous investigation into these matter would be quite worthwhile. However, after discretization we find that the presented formulation is sufficient in practice, perhaps providing the required regularity.

5.3 Numerics

5.3.1 Forward Problem

We discuss the details for the numerical evolution of the forward dynamics. First we introduce an augmented Lagrangian formulation to split the nonlinear and non-local operator coupling in the damage field equilibrium. Then, using a finite element discretization, we discuss the computational procedure for updating the displacements, plasticity and damage variables. Finally, we study the accuracy and efficiency of our formulation by studying the solution behavior for varying mesh sizes.

Augmented Lagrangian

The differential inclusion and gradient terms in the damage evolution of (5.10d) result in a nonlinear and non-local state equation for the damage updates. While there exist methods to directly solve these non-local constrained problems, they result in expensive computations that would be required at every timestep. Thus, we consider an augmented Lagrangian formulation to split this operator, and solve the system using an alternating direction method of multipliers (ADMM) [19, 17]. This method has been used to efficiently solve non-linear elasticity problems with internal variable evolution [52]. We introduce the auxiliary field $\alpha \in L^2(\Omega)$ and constrain $a = \alpha$ weakly for all time with the Lagrange multiplier $\lambda \in L^2(\Omega)$ and penalty factor r. Thus, we consider

the modified incremental energy

$$\begin{aligned}\mathcal{E} = \int_\Omega \Bigg\{ & W^e(\varepsilon, \varepsilon^p, \alpha, \eta) + d(\alpha) \left[W^p(q,\eta) + \int_0^t g^*(\dot{q},\eta)\, dt \right] \\ & + \frac{G_c(\eta)}{4c_w} \left[\frac{w^a(\alpha,\eta)}{\ell(\eta)} + \ell(\eta) \|\nabla a\|^2 \right] + \int_0^t \psi^*(\dot{\alpha},\eta) dt \\ & + \frac{r}{2}(a-\alpha)^2 + \lambda(a-\alpha) \Bigg\}\, d\Omega. \end{aligned} \tag{5.16}$$

Stationarity of the action integral using this augmented energy results in the equilibrium relations identical to that of (5.10), with the exception that (5.10d) be replaced by

$$\begin{aligned} & \lambda + r(a-\alpha) - \frac{\partial W^e}{\partial \alpha} - d'(\alpha) \left[W^p(q) + \int_0^t g^*(\dot{q})\, dt \right] \\ & - \frac{G_c}{4c_w \ell} \frac{\partial w^a}{\partial \alpha}(\alpha) \in \partial \psi^* (\dot{\alpha}) \qquad \text{on } \Omega, \end{aligned} \tag{5.17a}$$

$$0 = \int_\Omega \left[\frac{G_c \ell}{2c_w} \nabla a \cdot \nabla \delta a + r(a-\alpha)\delta a + \lambda \delta a \right] d\Omega \qquad \forall \delta a \in \mathcal{A}, \tag{5.17b}$$

$$0 = \int_\Omega (a-\alpha)\delta\lambda\, d\Omega \qquad \forall \delta\lambda \in L^2(\Omega), \tag{5.17c}$$

where

$$\mathcal{A} = \{ a \in H^1(\Omega),\ a = 0 \text{ on } \partial_u \Omega \}. \tag{5.18}$$

With α as the unknown, (5.17a) is a nonlinear local problem. Correspondingly, the second line (5.17b) is a linear global problem for a. The de-coupling of nonlinearity and non-locality allows for the efficient computation of the damage evolution, which we discuss with the numerical implementation.

Discretization and Solution Procedure

We discretize the system with standard $p = 1$ Lagrange finite elements for the displacement field u and the damage field a as

$$u = \sum_{i=1}^{n_u} u_i N_i^u(x), \qquad a = \sum_{i=1}^{n_a} a_i N_i^a(x), \tag{5.19}$$

where $N_i^u : \Omega \mapsto \mathbb{R}^n$ and $N_i^a : \Omega \mapsto \mathbb{R}$ are standard vector and scalar valued first-order shape functions with compact support. The fields α, q, and ε^p are discretized at quadrature points

$$\alpha(x_g) = \alpha_g, \qquad q(x_g) = q_g, \qquad \varepsilon^p(x_g) = \varepsilon^p_g, \tag{5.20}$$

for some Gauss point x_g. The Lagrange multiplier field λ is discretized in the same finite element space we use for a as

$$\lambda = \sum_{i=1}^{n_a} \lambda_i N_i^a(x). \tag{5.21}$$

Finally, the design field η is assumed constant on each element.

We start with an explicit central difference scheme to update the displacement field. Because the plasticity updates do not depend on the damage field, q and ε^p are next computed implicitly with a backwards Euler update. Finally, the damage field is updated implicitly by iterating between a nonlinear local problem for α by solving (5.17a), a linear global problem for a through (5.17b), and a Lagrange multiplier update for λ until convergence. Since the operator for the global problem remains identical between iterations, we need only construct the system matrix and perform the sparse LU decomposition once, where subsequent solves involve only a right-hand side assembly and back-substitution. For the n to $n+1$ time-step the displacement updates are

$$\begin{aligned} \ddot{u}_i^n &= M_{ij}^{-1} F_j^n(u^n, \varepsilon^{p,n}, \alpha^n, t^n), \\ \dot{u}_i^{n+1/2} &= \dot{u}_i^{n-1/2} + \Delta t^n \, \ddot{u}_i^n, \\ u_i^{n+1} &= u_i^n + \Delta t^{n+1/2} \, \dot{u}_i^{n+1/2}, \end{aligned} \tag{5.22}$$

where

$$\begin{aligned} M_{ij} &= \int_\Omega \rho(x) N_i^u \cdot N_i^u \, d\Omega, \\ F_j^n &= \int_\Omega \left[-\frac{\partial W^e}{\partial \varepsilon}(\varepsilon^n, \varepsilon^{p,n}, \alpha^n, \eta) \cdot \nabla N_j^u + f_b \cdot N_j^u \right] d\Omega \\ &\quad - \int_{\partial_f \Omega} f \cdot N_j^u \, d\Omega. \end{aligned} \tag{5.23}$$

In standard fashion, these integrals are approximated with Gauss quadrature. Again, since the plastic evolution does not depend on the damage field, we update the plasticity variables through an implicit backwards Euler discretization. For this, we employ a predictor-corrector scheme [35] to solve point-wise at each quadrature point,

$$\begin{aligned} &0 \in \bar{\sigma}_M(\varepsilon^{n+1}|_{x_g}, \varepsilon_g^{p,(n+1)}, \eta(x_g)) - \sigma_0(q_g^{n+1}, \eta(x_g)) - \partial g^* \left(\frac{q_g^{n+1} - q_g^n}{\Delta t}, \eta(x_g) \right), \\ &\varepsilon_g^{p,(n+1)} = \varepsilon_g^{p,n} + \Delta q M(\varepsilon_g^{n+1}, \varepsilon_g^{p,(n+1)}). \end{aligned} \tag{5.24}$$

The update for α uses an implicit backwards Euler method, coupled with ADMM for the fields a and λ. This reduces to iterations between a nonlinear

point-wise problem for the updates of α, a linear global problem for a, and an update for λ.

We summarize these operations for the n to $n+1$ time-step. Given u^{n+1}, q^{n+1}, $\varepsilon^{p,(n+1)}$, we initialize values $\tilde{\lambda}^0 = \lambda^n$, $\tilde{a}^0 = a^n$, and iterate over i:

- *Step 1: Non-linear local problem.* Update $\tilde{\alpha}^{i+1}$ by solving at each x_g

$$\begin{aligned} -\frac{\partial W^e}{\partial \alpha}&\left(\varepsilon^{n+1}|_{x_g}, \tilde{\alpha}_g^{i+1}, \eta(x_g)\right) \\ &- d'(\tilde{\alpha}_g^{i+1})\left[W^p(q_g^{n+1}, \eta(x_g)) + \int_0^t g^*(\dot{q}_g, \eta(x_g))\, dt\right] \\ &- \frac{G_c(\eta(x_g))}{4c_w \ell(\eta(x_g))}\frac{\partial w^a}{\partial \alpha}\left(\tilde{\alpha}_g^{i+1}, \eta(x_g)\right) \\ &+ \tilde{\lambda}^i|_{x_q} + r\left(\tilde{a}^i|_{x_g} - \tilde{\alpha}_g^{i+1}\right) \in \partial\psi^*\left(\frac{\tilde{\alpha}_q^{i+1} - \alpha_q^n}{\Delta t_n}, \eta(x_q)\right). \end{aligned} \tag{5.25}$$

- *Step 2: Linear global problem.* Update $\tilde{a}^{i+1}$ by solving

$$K_{pj}\, \tilde{a}_j^{i+1} = V_p(\tilde{\alpha}^{i+1}, \tilde{\lambda}^i), \tag{5.26}$$

where

$$\begin{aligned} K_{pq} &= \int_\Omega \left[\frac{G_c(\eta)\ell(\eta)}{2c_w}\nabla N_p^a \cdot \nabla N_q^a + r N_p^a N_q^a\right] d\Omega, \\ V_p(\alpha, \lambda) &= \int_\Omega (r\alpha - \lambda)\, N_p^a\, d\Omega. \end{aligned} \tag{5.27}$$

- *Step 3: Update Lagrange multiplier.* Update $\tilde{\lambda}^{i+1}$ by

$$\tilde{\lambda}_j^{i+1} = \tilde{\lambda}_j^i + r(\tilde{a}_j^{i+1} - S_{jk}^{-1}\hat{\alpha}_k^{i+1}), \tag{5.28}$$

where

$$S_{jk} = \int_\Omega N_j^a N_k^a\, d\Omega, \qquad \hat{\alpha}_k^{i+1} = \int_\Omega \tilde{\alpha}^{i+1} N_k^a\, d\Omega. \tag{5.29}$$

Note: this is the weak form of the update $\Delta\lambda = r(a - \alpha)$.

- *Step 4: Check for convergence.* Check both primal and dual feasibility

$$\begin{aligned} r_p &:= \left\|\bar{a}^{i+1} - \hat{\alpha}^{i+1}\right\|_{l^2} \le \frac{1}{\sqrt{n_a}} r_{abs}^{tol} + r_{rel}^{tol} \max\left(\left\|\hat{\alpha}^{i+1}\right\|_{l^2}, \left\|\bar{a}^{i+1}\right\|_{l^2}\right), \\ r_d &:= r\left\|\bar{a}^{i+1} - \bar{a}^i\right\|_{l^2} \le \frac{1}{\sqrt{n_a}} r_{abs}^{tol} + r_{rel}^{tol}\left\|\bar{\lambda}^{i+1}\right\|, \end{aligned} \tag{5.30}$$

where

$$\bar{a}_j^{i+1} = S_{jk}\tilde{a}_k^{i+1}, \qquad \bar{\lambda}_j^{i+1} = S_{jk}\tilde{\lambda}_j. \tag{5.31}$$

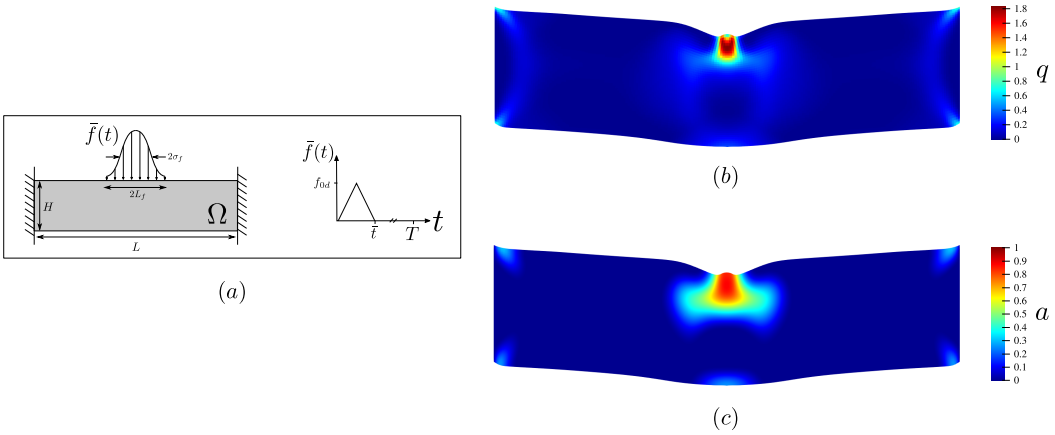

Figure 5.1: The model problem we use to study the accuracy and efficiency of our formulation. We consider a rectangular geometry with a impulse Gaussian loading profile (a). Additionally, deformed configurations with accumulated plasticity (b) and damage fields (c) are shown at the final time-step computed on a 200×50 mesh.

In the above, we use the vector l^2 norm

$$\|\bar{a}\|_{l^2}^2 = \sum_{i=1}^{n_a} \bar{a}_i^2. \tag{5.32}$$

until convergence, and update $\alpha^{n+1} = \tilde{\alpha}^i$, $a^{n+1} = \tilde{a}^i$, and $\lambda^{n+1} = \tilde{\lambda}^i$. For faster convergence, we update the penalty value r between iterations. As larger values of r improve primal feasibility convergence while slowing the dual feasibility convergence (and vice-versa), adapting the value of r based on these feasibility values can lead to few iterations [52, 12]. Thus, we consider the following scheme

$$r = \begin{cases} \min(\gamma_r r, r_{max}) & \text{if } r_p/r_d > \tau \\ \max(r/\gamma_r, r_{min}) & \text{if } r_d/r_p > \tau \\ r & \text{else} \end{cases}. \tag{5.33}$$

In our study, we choose $\tau = 10$, and take $\gamma_r = 2$.

Accuracy and Efficiency

To analyze the efficiency and efficacy of the above formulation, we study a model problem. We consider a clamped bar undergoing dynamic loading on its top surface, as shown in Figure 5.1a. The loading is chosen such that the

Parameter	Value Used	Description
Parameters for Accuracy and Scaling Tests		
H/L	0.25	Aspect ratio of domain
ν	0.3	Poisson ratio
σ_{y0}/E	1.0×10^{-2}	Yield strength
ε_0^p	0.13	Reference plastic strain
n	10	Isotropic hardening power
$\dot{\varepsilon}_0^p L/\sqrt{E/\rho}$	0.32	Reference plastic strain rate
m	6	Rate sensitivity power
ℓ/L	0.02	Damage length scale
$G_{c0}/(\ell E)$	1.5×10^{-2}	Toughness
d_1	0.01	Relative stiffness when fully damaged
w_1	0.95	Damage hardening parameter
f_{0d}/E	1.04×10^{-2}	Loading peak magnitude
L_f/L	0.1	Half width of Gaussian loading profile
σ_f/L	0.05	Standard Deviation of loading profile
$\bar{t}\sqrt{E/\rho}/L$	1.26	Duration of loading
$T\sqrt{E/\rho}/L$	11.3	Simulation time

Table 5.1: Non-dimensional geometric, loading, and material parameters used numerical accuracy and efficiency validation.

structure undergoes both plastic and damage evolution along its trajectory. Table 5.1 shows the geometric, loading, and material parameters used for this study. Figure 5.1b and 5.1c show the plasticity and damage fields at the final time. We investigate the solution convergence and time-scaling for uniform meshes varying from 60×15 to 600×150 for a constant 18,000 time-steps. Each of the simulations are run on 6 CPU cores using shared memory. The absolute and relative ADMM tolerance is set to a constant $r_{abs}^{tol} = r_{rel}^{tol} = 10^{-7}$.

To study the solution convergence, we consider the L^2 norm in time of the H^1 norm in space, which we denote as $|||\cdot||| := \| \left(\| \cdot \|_{H^1(\Omega)} \right) \|_{L^2(0,T)}$. We investigate $|||u|||$ for the varying meshes. As an analytical solution does not exist, we consider the solution on the 600×150 mesh as the reference, $\bar{u}$. Figure 5.2a shows the convergence of the displacement norm for varying characteristic mesh size h. A linear fit yields a convergence rate of 1.31, demonstrating

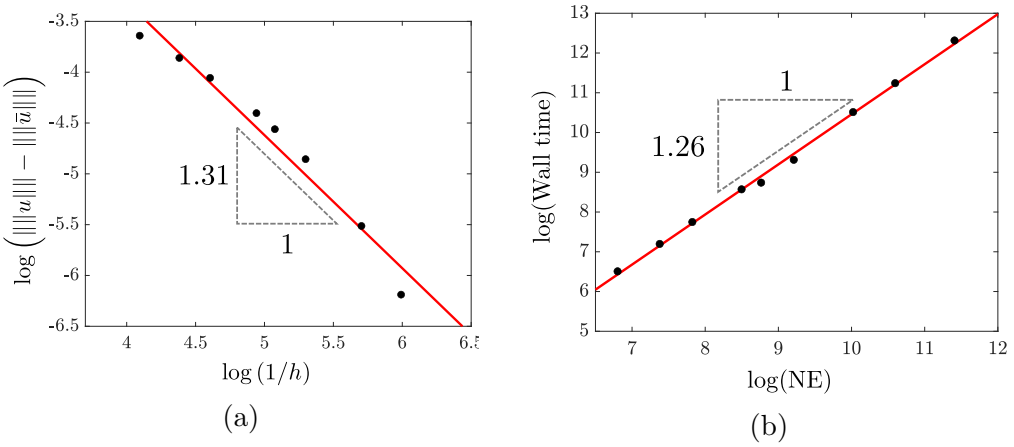

(a) (b)

Figure 5.2: Solution convergence and time-scaling plots for varying mesh sizes. The solution norm $|||u|||$ is studied relative to the characteristic mesh size h (a). For time-scaling, we consider the wall time v.s. the number of element, NE (b). The black dots represent data for each of the simulations, while the red lines show the linear fits, with the first order coefficients denoted on the triangles.

super-linear convergence even while undergoing large plastic and damage evolution. Next, we study the time-scaling for varying mesh sizes. For meshes varying from 900 to 90,000 elements, we see a growth rate with wall time of 1.26. This exceptional scaling may be attributed to the ADMM algorithm for computing the damage evolution. As the linear global problem has a constant operator for each penalty value r, these matrices may be pre-computed and treated with an LU decomposition in set-up. Then, each of the linear solves may be executed through efficient back-substitution. It is expected that this scaling breaks down if the number of elements increases significantly, as the solution time is then dominated by the more inefficient LU decomposition. Finally, 5.C presents a convergence study with respect to temporal resolution, and we see convergence in this regard as well.

5.3.2 Adjoint Problem

We now turn to the details of the numerical evolution of the adjoint problem, which must be solved backwards in time using the solution to the forward problem. For efficiency, we employ another augmented Lagrangian formulation for the adjoint damage variable update. Then, we discretize with finite elements and describe the solution procedure.

Augmented Lagrangian

The adjoint damage evolution for b in (5.14d) is challenging to efficiently solve. While the equation itself is linear, the $\dot{a}$ dependence makes the discretized operator dependent on the time-step. Therefore, we look to apply an augmented Lagrangian to cast this as a constant-operator global problem and a time-step dependent local problem. We introduce the auxillary field $z \in \mathcal{A}$, and constrain $z = \dot{a}b$ weakly through the Lagrange multiplier field $\chi \in L^2(\Omega)$. By writing the adjoint damage update as a minimization problem, we apply another augmented Lagrangian through the penalty parameter r (See 5.B). This gives the adjoint damage evolution as

$$0 = \int_\Omega \left[(r(z - \dot{a}b) + \chi)\, \delta z + \frac{G_c \ell}{2c_w} \nabla z \cdot \nabla \delta z \right] d\Omega \qquad \forall \delta z \in \mathcal{A}, \tag{5.34a}$$

$$\begin{aligned} \frac{\mathrm{d}}{\mathrm{d}t}\left[bD_a + \bar{\psi}^{*\prime\prime} \dot{a} b \right] = {} & \frac{\partial o}{\partial a} + \frac{\partial^2 W^e}{\partial a \partial \varepsilon} \cdot \nabla \xi \\ & + \dot{a} b \left(\frac{\partial^2 W^e}{\partial a^2} + \frac{G_c}{4\ell c_w} \frac{\partial^2 w^a}{\partial a^2} \right) \\ & + \dot{a} b d^{\prime\prime} \left[W^p + \int_0^t g^* d\tau \right] \\ & - r(z - \dot{a}b) - \chi \qquad \text{on } \Omega, \end{aligned} \tag{5.34b}$$

$$0 = \int_\Omega (z - \dot{a}b)\, \delta\chi \, d\Omega \qquad \forall \delta\chi \in L^2(\Omega). \tag{5.34c}$$

The first line (5.34a) is linear constant-operator global problem for z. (5.34b) is a linear local problem for b. Finally, the last line (5.34c) is the constraint that $z = \dot{a}b$ weakly. We discuss the iterative method of solving this in the next section.

Discretization and Solution Procedure

The adjoint variables are discretized in the same manner as their forward counterparts. The adjoint displacement field ξ, the adjoint damage field z, and adjoint Lagrange multiplier fields are then

$$\xi = \sum_{i=1}^{n_u} \xi_i N_i^u(x), \qquad z = \sum_{i=1}^{n_a} z_i N_i^a(x), \qquad \chi = \sum_{i=1}^{n_a} \chi_i N_i^a(x). \tag{5.35}$$

The fields b, γ, and μ are discretized at quadrature points:

$$b(x_g) = b_g, \qquad \gamma(x_g) = \gamma_g, \qquad \mu(x_g) = \mu_g, \tag{5.36}$$

for some Gauss point x_g. The adjoint problem must be solved backwards in time. Similar to the forward problem, we use an explicit central difference scheme for the adjoint displacement variable. Then, we implicitly update the adjoint damage variables through an alternating direction method of multipliers. After these converge, the adjoint plastic variables are updated implicitly. For the $n+1$ to the n time-step the displacement updates are

$$\begin{aligned} \ddot{\xi}_i^{n+1} &= M_{ij}^{-1} H_j^{n+1}(u^{n+1}, \varepsilon^{p,n+1}, \alpha^{n+1}, \xi^{n+1}, b^{n+1}, \gamma^{n+1}, \mu^{n+1}), \\ \dot{\xi}_i^{n+1/2} &= \dot{\xi}_i^{n+3/2} - \Delta t^{n+1}\, \ddot{\xi}_i^{n+1}, \\ \xi_i^{n} &= \xi_i^{n+1} - \Delta t^{n+1/2}\, \dot{\xi}_i^{n+1/2}, \end{aligned} \tag{5.37}$$

where

$$\begin{aligned} H_j^n = \int_\Omega \Bigg[\Bigg(& -\nabla \xi^n \cdot \frac{\partial^2 W^e}{\partial \varepsilon \partial \varepsilon} - \dot{\alpha}^n b^n \frac{\partial^2 W^e}{\partial \varepsilon \partial \alpha} \\ & -\gamma^n \dot{q}^n \frac{\partial \bar{\sigma}_M}{\partial \varepsilon} + \dot{q}^n \mu^n \cdot \frac{\partial M}{\partial \varepsilon} \Bigg) \cdot \nabla N_j^u - \frac{\partial o}{\partial u} \cdot N_j^u \Bigg] \, d\Omega. \end{aligned} \tag{5.38}$$

The update for b uses an implicit forward Euler method, coupled ADMM for fields z and χ. This results in iterations between a point-wise linear problem for b, a constant-matrix linear global problem for z, and an update for χ.

We describe this for the $n+1$ to n time-step. Given ξ^n, intialize $\tilde{\chi}^0 = \chi^{n+1}$, $\tilde{z}^0 = z^{n+1}$, and iterate over i:

- *Step 1: Linear local problem.* Update $\tilde{b}^{i+1}$ by solving at each x_g

$$\tilde{b}_g^{i+1} = \frac{\dot{\alpha}_g^{n+1} b_g^{n+1}\, \bar{\psi}^{*\prime\prime}\big|_{t_{n+1}} + b_g^{n+1} \tilde{D}_{a,g}^{n+1} + \Delta t \left(r\tilde{z}^i(x_g) + \tilde{\chi}^i(x_g) - \frac{\partial o}{\partial a}\big|_{t_n} - \frac{\partial^2 W^e}{\partial \alpha \partial \varepsilon}\Big|_{t_n} \cdot \nabla \xi^n \right)}{\dot{\alpha}_g^n\, \bar{\psi}^{*\prime\prime}\big|_{t_n} + \tilde{D}_{a,g}^n + \dot{\alpha}_g^n \left(\left[\frac{\partial^2 W^e}{\partial \alpha^2} + \frac{G_c}{4\ell c_w} \frac{\partial^2 w^a}{\partial a^2} \right]_{t_n} + d'' \left[W^p + \int_0^t g^* d\tau \right]_{t_n} + r \right)}, \tag{5.39}$$

  where

$$\begin{aligned} \tilde{D}_{a,g}^n = & \left[\frac{\partial W^e}{\partial \alpha} + \frac{G_c}{4\ell c_w} \frac{\partial w^a}{\partial \alpha} + \frac{\partial d}{\partial \alpha} \left(W^p + \int_0^t g^*\, d\tau \right) + \frac{\partial \bar{\psi}^*}{\partial \dot{\alpha}} \right]_{x_g, t_n} \\ & - r(a^n|_{x_g} - \alpha_g^n) - \lambda^n|_{x_g}. \end{aligned} \tag{5.40}$$

- *Step 2: Linear global problem.* Update $\tilde{z}^{i+1}$ by solving

$$K_{pj}\, \tilde{z}_j^{i+1} = U_p(\tilde{b}^{i+1}, \tilde{\chi}^i), \tag{5.41}$$

  where

$$U_p(b, \chi) = \int_\Omega (r\dot{\alpha}^n b - \chi)\, N_p^a \, d\Omega. \tag{5.42}$$

- *Step 3: Update Lagrange multiplier.* Update $\tilde{\chi}^{i+1}$ by

$$\tilde{\chi}_j^{i+1} = \tilde{\chi}_j^i + r(\tilde{z}_j^{i+1} - S_{jk}^{-1}\hat{z}_k^{i+1}), \tag{5.43}$$

where

$$\hat{z}_k^{i+1} = \int_\Omega \dot{\alpha}^n \tilde{b}^{i+1} N_k^a \, d\Omega. \tag{5.44}$$

Note: this is the weak form of the update $\Delta\chi = r(z - \dot{\alpha}b)$.

- *Step 4: Check for convergence.* Check both primal and dual feasibility,

$$\begin{aligned} r_p &:= \left\|\bar{z}^{i+1} - \hat{z}^{i+1}\right\|_{l^2} \leq \frac{1}{\sqrt{n_a}} r_{abs}^{tol} + r_{rel}^{tol} \max\left(\left\|\hat{z}^{i+1}\right\|_{l^2}, \left\|\bar{z}^{i+1}\right\|_{l^2}\right), \\ r_d &:= r\left\|\bar{z}^{i+1} - \bar{z}^i\right\|_{l^2} \leq \frac{1}{\sqrt{n_a}} r_{abs}^{tol} + r_{rel}^{tol}\left\|\bar{\chi}^{i+1}\right\|, \end{aligned} \tag{5.45}$$

where

$$\bar{z}_j^{i+1} = S_{jk}\tilde{z}_k^{i+1}, \qquad \bar{\chi}_j^{i+1} = S_{jk}\tilde{\chi}_k^{i+1}. \tag{5.46}$$

until convergence, and set $b^n = \tilde{b}^i$, $z^n = \tilde{z}^i$, and $\chi^n = \tilde{\chi}^i$. We adapt the penalty value r similarly to the forward problem in (5.33).

Finally, the adjoint plastic variables γ_g^n and μ_g^n are implicity updated by solving at each quadrature point:

$$\begin{aligned} &\left[\gamma\left(\bar{\sigma}_M - \sigma_0 - \frac{\partial \bar{g}^*}{\partial \dot{q}}\right) - \gamma\dot{q}\frac{\partial^2 \bar{g}^*}{\partial \dot{q}^2} + \frac{\partial \bar{g}^*}{\partial \dot{q}}\left(\int_t^T b\dot{\alpha}d'(\alpha)d\tau\right) - \mu \cdot M\right]_{\substack{t=t_{n+1} \\ x=x_g}} \\ &- \left[\gamma\left(\bar{\sigma}_M - \sigma_0 - \frac{\partial \bar{g}^*}{\partial \dot{q}}\right) - \gamma\dot{q}\frac{\partial^2 \bar{g}^*}{\partial \dot{q}^2} + \frac{\partial \bar{g}^*}{\partial \dot{q}}\left(\int_t^T b\dot{\alpha}d'(\alpha)d\tau\right) - \mu \cdot M\right]_{\substack{t=t_n \\ x=x_g}} \\ &\qquad = \Delta t\left(\left.\frac{\partial o}{\partial q}\right|_{\substack{t=t_n \\ x=x_g}} + b_g^n \dot{\alpha}_g^n d'(\alpha_g^n)\left.\frac{\partial W^p}{\partial q}\right|_{\substack{t=t_n \\ x=x_g}} - \gamma_g^n \dot{q}_g^n \left.\frac{\partial \sigma_0}{\partial q}\right|_{\substack{t=t_n \\ x=x_g}}\right), \\ \mu_g^{n+1} - \mu_g^n &= \Delta t\left(\left.\frac{\partial o}{\partial \varepsilon^p}\right|_{\substack{t=t_n \\ x=x_g}} + \nabla\xi^n \cdot \left.\frac{\partial^2 W^e}{\partial \varepsilon \partial \varepsilon^p}\right|_{\substack{t=t_n \\ x=x_g}}\right. \\ &\qquad + b_g^n \dot{\alpha}_g^n \left.\frac{\partial^2 W^e}{\partial \alpha \partial \varepsilon^p}\right|_{\substack{t=t_n \\ x=x_g}} + \gamma\dot{q}_g^n \left.\frac{\partial \bar{\sigma}_M}{\partial \varepsilon^p}\right|_{\substack{t=t_n \\ x=x_g}} \\ &\qquad \left. - \dot{q}_g^n \mu_g^n \cdot \left.\frac{\partial M}{\partial \varepsilon^p}\right|_{\substack{t=t_n \\ x=x_g}}\right). \end{aligned} \tag{5.47}$$

This is a linear system of equations which may be solved by direct inversion.

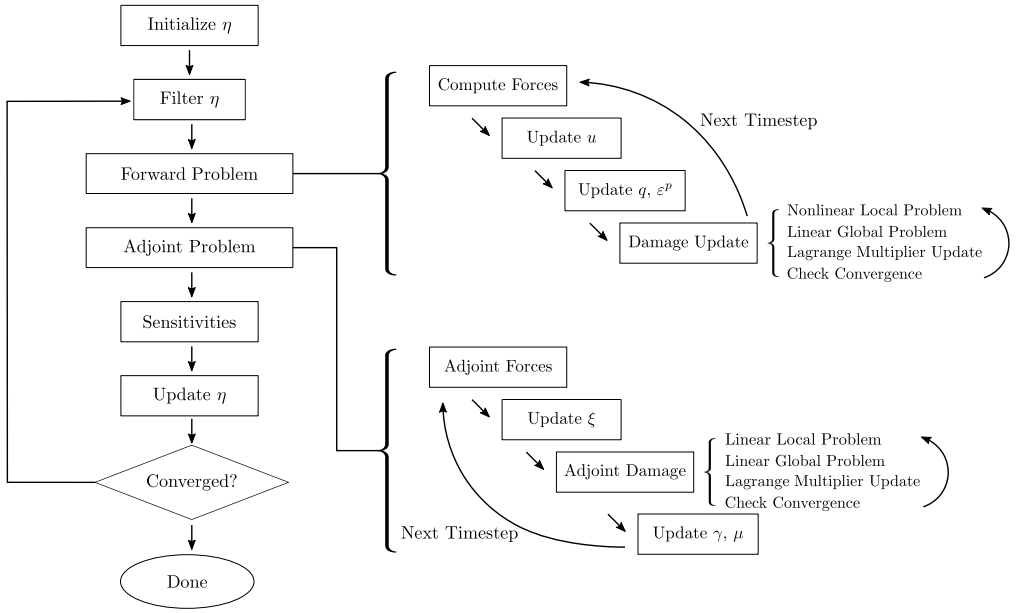

Figure 5.3: Diagram of the computational method for gradient-based topology optimization over the dynamic trajectory with plasticity and damage.

5.3.3 Sensitivities and Design Updates

Optimal design problems in structural mechanics often lead to ill-posed minimization problems, where minimizing sequences develop fine scale oscillations [24, 46]. To recover a well-posed problem, we filter the design variable η. These density-based filtering methods have been shown to lead to well-posed problems for linear, static compliance optimization. We consider η constant on each element, and adopt a discrete re-normalized filter with a linear weight function [9]. Sensitivities, accounting for the filtering, are then computed from (5.13). These are used to update η using the gradient-based method of moving asymptotes (MMA) [47]. This process is continued until convergence. Figure 5.3 shows a flow diagram of the entire computational process.

5.4 Material Interpolation

In the preceding section, we developed a computational method for evolving the forward and adjoint problem to compute sensitivities. However, we still must define how the material parameters depend on the design parameter η. That is, we must determine how the material density, elastic energy, plastic potential and dissipation, and also the damage parameters depend on η. In

this section, we discuss interpolation schemes for both solid-void designs, as well as designs composed of two materials of differing parameters.

The approach that we take implicitly penalizes intermediate densities, as is done by Solid Isotropic Material with Penalization (SIMP) methods used in static linear elastic compliance minimization [7]. Thus, we interpolate the material properties for intermediate densities while maintaining desired properties of each of the full material species. However, as there are multiple material parameters, rather than just the elastic modulus of SIMP, this leads to a complicated procedure which we describe below. Additionally, as SIMP in the linear elastic setting is specialized for compliance minimization, our method is specialized for failure resistance. Other objective functions would require a different interpolation scheme, as to render the intermediate densities unfavorable. Finally, sharp interface methods do not require interpolation [50]. However, the behavior of the full material species which we present would still be valid, and other issues might arise when computing the shape derivative.

5.4.1 Solid-Void Designs

We consider η as differentiating between void at $\eta = \eta_{min} << 1$ and solid at $\eta = 1$. Usually $\eta_{min} \approx 0.01$. Similar to traditional topology optimization, we would like to penalize intermediate densities so converged designs are dominated by regions of completely solid or void. In the following, the subscript 0 denotes parameters for the completely solid material. We propose the following interpolation scheme:

Material density We consider η a density variable, and assume the material density varies linearly:

$$\rho(\eta) = \eta\rho_0. \tag{5.48}$$

Elastic Energy For simplicity, we consider a separable dependence for the elastic energy through a Bezier curve interpolation. This ensures that the ratio of stiffness to density does not go to zero in the limit of small η. This mitigates spurious dynamical modes which could arise from artificial acoustic properties of the voids [7]. We consider

$$W^e(\varepsilon, \varepsilon^p, a, \eta) = B_e(\eta)W_0^e(\varepsilon, \varepsilon^p, a), \tag{5.49}$$

where W_0^e is the elastic energy of the solid and $B_e(\eta)$ is defined through

$$\begin{aligned} \eta &= \frac{1-k_2}{k_1-k_2}(3v-3v^2)+v^3, \\ B_e &= k_1\frac{1-k_2}{k_1-k_2}(3v-3v^2)+v^3. \end{aligned} \tag{5.50}$$

Given η, the top equation may be solved for v, which is then used to compute B_e in the second equation. k_1 and k_2 are the derivative values $\frac{dB}{d\eta}$ at $\eta = 0$ and $\eta = 1$, respectively. Typical values for these slopes are $k_1 \approx 0.2$, $k_2 \approx 5$.

Plastic potentials For the plastic potentials, we will again consider a separable dependence

$$W^p(q,\eta) = B_p(\eta)W_0^p(q), \qquad g^*(\dot{q},\eta) = B_p(\eta)g_0^*(\dot{q}). \tag{5.51}$$

However, care must be taken in choosing $B_p(\eta)$, as we require this interpolation to satisfy certain properties:

- *Strong voids* : The yield stress should be sufficiently high as to reduce excessive permanent deformation in the void regions. Additionally, we do not want to waste computational effort on plastic updates in the voids. This requires
$$1 < \frac{B_p(\eta_{min})}{B_e(\eta_{min})}. \tag{5.52}$$
- *Unfavorable intermediate densities* : The interpolation of the plastic potential should ensure that the relative yield stress is not excessively high in regions of intermediate density, so optimal solutions are dominated by regions of either completely solid or void. This requires
$$\frac{B_p(\eta)}{B_e(\eta)} < \tau_p \quad \forall \eta \in [\eta_1, \eta_2], \tag{5.53}$$
where $\eta_{min} < \eta_1 < \eta_2 < 1$ and $\tau_p \sim 1$.

We may accomplish both of these by considering a shifted Bezier curve interpolation as

$$B_p(\eta) = \frac{B_e(\eta)+\delta_p}{1+\delta_p}, \tag{5.54}$$

where $B_e(\eta_{min}) < \delta_p << 1$.

Damage parameters We now discuss the interpolation for the damage behavior. For simplicity, we assume that the normalized damage potential $w^a(a)$ is independent of the density. The damage length scale will also be considered constant with density

$$\ell(\eta) = \ell_0. \tag{5.55}$$

This allows the same computational mesh to resolve damage in both the solid and void regions. Then, we must only prescribe the interpolation on the toughness G_c. We assume a separable dependency

$$G_c(\eta) = B_a(\eta) G_{c0}, \tag{5.56}$$

where the interpolation function B_a must satisfy the following:

- *Boundary condition preservation* : The behavior at the solid-void interface should be nearly equivalent to the natural boundary conditions. This ensures that the voids behave similarly to free boundaries and do not add artificial toughness. This requires

$$B_a(\eta_{min}) << B_a(1). \tag{5.57}$$

- *Tough voids*: We require that the damage not propagate through the void regions, which could result in damage "jumping" from one solid region to another by moving through voids. This requires

$$1 < \frac{B_p(\eta_{min})}{B_e(\eta_{min})} << \frac{B_a(\eta_{min})}{B_e(\eta_{min})}, \tag{5.58}$$

  ensuring that the relative toughness of the voids is much larger than that of the solid.

- *Unfavorable intermediate densities* : The damage interpolation should ensure that the relative toughness is not excessively high in regions of intermediate density, so optimal solutions are dominated by regions of either completely solid or void. This requires

$$\frac{B_a(\eta)}{B_e(\eta)} < \tau_a \quad \forall \eta \in [\eta_1, \eta_2], \tag{5.59}$$

  where $\eta_{min} < \eta_1 < \eta_2 < 1$ and $\tau_a \sim 1$.

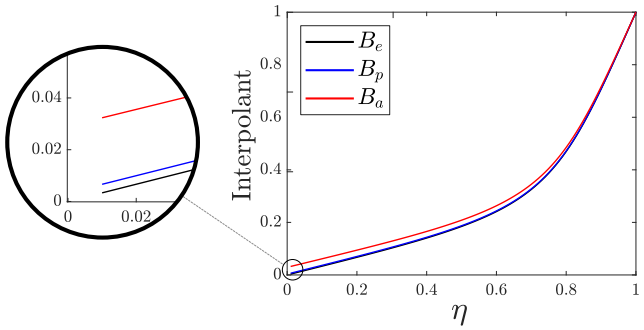

Figure 5.4: Plot of the interpolation functions for the elasticity (B_e), plasticity (B_p), and damage (B_a) for parameters $k_1 = 0.2$, $k_2 = 5.0$, $\delta_p = k_1\eta_{min}$, and $\delta_a = 9k_1\eta_{min}$. Here, $\eta_{min} = 0.01$.

We may again accomplish these through a shifted Bezier curve,

$$B_a(\eta) = \frac{B_e(\eta) + \delta_a}{1 + \delta_a}, \tag{5.60}$$

where $B_e(\eta_{min}) << \delta_p < \delta_a << 1$.

For our investigation, we choose a value of $\delta_p = k_1\eta_{min}$, $\delta_a = 9k_1\eta_{min}$. Thus, the yield strain of the void regions is roughly twice that of the solid. Additionally, the voids have around 10 times the relative toughness of the solid regions. Figure 5.4 shows these interpolation functions plotted for typical values.

5.4.2 Two-Material Design

We now consider designs composed of two materials, where $\eta = 0$ and $\eta = 1$ represents solids of either species. We propose to interpolate the majority of these parameters through standard power-law functions. These penalize regions of intermediate densities, while also being efficient and simple to implement. We discuss this further in Section 5.5.2 where we consider a specific example.

5.5 Examples

We now demonstrate the methodology using two examples which are of independent interest for the insights they offer on damage resistant structures. The first is a solid-void design to resist impulse loading. The second example explores the trade-offs between strength and toughness in a spall-resistant structure composed of two different materials undergoing dynamic impact. The

forward dynamics, adjoint problem, sensitivity calculation, and MMA update schemes are implemented using the deal.II C++ finite element library [5].

5.5.1 ***Solid-Void for Blast Loading***

We consider η as a density variable distinguishing between solid material and void. To model blast loading, we assume a fixed loading prescribed on the boundary. Thus, we consider a rectangular 2D geometry and impulse loading as shown in Figure 5.5. We look to minimize a sum of the time-space norm of the displacements, plastic dissipation, and damage dissipation

$$\mathcal{O} = \frac{\sigma_{y0} L}{T^{1/s}} \| \left(\|u\|_{H^1(\Omega)} \right) \|_{L^s(0,T)} + c_p \mathcal{D}^p + c_a \mathcal{D}^a, \tag{5.61}$$

where c_p and c_a are weights, and $\mathcal{D}^p$ and $\mathcal{D}^a$ are measures of the dissipated energy to plasticity and damage,

$$\begin{aligned} \mathcal{D}^p &= \int_\Omega d(a(T)) \left(\tilde{W}^p \Big|_{t=T} + \int_0^T \tilde{g}^* \, dt \right) \, d\Omega, \\ \mathcal{D}^a &= \int_\Omega \left[\frac{\tilde{G}_c w^a(a(T))}{4 c_w \ell} + \int_0^T \tilde{\psi}^* \, dt \right] \, d\Omega. \end{aligned} \tag{5.62}$$

We use a modified interpolation scheme in the objective to penalize intermediate densities. That is, we choose $\tilde{W}^p$, $\tilde{g}^*$, $\tilde{G}_c$, and $\tilde{\psi}^*$ to remain relatively large for intermediate η. Thus, we consider a concave power-law interpolation

$$\begin{aligned} \tilde{W}^p(q,\eta) &= P(\eta) W_0^p(q), \qquad & g^*(\dot{q},\eta) &= P(\eta) g_0^*(q), \\ \tilde{G}_c(\eta) &= P(\eta) G_{c0}, & \psi^*(\dot{q},\eta) &= P(\eta) \psi_0^*(q), \end{aligned} \tag{5.63}$$

where

$$P(\eta) = 1 - (1-\eta)^{p_O}. \tag{5.64}$$

Here, p_O is a growth factor parameter. s is the power for the norm in time. Because we intend to minimize the largest displacements, we choose $s = 4$ for the following studies. Additionally, we choose a value of $p_O = 8$.

We consider material parameters shown in Table 5.2. We also show material parameters for Al2014-T6, which were approximated from [39] where applicable, to demonstrate that we are indeed studying a realistic regime. We consider a Gaussian loading profile of standard deviation $\sigma_f = L/20$, truncated to a total width of $2L_f = L/5$. We use objective penalty values of $c_p = 5,\ c_a = 50$. Thus, we look to heavily penalize damage. For the interpolation parameters,

Parameter	Value Used	AL2014-T6	Description
Geometric and Material Parameters			
H/L	0.25	N/A	Aspect ratio of domain
ν	0.3	0.33	Poisson ratio
σ_{y0}/E	1.0×10^{-2}	0.71×10^{-2}	Yield strength
ε_0^p	0.13	0.7	Reference plastic strain
n	10	1.48	Isotropic hardening power
$\dot{\varepsilon}_0^p L/\sqrt{E/\rho}$	0.32	0.33	Reference plastic strain rate
m	6	3.3	Rate sensitivity power
ℓ/L	0.02	N/A	Damage length scale
$G_{c0}/(\ell E)$	1.5×10^{-2}	0.61×10^{-2}	Toughness
d_1	0.01	N/A	Relative stiffness fully damaged
w_1	0.95	N/A	Damage hardening parameter

Table 5.2: Non-dimensional geometric and material parameters used for the solid-void structures. Where applicable, approximate values for a Al2014-T6 specimen of length $L = 1$m are included to illustrate the typical value ranges (taken from Deformation behaviours of Al2014-T6 at different strain rates and temperatures, Prakash et al., *Structures* 2020.

we linearly update the Bezier slopes from $k_1 = 0.5$, $k_2 = 2.0$ to $k_1 = 0.125$, $k_2 = 8$ from the first to the 50th iteration. This allows the structure topology to more free change at lower iterations before intermediate densities are severely penalized, and is standard practice in topology optimization [7]. Because the structure may not be able to withstand the loading (without severe damage) for the early iterations, we begin with a lower loading amplitude before gradually increasing to the final desired value. We set the loading amplitude to be 70% of the final value until iteration 60, which we then linearly increase to the final value by iteration 100. Computations are performed on a 100×25 mesh, with a density filter radius of $0.021L$. Additionally, we restrict the amount of material used to be no more than half the volume of Ω. Designs are then initialized to uniform density fields equal to the total allowed volume fraction $\eta = 0.5$. We consider designs converged when the maximum change in density variable is less than 10^{-3}, or after 300 iterations.

We explore optimal designs for varying applied impulse magnitude $I = \int_0^T \int_{\partial_f \Omega} |f| \, d\Omega dt$, and loading duration $\bar{t}$. Here, we consider a reference

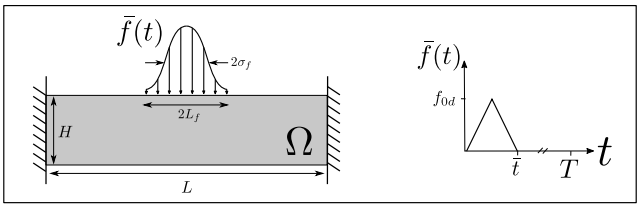

Figure 5.5: Geometry and dynamic impulse loading we consider for the solid-void structure.

loading duration $t_0 = 1.47\ L/c_L$, $c_L = \sqrt{E/\rho}$, roughly the time that it takes a longitudinal wave to traverse three half-length of the domain. For the reference impulse, we consider $I_0 = 6.3 \times 10^{-4}\ L^2\sqrt{E\rho}$. The simulation time is set to $T = 19t_0$ with 4000 timesteps. Figure 5.6 shows the converged design after contour smoothing in MATLAB®. This smoothing is performed by tracing contours along the filtered density function on the finite element mesh at a level-set value 0.5. Along each row, the loading impulse is constant, while along each columns the loading duration is constant. Although the structures share similar supports near the boundaries, their topologies near the loading site vary drastically. We see that for that for longer loading duration (right column), the structure is similar to what we would expect from static compliance optimization: truss-like members forming triangular structures [7]. However, for shorter loading duration, the structures have more mass congregated underneath the applied load. This not only provides damage resistance, but the additional inertia also reduces the energy the structure absorbs from the impulse loading. We also see more mass placed near the loading surface for large impulse magnitude. This is likely to reduce plasticity and damage near the loading site.

5.5.2 ***Two Material Design for Impact***

We now consider the design of a structure composed of two materials undergoing impact. Figure 5.7a shows the stress-strain response of the two materials in a quasi-static tensile simulation. While one material has double the strength and stiffness (red curve), the other has roughly twice the toughness (blue curve). We represent the strong solid with $\eta = 1$, and the tough solid with $\eta = 0$. Thus, we consider,

$$E_1 < E_2, \quad (\sigma_{y0})_1 < (\sigma_{y0})_2\,, \quad (G_c)_1 > (G_c)_2\,, \tag{5.65}$$

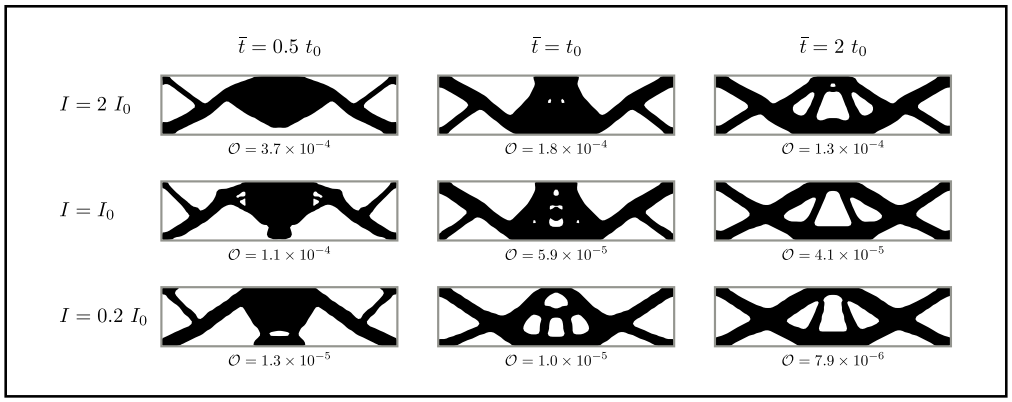

Figure 5.6: Converged solid-void designs under impulse loading following contour smoothing. Along each row, the impulse is constant, while along the columns we vary the loading duration. Values of the objective are shown for each of the designs. All of the designs saturated the constraint that $V \leq 0.5|\Omega|$.

where E, G_c, and σ_{y0} denotes the elastic modulus, fracture toughness, and yield stress. The subscripts 1 and 2 denotes properties of the tough and strong solid, respectively. For simplicity, we assume the rest of the material properties are identical (density, hardening parameters, damage length scale). As discussed in the previous section, we adopt a power-law interpolation for material parameters. However, to ensure that the intermediate η remains unfavorable, we must carefully choose the concavity of each of the interpolation functions. Since it is assumed that a larger value for each of the differing parameters is favorable, the interpolation is convex for all of these:

$$\begin{aligned} E(\eta) &= E_1 + \eta^p (E_2 - E_1), \\ \sigma_{y0}(\eta) &= (\sigma_{y0})_1 + \eta^p \left[(\sigma_{y0})_2 - (\sigma_{y0})_1 \right], \\ G_c(\eta) &= (G_c)_2 + (1-\eta)^p \left[(G_c)_1 - (G_c)_2 \right]. \end{aligned} \tag{5.66}$$

Similarly to the solid-void structure, we start with a penalty value of $p = 2$, and linearly increase it to $p = 8$ by the 100th iteration and onward.

We consider the geometry as Figure 5.7b. Here, we consider a linear elastic flyer of density ρ_0 and elastic modulus E_0 with an initial velocity of v_0. We note that enforcing strict contact conditions would complicate the adjoint sensitivity calculations, and also be computationally expense. Therefore, we consider a relaxation by introducing a layer of asymmetric linear elastic elements between the domain Ω and the flyer. These elements have a high bulk modulus in compression, with nearly zero resistance to shear or hydrostatic

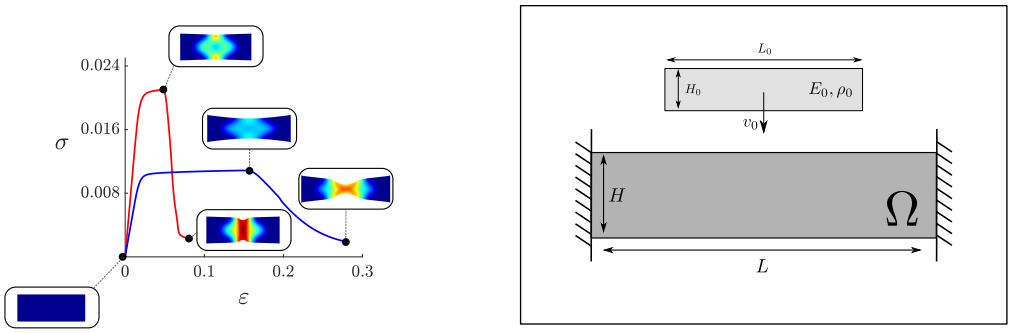

(a) (b)

Figure 5.7: (a) Normalized stress-strain response of the strong (red) and tough (blue) material in a uniaxial quasi-static 2D tensile test. Damage fields are plotted on deformed configurations at a few points throughout loading. (b) Geometry and loading for the two-material structure.

tension. Therefore, they may support compressive contact forces, while allowing the flyer and substrate to separate. This is consistent with the adjoint formulation we have derived, while providing the necessary physics of contact and separation. However, we are limited to cases where the impact site is known *a priori* and the impacting faces are parallel. While this regularization will give proper behavior of the traveling elastic waves far from the impact site, the loads nearby will be somewhat reduced. This is an acceptable compromise, as we are mainly interested in the spall phenomena occuring near the center of the structure, as well as hinging at the boundaries. But it should be noted that the behavior near the impact site may be inconsistent with true impact.

First, we consider the optimal design of the multi-material structure undergoing a relatively high impact velocity of $0.110c_L$, where c_L is the longitudinal wave speed of the strong material. Here, we consider a simulation time of $T = 6.5\ L/c_L$. In this case, a structure composed entirely of strong material experiences heavy damage, as shown in Figure 5.8a. The damage nucleates internally along a line parallel to the impact surface, which is characteristic of spall failure. Conversely, a structure made of only the tough material has large permanent deformation. There is regions of plasticity near the impact site as well as hinging near the boundary, as shown in Figure 5.8b. We apply the optimal design approach to this loading scenario, as we hypothesize that a mixture of both strong and tough material will yield a structure of better performance. We consider the objective shown in (5.61). Since η does not have

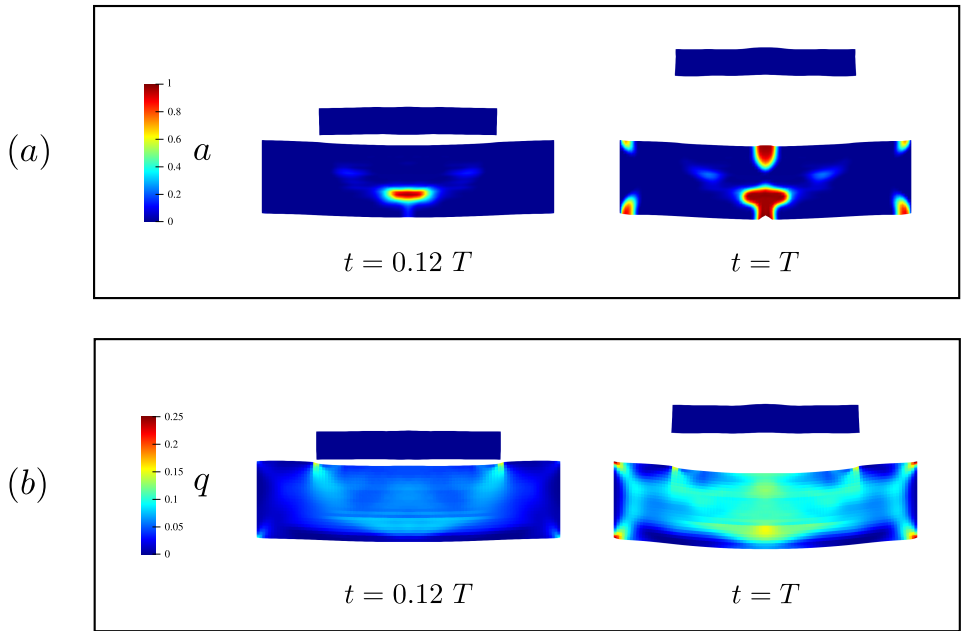

Figure 5.8: (a) Damage field of a domain composed entirely of the strong material shortly after impact (left), and long after impact (right). (b) Accumulated plasticity field of a domain composed entirely of the tough material shortly after impact (left), and long after impact (right).

a large effect on the dissipation functions, we do not need to modify the interpolation scheme in the objective as was done in the solid-void case. Table 5.3 shows the material parameters we consider. Computations are performed on a 100×25 mesh for the rectangular domain, with a 60×16 mesh for the flyer. A filter radius of $0.021L$ is used. Again, we use objective weights of $c_p = 5$, $c_a = 50$. The design is initialized to a uniform density field of $\eta = 0.5$. The converged optimal design is shown in Figure 5.7a. Red regions are occupied by strong material, and blue regions by the tough material. We see regions of strong (red) material near the boundaries and the impact site to mitigate large deformations and provide strength. However, the center is occupied by tough (blue) material to control spall. In terms of quantified performance, the converged design yields an objective value of $\mathcal{O} = 10.6 \times 10^{-4}$. This is improved performance over both the completely strong structure ($\mathcal{O} = 29.7 \times 10^{-4}$), and the completely tough structure ($\mathcal{O} = 11.3 \times 10^{-4}$).

Next, we study optimal designs for varying flyer velocity and allowed volume of strong material, V_s. We again consider the objective in (5.61). Figure 5.10 shows the converged designs. For lower impact velocities, the strong material

Parameter	Value	Description
Geometric Parameters		
H/L	0.25	Aspect ratio of domain
L_0/L	0.6	Length of flyer
H_0/L	0.1	Height of flyer
Elastic Material Parameters		
E_1/E_2	0.5	Young's modulus ratio tough to strong
ν	0.3	Poisson ratio of strong and tough material
E_0/E_2	0.3	Young's modulus ratio of flyer to strong
ν_0	0.4	Poisson ratio of flyer
ρ_0/ρ	0.4	Density ratio of flyer to target
Plastic Material Parameters		
$(\sigma_{y0})_1/E_2$	0.5×10^{-2}	Yield strength of tough material
$(\sigma_{y0})_2/E_2$	1.0×10^{-2}	Yield strength of strong material
ε_0^p	0.22	Reference plastic strain
n	3	Isotropic hardening power
$\dot{\varepsilon}_0^p L/\sqrt{E_2/\rho}$	0.22	Reference plastic strain rate
m	3	Rate sensitivity power
Damage Material Parameters		
$(G_{c0})_1/(\ell E_2)$	1.0×10^{-2}	Toughness of tough material
$(G_{c0})_2/(\ell E_2)$	0.5×10^{-2}	Toughness of strong material
ℓ/L	0.01	Damage length scale
d_1	0.01	Relative stiffness when fully damaged
w_1	0.95	Damage hardening parameter

Table 5.3: Non-dimensional geometric and material parameters for the multi-material structures.

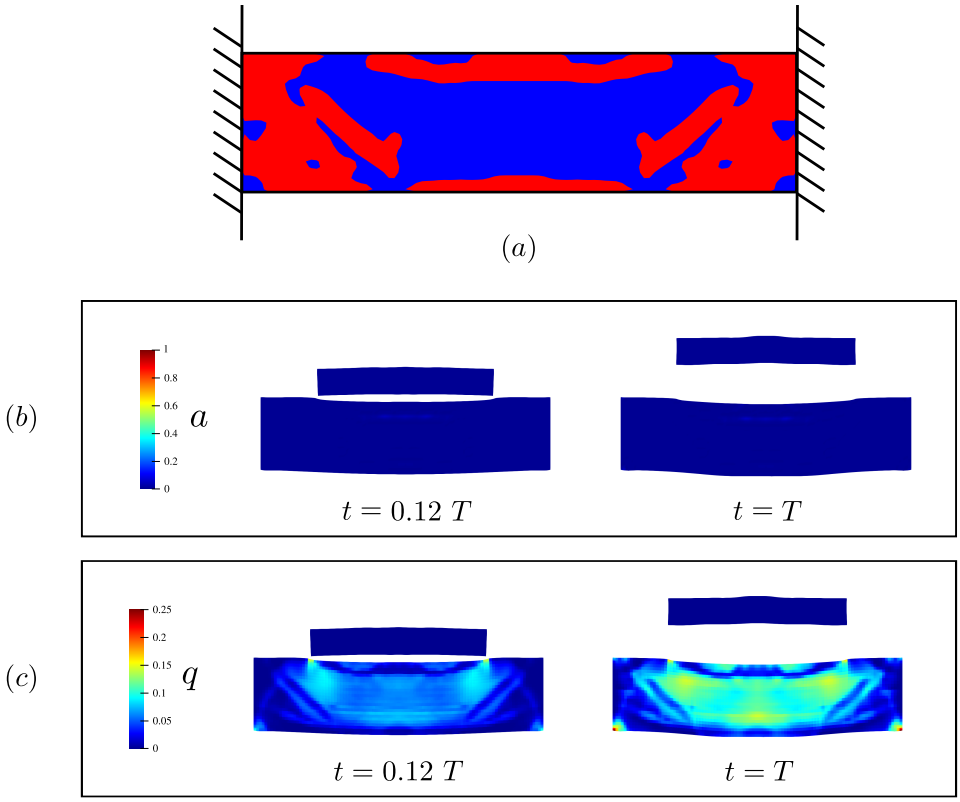

Figure 5.9: (a) Optimal design of the multi-material structure under impact loading following contour smoothing. The red regions correspond to the strong material, and the blue regions are the tough material. (b) Damage field of this design shortly after impact (left), and long after impact (right). (c) Accumulated plasticity field of this design shortly after impact (left), and long after impact (right).

is favored. In cases where no restrictions put on the design, the converged designs are almost completely occupied by strong material. This can primarily be attributed to the stiffness difference between the strong and tough material. At $v_0 = 0.019c_L$, there is almost no plasticity or damage, while at $v_0 = 0.058c_L$ there is only a small amount of plasticity. However, at $v_0 = 0.110c_L$, the converged designs have large areas of tough material, even in the case when there is no restriction placed on the amount of strong material. As discussed previously, this is to control spall which occurs at the higher impact velocities. Additionally, strong material is used at the larger two velocities on the top surface underneath the sides of the flyer. This is to mitigate the shear-dominated plugging failure.

Finally, we study optimal designs for varying yield strength and toughness

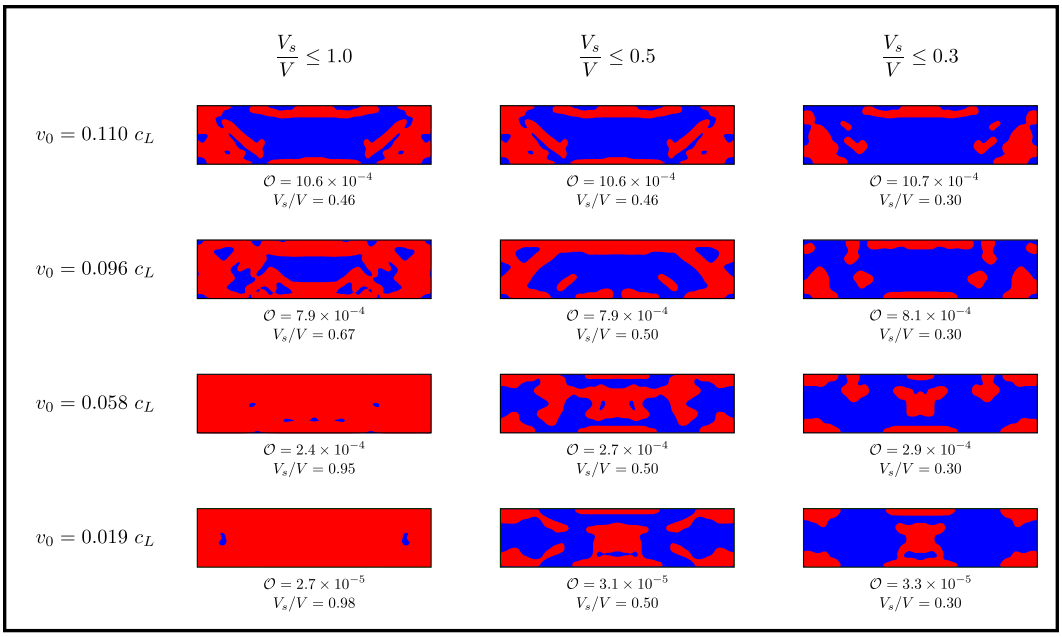

Figure 5.10: Converged multi-material designs for impact resistance following contour smoothing. Along each row the impact velocity is constant, while along the columns the allowed amount of strong material is prescribed. c_L denotes the longitudinal wave speed of the strong material. The red regions denote the strong material, while the blue regions are the tough material. Values of the objective as well as the volume fraction of strong material are shown for each design.

values. Figure 5.11 shows converged designs for a constant impact velocity of $v_0 = 0.096 c_L$. We constrain $V_s \leq 0.5$. The material parameters we use are identical to that of the previous study, with the following exceptions. Moving from the right to left column, the yield strength of the strong material is amplified by 50% from the previous study, while moving from the top row to the bottom row has an increased toughness of the tough material by 50%. While the designs do vary, qualitatively they all have strong material placed near the loading site attached to struts that connect to the boundary to provide stiffness.

5.6 Discussion and Conclusion

We have developed a formulation for the optimal design of impact resistant structures. After presenting a novel method to accurately and efficiently simulating phase field damage and plasticity evolution in a transient dynamic

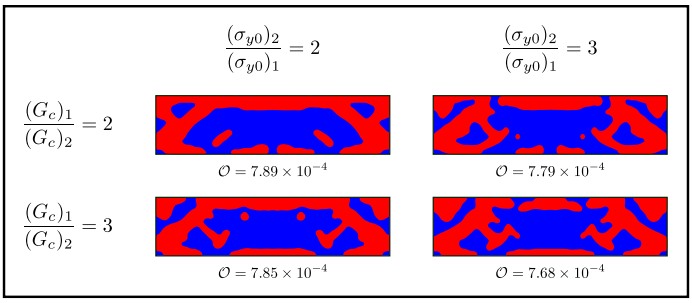

Figure 5.11: Converged multi-material designs for impact resistance following contour smoothing. Here, we consider a constant impact velocity of $v_0 = 0.096c_L$ and restrict $V_2/V \leq 0.5$. Along each row, the the toughness of both material are held constant, while along the columns we prescribe the yield strengths. The red regions denote the strong material, while the blue regions are the tough material. Values of the objective are shown for each design. In all of the cases, the designs saturate the constraint on allowed amount of strong material.

setting, we apply gradient based optimization through the adjoint method to find optimal structures. An important issue we address is the proper interpolation scheme for material parameters through intermediate densities. In the case of solid-void design, our formulation ensures that damage will not propagate through the void regions while preserving the natural boundary conditions at the interface. For the multi-material design, we assumed a power law interpolation for the material parameters. This implicitly penalizes intermediate densities only when either higher or lower values are clearly favorable. These would include elastic stiffness, yield stress, and fracture toughness, where higher values are almost universally preferred. For parameters such as the damage length scale, it is unclear if a higher or lower value is favorable. However, in our study, we only consider cases where these parameters are identical for both materials.

We demonstrate these capabilities through the design of both a solid-void structure for blast loading, and a multi-material structure undergoing impact. We find that the optimal designs for the solid-void case are highly dependent on loading magnitude and duration. For the short time-scale loading, inertia plays a large role in minimizing the energy transferred to the structure. This leads to a complex trade-off between inertia and support, all while mitigating material failure. As for the multi-material structures, optimal designs use a mixture of strong and tough material when the impact velocity is high. The

propagation and interaction between stress waves leads to a balance of strength and toughness throughout different parts of the domain.

We now discuss possible extensions and their challenges. As detailed in Section 5.2.2, there remain issues with regularity in the adjoint and sensitivity calculation. A rigorous investigation into this matter would be needed to give a deep understanding of the underlying mathematics of these methodologies. Another avenue would be to reformulate this work for a sharp interface topology optimization method [50]. This would eliminate the need for such a complex interpolation scheme, however, issues may arise from shape-derivative computation. Additionally, a systematic study comparing density based methods to sharp-interface methods in the case of a complex mechanics model would be quite beneficial to the community.

On the modeling side, we have chosen a small-strain elastic-plastic material model. While we have used a particular form for this plasticity and damage constitutive, the procedure of both the forward solution and optimization scheme remain general. Thus, it would be would be worthwhile and straightforward to apply this methodology to explore other models, such as a finite plasticity, and compare the results. These methods could also be easily applied to a local damage description. In such a case, there would be no need to for the operator-splitting method we have used, leading to a more efficient and straightforward calculation. Furthermore, the adjoint problem would also have a local description for the adjoint damage updates. However, these local damage models often suffer from ill-posed mathematical structures, relying heavily on ad-hoc update schemes. The methods presented would necessarily be reduced to such a setting. Additionally, we have simplified the contact mechanics by using asymmetric elastic elements, while also neglecting friction and adhesion. These would be necessary to model ballistic events. It would be beneficial to incorporate frictional contact through efficient active set methods to preserve the computational scaling [21]. Of course, the sensitivity and adjoint formulation would need to be modified to account for this complication. Thermal effects and shock physics would be another key modeling addition. Currently, empirically derived models exist for a variety of materials which could be incorporated into this framework [41].

It would also be interesting to explore other objective functionals. One might be interested in designing energy-absorbing structures that are designed to

undergo plasticity and damage, rather than the objective which we chose to mitigate these. However, this would require a reformulation of the interpolation scheme. We also note that the designs we obtain depend on the location of the load. It would be straightforward to extend this work to consider multiple loading scenarios, and optimize the structure over the collective response. Finally, our simulations were done in 2D, and were readily performed on a single machine with shared memory. It would be natural to extend the implementation to a 3D settings, requiring distributed memory parallelization.

Acknowledgements

The author would like to acknowledge Kaushik Bhattacharya for his advice and support throughout the project.

The financial support of the U.S. National Science Foundation through "Collaborative Research: Optimal Design of Responsive Materials and Structures" (DMS:2009289) and the US Army Research Laboratory through Cooperative Agreement Number W911NF-122-0022 is gratefully acknowledged. The views and conclusions contained in this document are those of the authors and should not be interpreted as representing the official policies, either expressed or implied, of the Army Research Laboratory or the U.S. Government. The U.S. Government is authorized to reproduce and distribute reprints for Government purposes notwithstanding any copyright notation herein.

BIBLIOGRAPHY

[1] G. Allaire, F. De Gournay, F. Jouve, and A. M. Toader. Structural optimization using topological and shape sensitivity via a level set method. *Control and Cybernetics*, 34(1):59–81, 2005.

[2] A. Ambrosi, R. D. Webster, and M. Pumera. Electrochemically driven multi-material 3D-printing. *Applied Materials Today*, 18:100530, 2020.

[3] H. Amor, J. J. Marigo, and C. Maurini. Regularized formulation of the variational brittle fracture with unilateral contact: Numerical experiments. *Journal of the Mechanics and Physics of Solids*, 57(8):1209–1229, 2009.

[4] M. E. Backman and W. Goldsmith. The mechanics of penetration of projectiles into targets. *International Journal of Engineering Science*, 16(1):1–99, 1978.

[5] W. Bangerth, R. Hartmann, and G. Kanschat. Deal.II - -A general-purpose object-oriented finite element library. *ACM Transactions on Mathematical Software*, 33(4):1–27, 2007.

[6] T. Barbier, E. Shakour, O. Sigmund, G. Lombaert, and M. Schevenels. Topology optimization of damage-resistant structures with a predefined load-bearing capacity. *International Journal for Numerical Methods in Engineering*, 123(4):1114–1145, 2022.

[7] M. Bendsøe and O. Sigmund. *Topology optimization. Theory, methods, and applications. 2nd ed., corrected printing.* Springer, Berlin, Heidelberg, 2004.

[8] M. P. Bendsøe. Optimal shape design as a material distribution problem. *Structural Optimization*, 1(4):193–202, 1989.

[9] B. Bourdin. Filters in topology optimization. *International Journal for Numerical Methods in Engineering*, 50(9):2143–2158, 2001.

[10] B. Bourdin and A. Chambolle. Design-dependent loads in topology optimization. *ESAIM: COCV*, 9(January):19–48, 2003.

[11] B. Bourdin, G. A. Francfort, and J. J. Marigo. Numerical experiments in revisited brittle fracture. *Journal of the Mechanics and Physics of Solids*, 48(4):797–826, 2000.

[12] S. Boyd, N. Parikh, E. Chu, B. Peleato, and J. Eckstein. Distributed optimization and statistical learning via the alternating direction method of multipliers. *Foundations and Trends in Machine Learning*, 3(1):1–122, 2010.

[13] S. Brach, E. Tanné, B. Bourdin, and K. Bhattacharya. Phase-field study of crack nucleation and propagation in elastic–perfectly plastic bodies. *Computer Methods in Applied Mechanics and Engineering*, 353:44–65, 2019.

[14] L. Collins and K. Bhattacharya. Optimal design of a model energy conversion device. *Structural and Multidisciplinary Optimization*, 59(2):389–401, 2019.

[15] D. Cox, N. Reid, P. Tauzowski, B. Blachowski, J. Lógó, S. Hüeber, B. I. Wohlmuth, M. Afrousheh, J. Marzbanrad, and D. Göhlich. Topology optimization of energy absorbers under crashworthiness using modified hybrid cellular automata (MHCA) algorithm. *Structural and Multidisciplinary Optimization*, 60(3):1021–1034, 2019.

[16] J. Desai, G. Allaire, and F. Jouve. Topology optimization of structures undergoing brittle fracture. *Journal of Computational Physics*, 458, 2022.

[17] M. Fortin and R. Glowinski. Augmented Lagrangian methods : applications to the numerical solution of boundary-value problems. 1983.

[18] B. Gadagi and R. Lekurwale. A review on advances in 3D metal printing. *Materials Today: Proceedings*, 45:277–283, 2020.

[19] R. Glowinski and P. L. Tallec. *Augmented Lagrangian and Operator Splitting Methods in Nonlinear Mechanics*. Studies in Applied Mathematics. Society for Industrial and Applied Mathematics, 1989.

[20] X. Huang, W. Zhang, Y. Deng, and X. Jiang. Experimental investigation on the ballistic resistance of polymer-aluminum laminated plates. *International Journal of Impact Engineering*, 113(December 2017):212–221, 2018.

[21] S. Hüeber and B. I. Wohlmuth. A primal-dual active set strategy for non-linear multibody contact problems. *Computer Methods in Applied Mechanics and Engineering*, 194(27-29):3147–3166, 2005.

[22] N. Ivarsson, M. Wallin, and D. Tortorelli. Topology optimization of finite strain viscoplastic systems under transient loads. *International Journal for Numerical Methods in Engineering*, 114(13):1351–1367, 2018.

[23] P. K. Jena, K. Ramanjeneyulu, K. Siva Kumar, and T. Balakrishna Bhat. Ballistic studies on layered structures. *Materials and Design*, 30(6):1922–1929, 2009.

[24] R. V. Kohn and G. Strang. Optimal design and relaxation of variational problems, i. *Communications on Pure and Applied Mathematics*, 39(1):113–137, 1986.

[25] H. Li, Z. Li, Z. Xiao, X. Wang, J. Xiong, J. Zhou, and Z. Guan. Development of an integrated model for prediction of impact and vibration response of hybrid fiber metal laminates with a viscoelastic layer. *International Journal of Mechanical Sciences*, 197(January), 2021.

[26] L. Li, G. Zhang, and K. Khandelwal. Topology optimization of energy absorbing structures with maximum damage constraint. *International Journal for Numerical Methods in Engineering*, 112(7):737–775, 2017.

[27] L. Li, G. Zhang, and K. Khandelwal. Failure resistant topology optimization of structures using nonlocal elastoplastic-damage model. *Structural and Multidisciplinary Optimization*, 58(4):1589–1618, 2018.

[28] E. Lorentz and V. Godard. Gradient damage models: Toward full-scale computations. *Computer Methods in Applied Mechanics and Engineering*, 200(21-22):1927–1944, 2011.

[29] J. Lubliner. *Plasticity Theory*. Dover books on engineering. Dover Publications, 2008.

[30] F. Maury, Aymeric and Allaire, Grégoire and Jouve. Elasto-plastic Shape Optimization Using the Level Set Method. *SIAM Journal on Control and Optimization*, 56(1):556–581, 2018.

[31] A. Mielke. Chapter 6 Evolution Of Rate-Independent Systems. *Handbook of Differential Equations: Evolutionary Equations*, 2(January):461–559, 2005.

[32] P. B. Nakshatrala and D. A. Tortorelli. Topology optimization for effective energy propagation in rate-independent elastoplastic material systems. *Computer Methods in Applied Mechanics and Engineering*, 295:305–326, 2015.

[33] P. B. Nakshatrala and D. A. Tortorelli. Nonlinear structural design using multiscale topology optimization. Part II: Transient formulation. *Computer Methods in Applied Mechanics and Engineering*, 304:605–618, 2016.

[34] L. Noël, P. Duysinx, and K. Maute. Level set topology optimization considering damage. *Structural and Multidisciplinary Optimization*, 56(4):737–753, 2017.

[35] M. Ortiz and J. B. Martin. Symmetry-preserving return mapping algorithms and incrementally extremal paths: A unification of concepts. *International Journal for Numerical Methods in Engineering*, 28(8):1839–1853, 1989.

[36] M. Ortiz and L. Stainier. The variational formulation of viscoplastic constitutive updates. *Computer Methods in Applied Mechanics and Engineering*, 171(3-4):419–444, 1999.

[37] N. L. Pedersen. Topology optimization of laminated plates with prestress. *Computers and Structures*, 80(7-8):559–570, 2002.

[38] R. E. Plessix. A review of the adjoint-state method for computing the gradient of a functional with geophysical applications. *Geophysical Journal International*, 167(2):495–503, 2006.

[39] G. Prakash, N. K. Singh, and N. K. Gupta. Deformation behaviours of Al2014-T6 at different strain rates and temperatures. *Structures*, 26(March):193–203, 2020.

[40] M. Rafiee, R. D. Farahani, and D. Therriault. Multi-Material 3D and 4D Printing: A Survey. *Advanced Science*, 7(12):1–26, 2020.

[41] S. Ravindran, V. Gandhi, Z. Lovinger, M. Mello, and G. Ravichandran. Dynamic Strength of Copper at High Pressures Using Pressure Shear Plate Experiments. *Journal of Dynamic Behavior of Materials*, 7(2):248–261, 2021.

[42] S. Schwarz and E. Ramm. Sensitivity analysis and optimization for non-linear structural response. *Engineering Computations (Swansea, Wales)*, 18(3-4):610–641, 2001.

[43] V. Shobeiri. Bidirectional evolutionary structural optimization for nonlinear structures under dynamic loads. *International Journal for Numerical Methods in Engineering*, 121(5):888–903, 2020.

[44] O. Sigmund and J. S. Jensen. Systematic design of phononic band-gap materials and structures by topology optimization. *Philosophical Transactions of the Royal Society A: Mathematical, Physical and Engineering Sciences*, 361(1806):1001–1019, 2003.

[45] E. C. N. Silva and N. Kikuchi. Design of piezoelectric transducers using topology optimization. *Smart Materials and Structures*, 8(3):350–364, 1999.

[46] G. Strang and R. V. Kohn. Optimal design in elasticity and plasticity. *International Journal for Numerical Methods in Engineering*, 22(1):183–188, 1986.

[47] K. Svanberg. The method of moving asymptotes - a new method for structural optimization. *International Journal for Numerical Methods in Engineering.*, 24(October 1985):359–373, 1987.

[48] P. Tauzowski, B. Blachowski, and J. Lógó. Functor-oriented topology optimization of elasto-plastic structures. *Advances in Engineering Software*, 135(October 2018):102690, 2019.

[49] M. Wallin, V. Jönsson, and E. Wingren. Topology optimization based on finite strain plasticity. *Structural and Multidisciplinary Optimization*, 54(4):783–793, 2016.

[50] M. Y. Wang, X. Wang, and D. Guo. A level set method for structural topology optimization. *Computer Methods in Applied Mechanics and Engineering*, 192(1):227–246, 2003.

[51] G. H. Yoon. Topology optimization for stationary fluid–structure interaction problems using a new monolithic formulation. *International Journal for Numerical Methods in Engineering*, 82(5):591–616, 2010.

[52] H. Zhou and K. Bhattacharya. Accelerated computational micromechanics and its application to polydomain liquid crystal elastomers. *Journal of the Mechanics and Physics of Solids*, 153:104470, 2021.

APPENDIX TO CHAPTER 5

5.A Adjoint Method for Sensitivities

We consider an objective of integral from

$$\mathcal{O}(u, q, \varepsilon^p, a, \eta) = \int_0^T \int_\Omega o(u, q, \varepsilon^p, a, \eta)\, d\Omega. \tag{5.67}$$

To conduct gradient based optimization, we require the total variation of this objective with the field $\eta(x)$, which we will compute through the adjoint method. We consider adjoint fields $\xi \in \mathcal{U}$, $\gamma : \Omega \mapsto \mathbb{R}$, $\mu : \Omega \mapsto \mathbb{R}^{n\times n}$, and $b : \Omega \mapsto \mathbb{R}$ which correspond to the displacement, plastic hardening, plastic strain, and the damage field, respectively. As is standard for the adjoint method, we consider these fields as the variations in their corresponding equilibrium relations, which we add to the objective. However, for the ir-reversible damage and platicity evolution, we use the necessary Kuhn-Tucker conditions. The augmented objective is

$$\begin{aligned}\mathcal{O} = \int_0^T \int_\Omega \Bigg\{ & o + \rho\ddot{u}\cdot\xi + \frac{\partial W^e}{\partial \varepsilon}\cdot\nabla\xi - f_b\cdot\xi + \gamma\dot{q}\left[\sigma_M - \sigma_0 - \frac{\partial \bar{g}^*}{\partial \dot{q}}\right] \\ & + \mu\cdot(\dot{\varepsilon}^p - \dot{q}M) + b\dot{a}\left[\frac{\partial W^e}{\partial a} + d'\left(W^p + \int_0^t \bar{g}^* d\tau\right)\right. \\ & \left. -\nabla\cdot\left(\frac{G_c\ell}{2c_w}\nabla a\right) + \frac{G_c}{4c_w\ell}\frac{\partial w^a}{\partial a} + \frac{\partial \bar{\psi}^*}{\partial \dot{a}}\right] \Bigg\} d\Omega dt \\ & + \int_0^T \int_{\partial\Omega} (f\cdot\xi)\; dS\, dt.\end{aligned} \tag{5.68}$$

We then take variations with η.

$$\begin{aligned}
\mathcal{O}_{,\eta}\delta\eta = \int_0^T \int_\Omega \Bigg\{ & \frac{\partial o}{\partial \eta} + \frac{\partial \rho}{\partial \eta}\ddot{u}\cdot\xi + \frac{\partial^2 W^e}{\partial \varepsilon \partial \eta}\cdot\nabla\xi + b\dot{a}\left(\frac{\partial^2 W^e}{\partial a \partial \eta} + \frac{\partial d}{\partial a}\frac{\partial W^p}{\partial \eta} + \frac{\partial d}{\partial a}\int_0^t \frac{\partial g^*}{\partial \eta}d\tau\right) \\
& + \frac{1}{2c_w}\frac{\partial (G_c \ell)}{\partial \eta}\nabla(b\dot{a})\cdot\nabla a + b\dot{a}\left(\frac{w^{a\prime}}{4c_w}\frac{\partial (G_c/\ell)}{\partial \eta} + \frac{\partial^2 \psi^*}{\partial \dot{a}\partial \eta}\right) + \gamma\dot{q}\left(\frac{\partial \bar{\sigma}_M}{\partial \eta} - \frac{\partial \sigma_0}{\partial \eta} - \frac{\partial^2 g^*}{\partial \dot{q}\partial \eta}\right)\Bigg\}\, \delta\eta\, d\Omega\, dt \\
+ \int_0^T \int_\Omega \Bigg\{ & \frac{\partial o}{\partial u}\delta_\eta u + \rho\xi\cdot\delta_\eta\ddot{u} + \left(\nabla\xi\cdot\frac{\partial^2 W^e}{\partial \varepsilon \partial \varepsilon} + b\dot{a}\frac{\partial^2 W^e}{\partial a \partial \varepsilon} + \gamma\dot{q}\frac{\partial \bar{\sigma}_M}{\partial \varepsilon} - \dot{q}\mu\cdot\frac{\partial M}{\partial \varepsilon}\right)\cdot\nabla\delta_\eta u \\
& + \left(\frac{\partial o}{\partial q} - \gamma\dot{q}\frac{\partial \sigma_0}{\partial q} + b\dot{a}d'\frac{\partial W^p}{\partial q}\right)\delta_\eta q + \left(-\gamma\dot{q}\frac{\partial^2 \bar{g}^*}{\partial \dot{q}^2} + \gamma\left[\sigma_M - \sigma_0 - \frac{\partial \bar{g}^*}{\partial \dot{q}}\right] - \mu\cdot M\right)\delta_\eta\dot{q} \\
& + b\dot{a}d'\int_0^t \left(\frac{\partial \bar{g}^*}{\partial \dot{q}}\delta_\eta\dot{q}\right)d\tau + \mu\cdot\delta_\eta\dot{\varepsilon}^p \\
& + \left(\frac{\partial o}{\partial \varepsilon^p} + \nabla\xi\cdot\frac{\partial^2 W^e}{\partial \varepsilon \partial \varepsilon^p} + b\dot{a}\frac{\partial^2 W^e}{\partial a \partial \varepsilon} + \gamma\dot{q}\frac{\partial \bar{\sigma}_M}{\partial \partial \varepsilon^p} - \dot{q}\mu\cdot\frac{\partial M}{\partial \varepsilon^p}\right)\cdot\delta_\eta\varepsilon^p \\
& + \left(\frac{\partial o}{\partial a} + \frac{\partial^2 W^e}{\partial a \partial \varepsilon}\cdot\nabla\xi + b\dot{a}\left[\frac{\partial^2 W^e}{\partial a^2} + \frac{G_c}{4c_w\ell}\frac{\partial^2 w^a}{\partial a^2}\right] + b\dot{a}d''\left[W^p + \int_0^t g^* d\tau\right)\right]\delta_\eta a \\
& - b\dot{a}\nabla\cdot\left(\frac{G_c\ell}{2c_w}\nabla\delta_\eta a\right) + bD_a\delta_\eta\dot{a} + b\dot{a}\frac{\partial^2 \bar{\psi}^*}{\partial \dot{a}^2}\delta_\eta\dot{a}\Bigg\}\, d\Omega\, dt,
\end{aligned} \tag{5.69}$$

where

$$D_a = \frac{\partial W^e}{\partial a} + \frac{\partial d}{\partial a}\left(W^p + \int_0^t g^*\, d\tau\right) - \nabla\cdot\left(\frac{G_c\ell}{2c_w}\nabla a\right) + \frac{G_c}{4\ell c_w}\frac{\partial w^a}{\partial a} + \frac{\partial \bar{\psi}^*}{\partial \dot{a}}. \tag{5.70}$$

The standard procedure would then be to integrate by parts, and enforce quiescence conditions on the adjoint variables at time $t = T$. However, for the accumulated plastic dissipation term, this is not straightforward. However, we will re-write this as

$$\begin{aligned}
\int_0^T b\dot{a}d' \int_0^t \left(\frac{\partial \bar{g}^*}{\partial \dot{q}}\delta_\eta\dot{q}\right)d\tau\; dt & \\
&= \int_0^T -\frac{\mathrm{d}}{\mathrm{d}t}\left[\int_t^T b\dot{a}d'\; d\tau\right]\int_0^t \left(\frac{\partial \bar{g}^*}{\partial \dot{q}}\delta_\eta\dot{q}\right)d\tau\; dt \\
&= -\left[\left(\int_t^T b\dot{a}d'\; d\tau\right)\int_0^t \left(\frac{\partial \bar{g}^*}{\partial \dot{q}}\delta_\eta\dot{q}\right)d\tau\right]_0^T \\
&\quad + \int_0^T \left(\int_t^T b\dot{a}d'\; d\tau\right)\frac{\partial \bar{g}^*}{\partial \dot{q}}\delta_\eta\dot{q}\; dt.
\end{aligned} \tag{5.71}$$

The boundary term in the above expression is indentically zero, thus

$$\int_0^T b\dot{a}d' \int_0^t \left(\frac{\partial \bar{g}^*}{\partial \dot{q}}\delta_\eta\dot{q}\right)d\tau\; dt = \int_0^T \left(\int_t^T b\dot{a}d'\; d\tau\right)\frac{\partial \bar{g}^*}{\partial \dot{q}}\delta_\eta\dot{q}\; dt. \tag{5.72}$$

Using this in 5.69, we may integrate by parts. Enforcing initial quiescent conditions on the adjoint variables and localizing gives the sensitivities as

$$\begin{aligned}\mathcal{O}_{,\eta}\delta\eta = \int_0^T \int_\Omega \Bigg\{ & \frac{\partial o}{\partial \eta} + \frac{\partial \rho}{\partial \eta}\ddot{u}\cdot\xi + \frac{\partial^2 W^e}{\partial\varepsilon\partial\eta}\cdot\nabla\xi \\ & + b\dot{a}\left(\frac{\partial^2 W^e}{\partial a\partial\eta} + \frac{\partial d}{\partial a}\frac{\partial W^p}{\partial\eta} + \frac{\partial d}{\partial a}\int_0^t \frac{\partial g^*}{\partial\eta}d\tau\right) \\ & + \frac{1}{2c_w}\frac{\partial(G_c\ell)}{\partial\eta}\nabla(b\dot{a})\cdot\nabla a + b\dot{a}\left(\frac{w^{a\prime}}{4c_w}\frac{\partial(G_c/\ell)}{\partial\eta} + \frac{\partial^2\psi^*}{\partial\dot{a}\partial\eta}\right) \\ & + \gamma\dot{q}\left(\frac{\partial\bar{\sigma}_M}{\partial\eta} - \frac{\partial\sigma_0}{\partial\eta} - \frac{\partial^2 g^*}{\partial\dot{q}\partial\eta}\right)\Bigg\}\,\delta\eta\,d\Omega\,dt,\end{aligned} \tag{5.73}$$

if the adjoint variables satisfy the evolution

$$\begin{aligned} 0 = \int_\Omega \Bigg[& \Bigg(\nabla\xi\cdot\frac{\partial^2 W^e}{\partial\varepsilon\partial\varepsilon} + b\dot{a}\frac{\partial^2 W^e}{\partial a\partial\varepsilon} \\ & + \gamma\dot{q}\frac{\partial\bar{\sigma}_M}{\partial\varepsilon} - \dot{q}\mu\cdot\frac{\partial M}{\partial\varepsilon}\Bigg)\cdot\nabla\delta_\eta u \\ & + \rho\ddot{\xi}\cdot\delta_\eta u + \frac{\partial o}{\partial u}\cdot\delta_\eta u\Bigg]\,d\Omega \qquad \forall\delta_\eta u\in\mathcal{U}, \end{aligned} \tag{5.74a}$$

$$\begin{aligned} & \frac{\mathrm{d}}{\mathrm{d}t}\Bigg[\gamma\left(\bar{\sigma}_M - \sigma_0 - \frac{\partial\bar{g}^*}{\partial\dot{q}}\right) - \gamma\dot{q}\frac{\partial^2\bar{g}^*}{\partial\dot{q}^2} \\ & \quad + \frac{\partial\bar{g}^*}{\partial\dot{q}}\left(\int_t^T b\dot{a}d'(a)d\tau\right) - \mu\cdot M\Bigg] \\ & \qquad = \frac{\partial o}{\partial q} + b\dot{a}d'(a)\frac{\partial W^p}{\partial q} - \gamma\dot{q}\frac{\partial\sigma_0}{\partial q} \qquad \text{on } \Omega, \end{aligned} \tag{5.74b}$$

$$\begin{aligned} \frac{\mathrm{d}\mu}{\mathrm{d}t} = & \frac{\partial o}{\partial\varepsilon^p} + \nabla\xi\cdot\frac{\partial^2 W^e}{\partial\varepsilon\partial\varepsilon^p} + b\dot{a}\frac{\partial^2 W^e}{\partial a\partial\varepsilon^p} \\ & + \gamma\dot{q}\frac{\partial\bar{\sigma}_M}{\partial\varepsilon^p} - \dot{q}\mu\cdot\frac{\partial M}{\partial\varepsilon^p} \qquad \text{on } \Omega, \end{aligned} \tag{5.74c}$$

$$\begin{aligned} \frac{\mathrm{d}}{\mathrm{d}t}\left[D_a b + \frac{\partial^2\bar{\psi}^*}{\partial\dot{a}^2}b\dot{a}\right] = & \frac{\partial o}{\partial a} + \frac{\partial^2 W^e}{\partial a\partial\varepsilon}\cdot\nabla\xi \\ & + b\dot{a}\left(\frac{\partial^2 W^e}{\partial a^2} + \frac{G_c}{4c_w\ell}\frac{\partial^2 w^a}{\partial a^2}\right) \\ & + b\dot{a}d''\left(W^p + \int_0^t g^* d\tau\right) \\ & - \nabla\cdot\left(\frac{G_c\ell}{2c_w}\nabla(b\dot{a})\right) \qquad \text{on } \Omega, \end{aligned} \tag{5.74d}$$

$$\xi|_{t=T} = 0, \quad \dot{\xi}|_{t=T} = 0,$$
$$\gamma|_{t=T} = 0, \quad \mu|_{t=T} = 0, \quad b|_{t=T} = 0.$$

5.B Adjoint Problem as Minimization

It is natural to employ an augmented Lagrangian formulation to efficiently solve the adjoint problem as we have done for the forward problem. However, we first need to write the second line of (5.14) as a minimization problem. Recall that this reads,

$$\begin{aligned}\frac{\mathrm{d}}{\mathrm{d}t}\left[D_a b + \frac{\partial^2 \bar{\psi}^*}{\partial \dot{a}^2} b\dot{a}\right] = \frac{\partial o}{\partial a} + \frac{\partial^2 W^e}{\partial a \partial \varepsilon}\cdot\nabla\xi \\ + b\dot{a}\left(\frac{\partial^2 W^e}{\partial a^2} + \frac{G_c}{4c_w\ell}\frac{\partial^2 w^a}{\partial a^2}\right) \\ + b\dot{a}d''\left(W^p + \int_0^t g^* d\tau\right) \\ - \nabla\cdot\left(\frac{G_c\ell}{2c_w}\nabla(b\dot{a})\right) \qquad \text{on } \Omega,\end{aligned} \tag{5.75}$$

where,

$$D_a = \frac{\partial W^e}{\partial a} + \frac{\partial d}{\partial a}\left(W^p + \int_0^t g^*\, d\tau\right) - \nabla\cdot\left(\frac{G_c\ell}{2c_w}\nabla a\right) + \frac{G_c}{4c_w\ell}\frac{\partial w^a}{\partial a} + \frac{\partial \bar{\psi}^*}{\partial \dot{a}}. \tag{5.76}$$

If $\dot{a} > 0$, then $D_a = 0$. Otherwise, if $\dot{a} = 0$, then $\frac{\partial^2 \bar{\psi}}{\partial \dot{a}^2} = 0$. Writing this as an implicit forward-euler discretization (as we will be solving this backwards in time) from timestep $n+1$ to n, gives,

$$\begin{aligned}&\frac{1}{\Delta t}\left[\left(b^{n+1}D_a|_{t_{n+1}} + \bar{\psi}^{*\prime\prime}\Big|_{t_{n+1}} b^{n+1}\dot{a}^{n+1}\right) - \bar{\psi}^{*\prime\prime}\Big|_{t_n} b^n\dot{a}^n\right] \\ &\quad = \frac{\partial o}{\partial a}\Big|_{t_n} + \frac{\partial^2 W^e}{\partial a\partial\varepsilon}\Big|_{t_n}\cdot\nabla\xi^n + b^n\dot{a}^n\,\frac{\partial^2 W^e}{\partial a^2}\Big|_{t_n} \\ &\qquad + b^n\dot{a}^n d''\left[W^p + \int_0^t g^* d\tau\right]_{t_n} - \nabla\cdot\left(\frac{G_c\ell}{2c_w}\nabla(b^n\dot{a}^n)\right) \qquad \text{on } \Omega_{\dot{a}_n>0}, \\ &\frac{1}{\Delta t}\left[b^n D_a|_{t_n} - \left(b^{n+1}D_a|_{t_{n+1}} + \bar{\psi}^{*\prime\prime}\Big|_{t_{n+1}} b^{n+1}\dot{a}^{n+1}\right)\right] \\ &\quad = \frac{\partial o}{\partial a}\Big|_{t_n} + \frac{\partial^2 W^e}{\partial a\partial\varepsilon}\Big|_{t_n}\cdot\nabla\xi^n \qquad \text{on } \Omega_{\dot{a}_n=0}.\end{aligned} \tag{5.77}$$

If we define

$$z^n = \dot{a}^n b^n, \tag{5.78}$$

we may write the first line of (5.77) as a minimization problem

$$\begin{aligned}\inf_{z=0 \text{ on } \Omega_{\dot{a}^n=0}} I[z] = \int_\Omega \Bigg\{ \frac{1}{2\Delta t \bar{\psi}^{*\prime\prime}|_{t_n}} \Big[\Big(b^{n+1} D_a|_{t_{n+1}} + \bar{\psi}^{*\prime\prime}\Big|_{t_{n+1}} b^{n+1}\dot{a}^{n+1} \Big) \\ - \bar{\psi}^{*\prime\prime}\Big|_{t_n} z \Big]^2 \\ + \left(\frac{\partial o}{\partial a}\Big|_{t_n} + \frac{\partial^2 W^e}{\partial a \partial \varepsilon}\Big|_{t_n} \cdot \nabla \xi^n \right) z \\ + \left(\frac{\partial^2 W^e}{\partial a^2}\Big|_{t_n} + d^{\prime\prime} \left[W^p + \int_0^t g^* d\tau \right]_{t_n} \right) \frac{z^2}{2} \\ + \frac{G_c \ell}{4 c_w} |\nabla z|^2 \Bigg\} \, d\Omega.\end{aligned} \tag{5.79}$$

We now introduce another augmented Lagrangian with an auxiliary field $\zeta \in L^2(\Omega)$, and enforce $\zeta = z$ through the Lagrange multiplier field $\chi \in L^2(\Omega)$ and penalty factor r. Thus, the previous minimization is equivalent to finding the saddle point of

$$\begin{aligned}\hat{\mathcal{L}}(z,\zeta,\chi) = \int_\Omega \Bigg\{ \frac{1}{2\Delta t \bar{\psi}^{*\prime\prime}|_{t_n}} \Big[\Big(b^{n+1} D_a|_{t_{n+1}} + \bar{\psi}^{*\prime\prime}\Big|_{t_{n+1}} b^{n+1}\dot{a}^{n+1} \Big) \\ - \bar{\psi}^{*\prime\prime}\Big|_{t_n} z \Big]^2 \\ + \left(\frac{\partial o}{\partial a}\Big|_{t_n} + \frac{\partial^2 W^e}{\partial a \partial \varepsilon}\Big|_{t_n} \cdot \nabla \xi^n \right) z \\ + \left(\frac{\partial^2 W^e}{\partial a^2}\Big|_{t_n} + d^{\prime\prime} \left[W^p + \int_0^t g^* d\tau \right]_{t_n} \right) \frac{z^2}{2} \\ + \frac{G_c \ell}{4 c_w} |\nabla z|^2 + \chi\,(z-\zeta) + \frac{r}{2}(z-\zeta)^2 \Bigg\} \, d\Omega,\end{aligned} \tag{5.80}$$

subject to the constraints that $\zeta = 0$ on $\Omega_{\dot{a}=0}$. Then, conditions for stationarity are

$$\begin{aligned} 0 &= \int_\Omega \left[(r(z-\zeta^n) + \chi)\,\delta z + \frac{G_c \ell}{2 c_w} \nabla z \cdot \nabla \delta z \right] d\Omega \quad \forall \delta z \in \mathcal{A}, \\ 0 &= \int_\Omega (z - \zeta^n)\,\delta\chi \, d\Omega \qquad\qquad\qquad\qquad\qquad\quad \forall \delta\chi \in L^2(\Omega), \end{aligned} \tag{5.81}$$

and

$$\begin{cases} \frac{1}{\Delta t}\left[\left(b^{n+1}D_a|_{t_{n+1}} + \bar{\psi}^{*\prime\prime}\Big|_{t_{n+1}}\zeta^{n+1}\right) - \bar{\psi}^{*\prime\prime}\Big|_{t_n}\zeta^n\right] & \\ \quad = \frac{\partial o}{\partial a}\Big|_{t_n} + \frac{\partial^2 W^e}{\partial a \partial \varepsilon}\Big|_{t_n}\cdot\nabla\xi^n + \zeta^n\,\frac{\partial^2 W^e}{\partial a^2}\Big|_{t_n} & \\ \quad\quad +\zeta^n d''\left[W^p + \int_0^t g^* d\tau\right]_{t_n} - r(z-\zeta^n) - \chi & \text{on } \Omega_{\dot{a}_n>0}, \\ \zeta^n = 0 & \text{on } \Omega_{\dot{a}_n=0}, \\ \frac{1}{\Delta t}\left[\left(b^{n+1}D_a|_{t_{n+1}} + \bar{\psi}^{*\prime\prime}\Big|_{t_{n+1}}\zeta^{n+1}\right) - D_a|_{t_n}b^n\right] & \\ \quad = \frac{\partial o}{\partial a}\Big|_{t_n} + \frac{\partial^2 W^e}{\partial a \partial \varepsilon}\Big|_{t_n}\cdot\nabla\xi^n - rz - \chi & \text{on } \Omega_{\dot{a}_n=0}. \end{cases} \tag{5.82}$$

Using $\zeta^n = \dot{a}^n b^n$ gives

$$\begin{aligned} 0 &= \int_\Omega \left[(r(z-\dot{a}^n b^n)+\chi)\,\delta z + \frac{G_c \ell}{2c_w}\nabla z\cdot\nabla\delta z\right] d\Omega && \forall \delta z \in \mathcal{A}, \\ 0 &= \int_\Omega (z-\dot{a}^n b^n)\,\delta\chi\, d\Omega && \forall \delta\chi \in L^2(\Omega), \\ &\frac{1}{\Delta t}\left[\left(b^{n+1}D_a|_{t_{n+1}} + \bar{\psi}^{*\prime\prime}\Big|_{t_{n+1}}\dot{a}^{n+1}b^{n+1}\right)\right. \\ &\quad \left. - \bar{\psi}^{*\prime\prime}\Big|_{t_n}\dot{a}^n b^n - b^n D_a|_{t_n}\right] = \\ &\quad \frac{\partial o}{\partial a}\Big|_{t_n} + \frac{\partial^2 W^e}{\partial a\partial\varepsilon}\Big|_{t_n}\cdot\nabla\xi^n + \dot{a}^n b^n\,\frac{\partial^2 W^e}{\partial a^2}\Big|_{t_n} \\ &\quad + \dot{a}^n b^n d''\left[W^p + \int_0^t g^* d\tau\right]_{t_n} - r(z-\dot{a}^n b^n) - \chi && \text{on } \Omega. \end{aligned} \tag{5.83}$$

5.C Forward Problem Convergence with Temporal Resolution

We include a convergence study with respect to temporal resolution for the forward problem algorithm presented in Section 5.3. Here, we consider identical parameters to those discussed in Section 5.3.1. However, the number of timesteps is varied from 4.8×10^3 to 7.2×10^4 for fixed 160×40 mesh over a constant simulation time equivalent to that presented in Section 5.3. Figure 5.C.1 shows that the solution converges with respect to temporal resolution, with a convergence rate of 1.38. As an analytical solution does not exist, the reference solution $\bar{u}$ is computed over 10^5 timesteps.

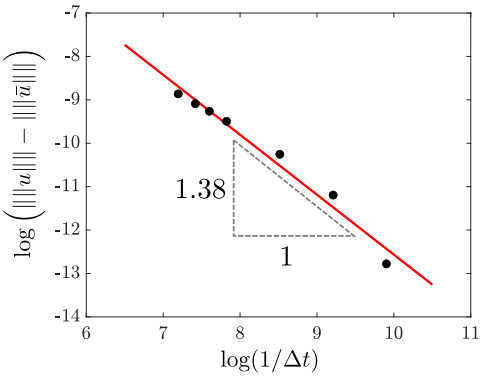

Figure 5.C.1: Solution convergence with respect to temporal resolution. The solution norm $|||u|||$ is studied relative to the timestep size Δt. The black dots represent the data for each simulation, while the red lines show the linear fit, with the first order coeffcient shown on the triangle.

Chapter 6

CONCLUSION

In this thesis we explored optimal design for applications which exploit recent advances in materials and manufacturing. After a brief discussion on the classical methods for optimal design and its challenges, we considered two concrete examples.

First, we examined optimal design of soft responsive actuators. We started from a linear elastic theory with spatially constant actuation. Then, we worked our way up to a formulation which includes finite deformations, microstructural evolution, and 3D print constraints to optimize both structure and material orientation for the model LCE system. Through this, we applied direct methods of calculus of variations to prove well-posedness of a class of carefully chosen objective functions. Here, special attention was placed towards regularization on the spatially varying director field. We designed a variety of integrated lifting actuators in 2D and 3D. Finally, we achieved physical realizations of these structures through advanced 3D printing techniques.

Next, we examined the optimal design of impact resistant structures. We formulated a model which includes transient dynamics, viscoplasticity, and material damage. We developed an accurate and efficient scheme to compute the dynamic trajectory by exploiting an augmented Lagrangian operator splitting method. Then, we introduced optimal design. Careful consideration was put towards material interpolation rules, ensuring natural boundary condition preservation, unfavorable intermediate densities, and efficient numerics. With this formulation, we explored two examples demonstrating dynamic resistance. First, we designed solid-void designs for blast loading. Then, we explored the trade-offs between strength and toughness to design a multi-material spall-resistant structure.

Through these studies, we have addressed major challenges related to the broader goal of optimal design for emerging materials and manufacturing technologies. The investigation on soft actuation explored optimal design for finite deformation and microstructural evolution while considering mathematical regularization for orientation design of anisotropic materials. We also

included manufacturing constraints by encoding the link between fabrication pathway and material microstructure into the design formulation. All of this was treated with rigorous mathematical theory to prove well-posedness of the resulting optimization problem. By studying optimal design for impact resistance, we investigated optimal design for structures with complex material behavior undergoing transient dynamic evolution. We explored the challenges associated with material interpolation, adjoint sensitivity analysis for irreversible processes, and objective choice for impact resistance.

6.1 Extensions

Our contributions to the field of optimal design can be readily extended to include further design considerations, allowing one to tackle related engineering problems. We detail these opportunities and discuss general pathways moving forward.

The first direction of continuation is designing fast actuating responsive structures. Many responsive materials, such as the LCEs we studied, are actuated through heating. Thus, the timescale of forward and reverse actuation are controlled by the heating and cooling of the structure. This creates challenges when quick actuation is required. We may extend the work on soft responsive actuators to additionally consider the response time in the objective. Here, the responsive and passive material might have differing heat conductance, leading to a trade-off between actuation stroke and response time. However, formulating this in an optimal design setting would introduce challenges associated with the modeling and design quantification. We first need to understand the proper objective function in this setting. The initial step is to investigate the design of integrated responsive structures in the small-strain regime where the actuation is temperature dependent, necessitating thermodynamic modeling. We may then introduce finite deformations, orientation dependence, and 3D-printing constraints to design manufacturable, fast responding actuators for real-world deployment.

Another avenue to explore is the design of structures for ballistic loading regimes by extending the formulation for impact resistant structures. To model ballistic impact in solids, thermodynamics plays a large role. Heating through plasticity results in loss of strength which may manifest as adiabatic shear banding. By including thermodynamics into the formulation, we may design

for ballistic loading regimes. Additionally, frictional contact at the impact site is needed to accurately model such scenarios. We may also explore different objective functions such as energy absorption or payload protection.

Another pressing engineering problem we may explore through optimal design is that of energy conversion or storage devices. These systems are complicated by physical mechanisms such as ionic transport coupled with solid deformation and material failure. After developing high-fidelity models to capture these multi-physics interactions in a use-case setting, we may apply optimal design in this setting. The methods we developed may be adapted for such problems. Here, we could explore the design of energy storage devices such as solid-state batteries with greatly improved capacity and lifespan. We may also examine a similar problem of energy conversion devices, where a reaction-diffusion process converts inert gas to usable fuel. Here, special attention must be put towards manufacturing constraints and accurately capturing the chemical mechanisms driving energy flow.

Finally, the tools developed for optimal design may be applied to other PDE based optimization problems. For instance, the methodology may be applied to data-driven constitutive modeling. The rich data sets obtained from emerging experimental techniques provide an opportunity to model material behavior with remarkable precision. However, current methods are limited when accounting for history dependence, fracture, and microstructural evolution. Here, we may apply PDE based optimization methods to construct a methodology similar to optimial design, where the design parameters are now the weights and biases of a neural-net constitutive law. We have recently begun to explore this through a mechanically-consistent formulation which accounts for history dependence.

6.2 Challenges Moving Forward

While there are a number of exciting applications where we may apply optimal design, there are major challenges which must be addressed before optimal design is used in practice for complex engineering problems in a practical setting. We discuss some of these issues and give insights into how they may be approached.

The first issue is rigorously developing means to design for instabilities. Elastic structures undergoing finite deformations may admit multiple energy minimiz-

ing solutions through solution bifurcations. This is desirable in cases such as bi-stable actuators, where one might want to design for such phenomenon. Conversely, buckling in a lifting actuator would lead to poor performance. In both cases, understanding how to deal with instabilities in an optimal design setting is crucial. There are a number of open questions on this front. On the theoretical side, a proper formulation leading to a well-posed design problem is not clear. In terms of computation, ensuring stability or searching for multiple solutions is not straightforward. There remains an interesting research front in formalizing optimal design in these settings to either harness or mitigate structural instabilities.

Another open question is understanding how to design robust structures. Many uncertainties exist when deploying structures in an application setting. Material properties, loading site and magnitude, and boundary conditions are all subject to variance in practice. Thus, performing optimal design for set values may not guarantee sufficient performance. This is especially the case for chaotic systems, such as impact, where a small change in these system parameters may lead to a large change in dynamic trajectory. Thus, we propose that robustness to these uncertainties be included in the design formulation. This could be achieved by a combination of penalizing parameter sensitivities, parallel modeling over a range of system parameters with a "worst case" performance metric, or utilizing methods of uncertainty quantification. A main focus should be developing a design formulation which reliably handles possible discontinuities in dynamic trajectory in a mathematically rigorous fashion.

Rigorous formulations including these considerations may allow optimal design to tackle pressing engineering problems while taking full advantage of emerging materials and manufacturing technologies. The work presented in this thesis will serve as a starting point to these investigations.